INCREASE OF STAGNATION PRESSURE AND ENTHALPY IN SHOCK TUNNELS

David W. Bogdanoff* and Jean-Luc Cambier†
Eloret Institute, 3788 Fabian Way
Palo Alto, California 94303

ABSTRACT

High stagnation pressures and enthalpies are required for the testing of aerospace vehicles such as aerospace planes, aeroassist vehicles and reentry vehicles. Among the most useful ground test facilities for performing such tests are shock tunnels. With a given driver gas condition, the enthalpy and pressure in the driven tube nozzle reservoir condition can be varied by changing the driven tube geometry and initial gas fill pressure. Reducing the driven tube diameter yields only very modest increases in reservoir pressure and enthalpy. Reducing the driven tube initial gas fill pressure can increase the reservoir enthalpy significantly, but at the cost of reduced reservoir pressure and useful test time. A new technique, the insertion of a converging section in the driven tube is found to produce substantial increases in both reservoir pressure and enthalpy. Using a one-dimensional inviscid full kinetics code, a number of different locations and shapes for the converging driven tube section were studied and the best cases found. For these best cases, for driven tube diameter reductions of factors of 2 and 3, the reservoir pressure can be increased by factors of 2.1 and 3.2, respectively and simultaneously the enthalpy can be increased by factors of 1.5 and 2.1, respectively.

I. INTRODUCTION - THE REFLECTED SHOCK SHOCK TUNNEL

The basic setup of a reflected shock shock tunnel is shown in Fig. 1. It comprises a driver tube, driven tube, nozzle and test section. Typically, the driver and driven tubes are

* Senior Research Scientist. Mailing Address: NASA Ames Research Center, Mail Stop 230-2, Moffett Field, CA 94035. Associate Fellow AIAA.

† Scientist. Mailing Address: NASA Ames Research Center, Mail Stop 230-2, Moffett Field, CA 94035. Member AIAA.

separated by a heavy diaphragm and the driven tube and nozzle are separated by a very light diaphragm. The driver is initially filled with a high pressure, high sound speed gas, typically helium or hydrogen, which may be heated to further increase its sound speed and enthalpy. The driven tube is initially filled with the test gas, frequently air or nitrogen, at a much lower pressure. Upon rupture of the main diaphragm a shock wave travels down the driven tube and an expansion wave system moves into the driver gas. The shock wave reflects from the driven tube end wall and breaks the light secondary diaphragm. The doubly shocked gas forms a nozzle plenum reservoir condition. Gas from this reservoir rushes through the nozzle and flow is established there and in the test section. The useful test time is typically hundreds of microseconds to 5 or 10 milliseconds.

We now examine the shock tunnel operation in more detail using the "X-T" diagram shown in Fig. 2. In Fig. 2, X is the distance along the driver and driven tubes and T is the time after the rupture of the diaphragm. Figure 2 is schematic only and is not to scale. In Fig. 2, shock waves are shown as heavy lines, undefined (compression or expansion) waves as single light lines, expansion wave systems as fan-like systems of lines and the interface between the driver and driven gas as a dashed line. The numbers within the zones identify regions of various thermodynamic states. The initial states of the driver and driven gas are 4 and 1, respectively. Upon rupture of the diaphragm, shock S1 moves down the driven tube, compressing the gas from state 1 to state 2. S1 reflects at the driven tube end wall as shock S2, compressing the gas from state 2 to state 5. The driver gas expands through two wave systems, E1 and E2, from state 4 to state 3. The gas in state 3 drives the initial shock S1 through the driven gas. In the classic constant area shock tube the expansion systems E1 and E2 become one continuous expansion system and the zone 3' does not exist. With an area contraction between the driver and driven tubes, the part of the unsteady expansion wave system between lines P and Q is replaced by a quasi-steady expansion through the area contraction between states 3' and 3" and an extended region

at state 3' appears.

The reflected shock S2 passes through the interface at M. If the acoustic impedances of regions 2 and 3 are properly matched, there will be no reflected wave W, all the additional waves near the interface above M will likewise vanish and regions 5, 6, 7, 8, etc. become one region at state 5. This is called "tailored interface" operation. Tailoring can be achieved by varying the initial pressure in region 1. The plenum reservoir for the nozzle during the test time is then at state 5. If one is not operating at the tailored interface condition, wave W and the additional reflected waves above W will exist and conditions in regions 5, 6, 7, 8, etc., will be different. However, in practice, after 2 or 3 reflections from the interface, the waves become quite weak and regions 7, 8, and beyond are essentially at the same condition. This condition will be essentially at the pressure which would be generated by a single shock propagating into region 3, bringing that gas to "rest". This is referred to as "equilibrium interface" operation. The plenum reservoir for the nozzle during the test time is then at the state of regions 7, 8, etc. (which are very closely at the same thermodynamic state).

The available test time of shock tunnels is limited by several factors. Arrival of the head of the reflection of the driver expansion wave system (HE) at the nozzle entrance at time TE initiates a rapid drop in nozzle reservoir pressure and will end the useful test time. Also, passage of the driven gas-driver gas interface I through the nozzle entrance at time TI will end the useful test time. In equilibrium interface operation, the time for the nozzle reservoir condition to settle out, say, between TSH and TS, is not useful test time. Although not related directly to Fig. 2, time is required for the establishment of steady flow in the nozzle and test section and this time cannot be use for testing.

The interface motion shown in Fig. 2 assumes a perfect one-dimensional interface. As is well known, this is very far from being the case in real shock tubes and shock tunnels. A number of effects are known to cause substantial spreading out of the interface. These

include interface distortion upon diaphragm opening, boundary layer effects,[1-3] bifurcation of the reflected shock (S2) near the wall,[4] instability of the interface[2,3,5-7] and combustion at the interface.[3] We do not go into detailed discussion of these effects here, but note the following. For incident shock Mach numbers of 8-10, Fig. 15 of Ref. 3 gives a correlation of experimental data for driver gas free test times. These are only ~25% of the perfect one-dimensional interface values. Also, for some conditions, e.g., some data points of Fig. 14 of Ref. 3, the driver gas free test time can drop to nearly zero.

There is a continuing need for ground facilities with higher stagnation pressures and enthalpies to allow closer simulation in the testing of current and proposed aerospace vehicles. The vehicles include the national aerospace plane, aeroassist space vehicles and reentry vehicles for earth and other planets. The shock tunnel is one of the types of facilities which can provide these simulations. A number of techniques can be used to generate the high enthalpy driver gas needed for such shock tunnels. The driver gas can be characterized by its specific heat ratio (γ), sound speed (c_o), enthalpy (h) and escape speed (u_e). The last speed is the maximum velocity the driver gas would reach if it expanded into vacuum and gives a rough estimate of the maximum initial shock velocity which could be achieved if the inital driver gas to driven gas pressure ratio were very large. For an ideal driver gas u_e can be shown[8] to equal $2c_o/(\gamma\text{-}1)$. Low molecular weight driver gases, hydrogen and helium, are the obvious choices to yield high driver gas sound speeds and enthalpies. These driver gas sound speeds can be further increased by heating. The driver gases have been heated by electrical resistance heaters,[9] combustion of hydrogen and oxygen,[10] piston compression,[11] electric arcs,[12,13] and high explosives.[14] Table 1 shows representative performances for the driver gases for the first three of these techniques, as well as that of room temperature helium and hydrogen. The numbers shown in Table 1 are based on ideal gas calculations and are therefore estimates, not exact numbers. The heated driver gases in the last three rows can produce the most useful simulations of aerospace vehicles.

Table 1 Performances of various driver gases

Reference	Gas	T (K)	γ	c_o (km/sec)	u_e (km/sec)	h (J/gm)
—	He	300	1.67	1.02	3.04	1550
—	H_2	300	1.40	1.32	6.61	4370
9	H_2	700	1.40	2.02	10.10	10200
10	He/H_2O	—	1.50	2.13	8.54	9090
11	He	4660	1.67	3.99	11.90	24100

The electric arc shock tube of Refs. 12 and 13 can produce very high shock velocities, up to 50 km/sec, but has the disadvantages of a driver pressure limitation of 500 atm, very short test times (2-20 μsec) and large capacitive energy storage requirements (1.24 MJ). Because of the pressure and test time limitations, it is not suitable for many of the tests needed for aerospace vehicles. The high explosive driven shock tube of Ref. 14 destroys a large amount of hardware with each test run and cannot be considered a facility useful for an extensive research or test program. Hence, we will focus our attention on the electrical resistance heated driver, the combustion heated driver and the piston compression heated driver of Refs. 9-11.

II. VARIATION OF DRIVEN TUBE DIAMETER AND INITIAL FILL PRESSURE

Let us consider a given driver performance, i.e., with sound speed and enthalpy given, say, by one of the last three rows of Table 1. There will, of course, be a pressure limitation also for the driver. The nozzle plenum reservoir pressure and enthalpy can be changed by changing the driven tube area and initial fill pressure. We will discuss these variations with reference to the NASA Ames 16 Inch Shock Tunnel. The driver tube is 21 m long, 43 cm inside diameter and the driven tube is 26 m long, 30 cm inside diameter. The nozzle is 5.9 m long, the exit diameter is 99 cm and the area ratio can be varied from 95 to 271. The pressure ratings of the driver and driven tubes are 680 atm. The combustion driver

operates with a mixture of $2H_2 + 1.17O_2 + 9.36He$ ignited by 4 wires strung the length of the tube and heated by a capacitor bank discharge. Further details can be found in Ref. 10.

The performance of the Ames Shock Tunnel was analyzed using a simple zoned, inviscid, ideal gas computational method described in Appendix A. This method does not give exact predictions of tunnel performance but does show the trends of the effects of varying the driven tube diameter and initial fill pressure. There are only a few percentage points differences between the enthalpies and pressures reached in the nozzle reservoir conditions, depending on whether the nozzle is plugged or not. Hence, because the calculations are simpler, we consider below only cases with the nozzle plugged. The calculations were done for $2H_2 + O_2 + 9He$ as the drive gas (which is very close to that actually used) and air as the driven gas. Figure 3 shows the ratio of tailored interface driver tube reservoir pressure to driver after burn pressure (P_{res}/P_{dr}) versus the ratio of driven tube area to driver tube area (A_{dn}/A_{dr}). The point is an experimental value from the Ames Shock Tunnel. The maximum pressure gain from A_{dn}/A_{dr} going from 1 to 0 is about a factor of two. For a reasonable value of A_{dn}/A_{dr}, say, 0.3, the gain over a constant area tube is factor of $\sim$1.5. There will be a small attendent gain in reservoir enthalpy, of the order of 10%, also. Making the driven tube smaller has the disadvantages that the amount of gas in the nozzle reservoir condition is reduced and boundary layer effects in the driver tube become more severe. Clearly, the increases in nozzle reservoir pressure and enthalpy obtainable in this way are very limited.

A second approach is to operate the tunnel in the equilibrium interface mode. Figure 4 shows calculated results for equilibrium interface operation of the Ames Shock Tunnel for the actual value of A_{dn}/A_{dr}, 0.498. Again, the calculations were made for the plugged nozzle condition. The abscissa is the ratio of the initial driven tube fill pressure to that at the tailored interface condition. The R_H and R_P curves give the ratios of the driven tube

reservoir enthalpies and pressures achieved to those at the tailored interface condition. The R_R curve gives the ratio of the compression ratio of the driven gas between the initial fill condition and the reservoir condition to that which occurs at the tailored interface condition. The 1,1 coordinate point in Fig. 4 is the tailored interface condition. First, we see that very little increase in driven tube reservoir pressure can be obtained using equilibrium interface operation, perhaps 10%, and this is achieved at at a cost of significant drops in enthalpy.

By decreasing the driven tube initial fill pressure below the tailored interface value, significant increases in enthalpy can be achieved. However, these are achieved at a cost of decreased reservoir pressure and test time. The decreased reservoir pressure can be obtained directly from Fig. 4. Also, however, the driven tube gas is more highly compressed and at a higher sound speed than for the tailored interface case. Both these factors will tend to make the slug of compressed driven tube gas pass through the nozzle more quickly than for the tailored interface case. Further, for the equilibrium interface case, one must wait for the reservoir condition to settle out (i.e., wait between TSH and TS in Fig. 2) before the test time can begin. This waiting is not necessary for tailored interface operation. For example, from Fig. 4, if the initial driven tube fill pressure is reduced to 0.22 times the value for tailored interface operation, the reservoir enthalpy will be doubled, the reservoir pressure will be reduced 21% and the gas compression ratio will be increased by a factor of 1.79. This would cause the time for test gas slug to pass through the nozzle to be reduced to about 40% of the value for tailored interface operation. A further reduction in test time would occur due to the required wait for settling out of the reservoir pressure. Summing up, equilibrium operation can produce only very minor increases in driven tube reservoir pressure. It can produce significant increases in driven tube reservoir enthalpy, but at the cost of significant reductions in reservoir pressure and test time.

III. NEW CONVERGING DRIVEN TUBE TECHNIQUE

A. Technique

As was pointed out in the previous section, simply decreasing the size of the driven tube with respect to the driver tube produces only very limited increases in reservoir pressure pressure and enthalpy. The situation is entirely different if a portion of the driven tube is made converging. We will demonstrate that large increases in reservoir pressure and enthalpy can be obtained if a converging driven tube is used. A number of geometries studied herein are shown in Fig. 5. The diameters of the driver and driven tube are in the correct proportion in the figure but the length-to-diameter of the driven tube is not. As can be seen from Fig. 5, the converging section of the driven tube can be at the upstream end of the tube (cases d,e,f,g,h,j), the downstream end of the tube (cases b,i) or the entire driven tube can be converging (case c). Diameter ratios of 2 (most cases) and 3 (cases i,j) were studied. The majority of the converging sections had a linear diameter taper, but, in addition, both trumpet (cases f,h) and bell shapes (case g) were studied. The equations of the driven tube radius ("taper equations") as functions of distance along the tube are given below.

$$\textit{Linear taper, case d} \qquad \frac{D}{D_o} = 1 - 0.5\frac{x}{\Delta x} \tag{1}$$

$$\textit{Bell, case g} \qquad \frac{D}{D_o} = \sqrt{1 - 0.75\frac{x}{\Delta x}} \tag{2}$$

$$\textit{Trumpet, case f} \qquad \frac{D}{D_o} = 1 - 0.5\sqrt{\frac{x}{\Delta x}} \tag{3}$$

$$\textit{Trumpet, case h} \qquad \frac{D}{D_o} = 1 - 0.647\sqrt{\frac{x}{\Delta x}} \tag{4}$$

where D_o is the diameter of the driven tube inlet, D is the diameter of the driven tube at distance x from the inlet and Δx is the length of the contracting section of the driven tube. An abbreviated numerical code describing each case is also given in Fig. 5. The first digit in each code is the total diameter contraction ratio of the driven tube relative to the reference, constant area driven tube. If there is a single number after the comma, it denotes

either a constant area driven tube ("0" after the comma) or that the contraction occupies the entire driven tube ("1" after the comma). Two numbers after the comma denote the location in the driven tube where the contraction takes place, as follows. "2,20" denotes that the contraction takes place in the upstream half of the tube, while "2,02" denotes that the contraction takes place in the downstream half of the tube. "2,40" denotes that the contraction takes place in the upstream quarter of the tube. If there are only numbers in the designation, the taper is linear in diameter. Letters at the end of the designation denote other curved taper shapes. These include trumpet shapes ("t1", Fig. 5f; "t2", Fig. 5h; "t3", to be discussed at a later point), bell shapes ("b", Fig. 5g) or hyperbolic tangent shapes ("h", not shown in Fig. 5; will be discussed at a later point).

B. Run Conditions and Computational Method

The conditions in the driver for all cases studied were calculated as follows. Before combustion, the driver was assumed to be filled with a $2H_2 + 1.17O_2 + 9.36He$ mixture at 8.622×10^7 d/cm^2 and 292 K. This gas was then allowed to burn adiabatically to an equilibrium mixture and the enthalpy noted. This calculation was repeated with an enthalpy loss of 2.5% added in to bring the calculated sound speed into good agreement with a representative experimental value of 2.13 km/sec. The resulting burned driver gas was at a pressure of 7.075×10^8 d/cm^2, a temperature of 2631 K and had a molecular weight of 6.839. The driven gas for most runs was air at 8.67×10^5 d/cm^2 and 295 K. The nozzle from the secondary diaphragm to the throat is initally filled withe air at 1.014×10^2 d/cm^2 and 295 K. These conditions are nearly identical to those of a number of experimental runs made recently (1991) in the Ames 16 In. Hypersonic Shock Tunnel. The only difference is that the theoretical cases studied herein are at the maximum rated pressure of the Ames facility which is about 25% higher than the pressure of any experimental run made to date.

The calculations were done using a one dimensional, inviscid CFD code. The driven and nozzle gases were modelled using the species N_2, 0_2, NO, N and O and a five equation

reaction set. The mole fractions of the species of the driver gas were frozen at the values given after combustion, as described above. The specific heat of the (frozen) driver gas was taken to follow values from the JANAF Tables.[15] A 250 cell coarse grid was used for the driver and driven tubes. In addition, a sliding 800 cell grid was used which followed the main shock and the interface down the driven tube an then became strationary at the downstream end of the driven tube. The sliding grid allowed much higher resolutions to be obteained in the region of the shocks and the interface. There is an abrupt area change at the main diaphragm. The nozzle is modelled with a 100 cell grid which extends 2 m downstream from the end of the driven tube. For the reference case without driven tube contraction, the throat diameter is 7.60 cm. For most cases with driven tube contraction, the throat diameter is reduced in proportion to the reduced driven tube diameter at the downstream end of the tube. The nozzle diameter at the end of the nozzle grid is 76 cm and the "no gradient" boundary condition is used there. At beginning of the calculation, the primary diaphragm is suddenly removed. When the main shock reaches the secondary diaphragm, the pressure rises steeply; when it reaches 5.07 x 10^7 d/cm^2, the secondary diaphragm is removed.

IV. RESULTS

A. Time Histories at Nozzle Entrance

Figure 6 shows pressure time histories at the nozzle entrance for cases 1,0, 2,02, 2,1 and 2,20. First, we note that use of the driven tube contraction technique can produce about a doubling of the nozzle reservoir pressure. Second, the different contraction geometries have large differences in their ability to maintain the increased reservoir pressure. With the contraction in the downtream half of the driven tube, performance is very poor. Somewhat improved performance is obtained if the entire driven tube is converging. By far the best performance is obtained if the contraction is in the upstream half of the driven tube. In

this case, the nearly flat part of the pressure history extends out to ~13 msec after arrival of the main shock. For this best case, the increase in reservoir enthalpy due to the driven tube contraction is by a factor of ~1.5. From the pressure variations seen in the first ~2 msec in Fig. 6, it is clear that the shock tunnel operation is not tailored for the cases shown there. Tailoring is computationally expensive, typically requiring ~5 additional runs with varying initial driven tube pressure per case and hence, has not been done for most cases presented herein. Tailoring of an optimized case for a 2 to 1 diameter driven tube contraction will be discussed at a later point. A comparison was then made between the nozzle entrance pressure histories for the 2,20 case and the 2,40 case with the contraction taking place in the upstream quarter of the driven tube. For brevity, the plots are not shown here, but in regard to the ability to maintain the high reservoir pressure the 2,40 case was found to be much inferior to the 2,20 case.

Further studies are now presented keeping the basic 2,20 location of the contraction section, but considering non-linear diameter tapers. We consider cases 2,20, 2,20t1 and 2,20b. These are linear, trumpet and bell shaped tapers, respectively, and the equations of the tapers are given in Sec. IIIA, Eqs. (1), (3) and (2), respectively. Figure 7 shows the nozzle entrance pressure histories for these three cases. At this point in the study, we are searching for the contraction geometry which produces the most nearly constant nozzle reservoir conditions. From Fig. 7, we can see that the 2,20b case is roughly equivalent to the 2,20 case in this respect, but that the 2,20t1 case is substantially better than the 2,20 case. Since the trumpet case 2,20t1 produced the most nearly constant reservoir pressure history, this line of attack was pursued further and two additional trumpet cases were investigated. For case 2,20t2 (Eq. (4), Sec. IIIA) the basic shape of the trumpet of case 2,20t1 was maintained, but the trumpet entrance diameter was increased to equal the driver tube diameter, thus eliminating the step area change at the main diaphragm. The driven tube diameter at the downstream end of the tube is the same for cases 2,20t1 and

2,20t2 (and also for all 2,– cases). For case 2,20t3 the taper equation is given below.

$$\frac{D}{D_o} = 0.5 + 0.5\left(1 - \frac{x}{\Delta x}\right)^2 \tag{5}$$

For cases 2,20t1 and 2,20t2, there is an abrupt change in wall slope at the downstream end of the taper section. For case 2,20t3 the taper section slope, instead, goes smoothly to zero at the downstream end of the section. Case 2,20t3 maintains the step area change at the main diaphragm typical of all 2,– cases except the 2,20t2 case. Figure 8 shows the nozzle entrance pressure histories for cases 2,20t1, 2,20t2 and 2,20t3. The 2,20t2 case shows about a 15% pressure increase over the 2,20t1 case (after the initial pressure spiking). However, both the 2,20t2 and the 2,20t3 show much more variation of nozzle reservoir pressure during the critical first ~13 msec than the 2,20t1 case.

One last non-linear taper case was tested, case 2,20h. The taper equation for this case is given below.

$$\frac{D}{D_o} = 1 - \frac{1}{4}\left(1 + \frac{tanh\left(\frac{4x}{\Delta x} - 2\right)}{tanh2}\right) \tag{6}$$

This taper equation is a hyperbolic tangent with minimum slope at the beginning and end of the taper section and maximum slope at the middle of the taper section. Compared to other cases, for case 2,20h there is a relatively steep wall slope at the middle of the taper section and fairly early in the CFD calculation it became apparent that choking was occuring near the maximum slope point. Hence, this taper was rejected as unsatisfactory and the solution stopped. Hence, no nozzle entrance time histories were obtained for this case. We will discuss choking further in Sec. IVB. From the discussion of this section, we conclude that the best contraction geometry of the 2,– cases studied is the trumpet case 2,20t1.

For the optimized case 2,20t1, the tunnel operation was tailored by varying the initial driven tube fill pressure. Calculations were run for pressures of 0.65, 0.75, 0.80, 1.20 and 1.40 times the original driven tube fill pressure of 8.67 x 10^5 d/cm^2. Figure 9 shows the

nozzle entrance pressure histories for 0.65, 0.80, 1.00 and 1.20 times the original driven tube fill pressure. The best tailoring is seen to occur for an initial driven tube fill pressure of 6.94 x 10^5 d/cm^2 or 0.80 times the value used for most run reported herein. For this case, the pressure between 6.2 - 6.6 msec is very nearly equal to that after ~7.4 msec.The wiggle in between these times may be a computational artifact due to the limited resolution of the shock waves and interface.

Figure 10 shows the nozzle reservoir pressure and enthalpy histories for the 1,0 and the 2,20t1 cases (both cases are untailored). We note that for the 1,0 reference case, the pressure starts to fall off ~18 msec after initial shock arrival. This is in excellent agreement with experimental results from the operation of the Ames 16 Inch Tunnel.[10] As mentioned in Sec. IIIB, much of this experimental data was taken at conditions closely matching the reference case 1,0 conditions except that the experimental data was taken at somewhat lower pressure levels. The enthalpy for the 1,0 case is calculated to begin to fall off ~12 msec after initial shock arrival. For the 2,20t1 case, both the pressure and enthalpy are calculated to begin to fall off ~13 msec after initial shock arrival. From Ref. 10, the actual driver gas free test time for the cases nearly matching case 1,0 is estimated to be ~5 msec. This relatively short test time is due to a number of effects which cause the driver-driven gas interface to spread out significantly from the ideal sharp interface (see Sec. I). The increased pressure and enthalpy of the case 2,20t1 nozzle reservoir condition are thus maintained sufficiently long to allow full use of this condition up to the likely time when driver gas will begin the flow through the nozzle, ending the useful test time. Going from the reference case 1,0 to the 2,20t1 case provides an increase in reservoir pressure from 8.01 x 10^8 d/cm^2 to 1.67 x 10^9 d/cm^2, a factor of 2.09. The reservoir enthalpy is increased from 9,500 J/gm to 14,300 J/gm, a factor of 1.51.

We now discuss cases with a driven tube diameter contraction ratio of 3 to 1. Only 3 cases were computed. Two of these cases were with linear diameter tapers, cases 3,02 and

3,20. The third case was a trumpet case denoted by 3,20t1. The taper of the 3,30t1 is of the same form as that of the 2,20t1, with constants adjusted to provide a 3 to 1 diameter ratio. The taper equation of case 3,30t1 is as follows.

$$\frac{D}{D_o} = 1 - 0.667\sqrt{\frac{x}{\Delta x}} \tag{7}$$

The last case was chosen because of the superior performance of case 2,20t1. Figures 11 and 12 show the pressure and enthalpy histories at the nozzle entrance for cases 1,0 (reference case), 3,02, 3,20 and 3,20t1. The performance of the 3,02 case is very poor, considering the 3 to 1 contraction ratio, providing only conditions about equal to those of the 2,20 case. The 3,20 case provides much larger gains in enthalpy and pressure. The trumpet case 3,20t1 provides a further gain in enthalpy of ~10% and a considerably flatter pressure history. Choking effects are quite strong for the 3,20 case, but much less serious for the 3,20t1 case, due to the curved trumpet taper of the latter. The reduction of choking effects for the 3,20t1 case is likely responsible for its superior performance. (Choking effects will be discussed further in Sec. IVB.) It is likely that significantly better taper profiles could be found for 3 to 1 diameter contractions; however, limitations of time and available computational resources have prevented us from pursuing such cases further at the present time.

Let us examine the performance of the 3,20t1 case. From Fig. 11, if we imagine this case to be tailored, it seems likely that the nozzle reservoir pressure could be maintained constant within ~5% for about 5 msec. Further optimization might well allow nearly constant pressure to be maintained for a longer time. Since the arrival of driver gas at the nozzle entrance has been estimated to occur ~5 msec after initial shock arrival, it follows that full utilization of the tunnel test time capability can be achieved using 3 to 1 diameter contraction as well as using 2 to 1 diameter contraction. Going from the reference case 1,0 to the 3,20t1 case provides an increase in reservoir pressure from 8.01 x 10^8 d/cm^2 to

2.59 x 10^9 d/cm^2, a factor of 3.23. The reservoir enthalpy is increased from 9,500 J/gm to 19,800 J/gm, a factor of 2.08.

B. Plots of data along driver and driven tubes

We now turn to plots of data along the driver and driven tubes just before the main shock reaches the nozzle entrance. We consider first the the reference case without driven tube contraction (1,0), the optimized case for 2 to 1 diameter contraction (2,20t1) and the best case for 3 to 1 diameter contraction (3,20t1). This last case uses the trumpet taper of case 2,20t1 modified for 3 to 1 diameter contraction. These cases all have an initial driven tube fill pressure of 8.67 x 10^5 d/cm^2 and are untailored. Figures 13 and 14 shows plots of velocity and pressure for these three cases. In these figures, the driver tube extends from 0 to 21 m and the driven tube from 21 to 47 m. From Fig. 13 we see that the gas velocity behind the main shock rises from 3.1 to 3.8 to 4.6 km/sec for diameter contraction ratios of 1, 2 and 3, respectively. The corresponding pressures behind the main shock rise from 0.9 x 10^8 to 1.6 x 10^8 to 1.9 x 10^8 d/cm^2.

From Fig. 14, even in the downstream one-third of the driver, the pressures are somewhat higher (10 - 15%) for the cases with contraction. The pressure drop at the main diaphragm station is substantially lower for the cases with contraction. This is due to the lower Mach numbers at this station for cases with contraction. The Mach number (plots not shown) on the driven tube side of the diaphragm station is ~0.5 for the cases with contraction compared to 1.0 for the constant driven tube area case. Further, on a fractional basis, the pressure drop in the converging part of the driven tube is much smaller for the cases with contraction than for the corresponding part of the constant area driven tube. In fact, for the 3 to 1 contraction, there is actually a net pressure rise in the contraction section. Finally, for cases with contraction, in the constant area part of the driven tube, the pressure falls off, but the performance of the geometries up to this point has been sufficiently good that the net pressure behind the main shock still considerably exceeds

that for the constant area driven tube case.

We now discuss choking in the driven tube. Figures 15 and 16 show plots of pressure an Mach number along the driver and driven tubes for cases 1,0, 3,20 and 3,20t1. Case 3,20 is a 3 to 1 diameter contraction case with linear taper and case 3,20t1 is the corresponding case with a trumpet taper. For the 1,0 (reference case), the Mach number profile along the driven tube shows a smooth increase from 1.0 at the main diaphragm station to ~1.9 at the end of the expansion fan 3 in Fig. 2 (see Sec. I) and then remains constant out to the interface, across which it jumps to ~2.3. In constrast, for case 3,20, severe choking is apparent at the end of the driven tube contraction section. There is a sharp pressure peak reaching 1.2 x 10^9 d/cm^2, and Mach number, instead of rising in the contraction section, falls from a maximum of ~0.9 to ~0.8 at the end of the contraction section. The rate of contraction of the linear taper in the logarithmic sense, d(ln(Area))/d(x/L), appears to be too great at the end of the contraction for a 3 to 1 diameter ratio. (L is the length of the driven tube.) By switching to the trumpet taper, case 3,20t1, the choking problem in the driven tube is very much ameliorated. The pressure peak at the end of the contraction has been reduced by a factor of 2 and the Mach number in the contraction section now rises smoothly from ~0.5 to ~1.3. There still does remain a much reduced pressure peak at the end of the driven tube contraction section; it is possible that this peak could be removed by further optimization of the contraction taper shape.

In Sec. IVA, we noted that case 2,20h, with a hyperbolic tangent taper profile, produced severe choking. Figure 17 shows plots of pressure and Mach number along the driver and driven tubes for this case. The choking is shown by the sharp pressure peak and Mach number drop (from 1.1 to 0.6) near the center of the taper section, where the slope of the tube wall is the steepest. For this case also, it appears that d(ln(Area))/d(x/L) is too great to avoid substantial choking effects.

C. Test times and impact pressures in the test section

First, we consider cases 1,0 (reference case) and 2,20t1 (optimized case with 2 to 1 diameter contraction). As we have noted previously, the nozzle reservoir pressure and enthalpy of the 2,20t1 case are 2.09 and 1.51 times higher, respectively, than the values for the 1,0 case. However, these gains were not achieved without some cost. The volume of compressed test gas in the driven tube reservoir is considerably smaller for the 2,20t1 case than for the 1,0 case. At this time, we have no way to know whether the spreading out of the driven-driver gas interface (see Sec. I) will be better, worse or about the same for the 2,20t1 case, compared to the 1,0 case. Lacking this information, we shall assume that the volume of compressed driver-gas-free test gas at the nozzle entrance for the 2,20t1 case will be the same fraction of the driven tube volume as for the 1,0 case. The volume of the driven tube for the 2,20t1 case can readily be calculated, using the taper equation (3) to be 0.354 of the volume for the 1,0 case.

We now introduce a number of ratios, all of which are formed by taking the parameter for the case with driven tube diameter contraction (here, case 2,20t1) and dividing by the same parameter for the reference case (1,0). R_p is the ratio of driven tube reservoir pressures, here equal to 2.09. R_h is the ratio of driven tube reservoir enthapies, here equal to 1.51. R_v is the ratio of driven tube reservoir gas volumes, here equal to 0.354. R_t, R_{ath}, R_{ats}, R_{dts} and R_{pi} are the ratios of test time, nozzle throat area, test section area, test section diameter and test section impact pressure, respectively. Now, R_p, R_h and R_v are given for the case 2,20t1 - case 1,0 comparison. However, R_{ath} and R_{ats} can be varied and allow one to trade off among R_{ats}, R_t and R_{pi}. R_t, R_v, R_{ath} and R_h can be related as follows.

$$R_t = \frac{R_v}{R_{ath}} \frac{1}{R_h^{.5}} \tag{8}$$

Equation (8) can be obtained by noting that the flow time of the test gas slug through the nozzle throat is proportion to the volume of the gas slug and inversely proportional to the area of the nozzle throat and the sound speed of the gas. Further, the following

approximate relation for hypersonic flow can be written.

$$R_{pi} = \frac{R_{ath}}{R_{ats}} R_p \tag{9}$$

Equation (9) can be obtained, for example, from the discussion of the treatment of the impulse function in Ref. 16 by assuming that the Mach number is much greater than unity. Combining Eqs. (9) and (10), we obtain

$$R_t R_{pi} R_{ats} = \frac{R_v R_p}{R_h^{.5}} = 0.603 \tag{10}$$

The numerical constant in Eq. (10) was obtained using R_v, R_p and R_h for the case 2,20t1 - case 1,0 comparison (in addition to one case for 3 to 1 diameter contraction).

Using Eqs. (9) and (10), a number of cases will be constructed and discussed. The parameters for these cases are shown in Table 2.

Table 2 Test times and impact pressures

Nozzle case #	Driven tube case	R_{ath}	R_{ats}	R_{dts}	R_h	R_t	R_{pi}
1	1,0	1.00	1.00	1.00	1.00	1.00	1.00
2	2,20t1	0.25	0.25	0.50	1.51	1.15	2.09
3	2,20t1	1.00	1.00	1.00	1.51	0.289	2.09
4	2,20t1	0.50	1.00	1.00	1.51	0.577	1.04
5	2,20t1	0.25	1.00	1.00	1.51	1.15	0.522
6	2,20t1	0.50	0.50	0.707	1.51	0.577	2.09
7	3,20t1	0.367	0.367	0.606	2.08	0.420	3.23

Nozzle case 1 is simply the reference case without driven tube contraction. All ratios for this case are, by definition, equal to unity. For the remaining nozzle cases, driven tube contraction, cases 2,20t1 or 3,20t1 is assumed. For nozzle case 2, the nozzle throat and test section linear dimensions are half the values for the reference case. The test section impact pressure is increased by a factor of $\sim$2 and the test time is actually increased 15% above the value for case 1,0. The disadvantage is that the model must be twice as small as for the

reference case. For nozzle case 3, the nozzle throat and test section linear dimensions kept equal to the values for the reference case. The test section impact pressure is increased by a factor of two and the model size is kept undiminished, but the test time is ~0.29 that for the reference case. For many cases, this would be unsatisfactory, since there might well not be sufficient time for the flow the stabilize properly in the nozzle and/or over the model. Nozzle cases 4 and 5 are cases where the nozzle throat area has been reduced by factors of 2 and 4, respectively, from that of case 3, while keeping the test section size undiminished. The result is that the test times are increased in inverse proportion to the throat areas, but the impact pressures in the test section are correspondingly reduced.

For nozzle cases 2 - 5, we have not considered that less test time should be required to establish the flow if the nozzle and model are smaller and also that less test should be required when the free stream velocity is faster due to increased reservoir enthalpy. To allow for this we now assume the following.

$$R_{ats}^{.5} = R_h^{.5} R_t \tag{11}$$

The condition of Eq. (11) is that the test section (and presumably nozzle and model) dimensions should vary, for the various cases studied, proportionally to the free stream velocity and the test time. Applying the condition of Eq. (11) to Eq. (10) yields the following equation.

$$R_{pi} R_t^3 = 0.401 \tag{12}$$

Let us assume that we wish to obtain the full pressure advantage of the driven tube contraction technique and therefore take $R_{pi} = 2.09$. From Eqs. (9), (11) and (12), we then obtain $R_t = 0.577$, $R_{ats} = R_{ath} = 0.500$ and $D_{ats} = 0.707$, nozzle case 6 in Table 2. For this case, the test time is 0.577 times that of the baseline case, but this shorter time should be just as effective a setting up the flow as in the reference case, since the model is smaller and the flow is faster. The test section and model size are 0.707 that for the

reference case and the full pressure advantage of the driven tube contraction technique is available in the test section.

We should note here that nozzle cases 4 and 5 in Table 2 involve a change in area ratio of the nozzle, since R_{ats} is not equal to R_{ath} for these cases. If these cases were to be used, there would be a tendency for the test section Mach number to change from that for the reference case. For example, assuming a reference case test section Mach number of 5 and and effective γ value of 1.25, doubling and quadrupling the nozzle area ratio would increase the Mach number to ~5.6 and ~6.2, respectively.

We now discuss the case for a 3 to 1 diameter contraction, using cases 3,20t1 and 1,0. R_p, R_h and R_v for this case are 3.23, 2.08 and 0.222, respectively. For brevity, we go directly to the case where we maintain the full pressure advantage of the contraction technique and allow the test time to be shortened corresponding to a shorter nozzle and model and faster flow. The resulting parameters are shown in Table 2, nozzle case 7. The test time is 0.420 times that of the baseline case but should be equally satisfactory at setting up the flow properly. The model dimensions are 0.606 times those for the baseline case. Other possible combinations of R_{ats} and R_{ath} could of course be used, allowing a wide variety of cases to be obtained, including those corresponding to nozzle cases 2 - 5 for 2 to 1 diameter contraction.

D. Further work

Pursuing the converging driven tube technique further would likely involve the following steps. First, a contraction ratio yielding approximately the desired condition would be selected. Then, inviscid analyses similar to those presented here should be done, but in more depth, to allow the best location and shape of the contraction section to be found. Then, axisymmetric viscous flow analyses with turbulence modelling should be carried out. This would allow possible additional choking effects due to boundary layers to be studied as well as some of the effects which cause spreading out of the driver-driven interface.

The latter include jetting of the driver gas upon initial rupture of the main diaphragm, effects of the boundary layer upon the motion of the initial shock and the driver-driven gas interface, bifurcation of the reflected shock in the boundary layer and, possibly, instability effects at the interface. The best viscous flow cases should then be tested experimentally in a small facility. Finally, if the predicted gains in pressure and enthalpy are verified experimentally at small scale, one might consider the modification of a major facility to use the driven tube contraction technique.

V. CONCLUSIONS

High stagnation pressures and enthalpies are required for the testing of aerospace vehicles such as aerospace planes, aeroassist vehicles and reentry vehicles. Shock tunnels are among the most useful facilities to perform such tests. For large, high pressure production facilities, the most practical ways of achieving high enthalpy in the driver of a shock tunnel are to use light gases, hydrogen or helium, and to heat the gas using electrical resistance heaters, combustion or piston compression. The enthalpies achieved in these ways are limited and there are also pressure limits on the driver tube. Given a fixed driver condition, the nozzle reservoir enthalpy and pressure in the driven can be varied by changing the size of the driven tube and the initial driven tube fill pressure. The gains in pressure and enthalpy achievable using the former technique are very limited. The latter technique can be used to achieve significant increases in enthalpy, but at the cost of decreased pressure and test time.

A new technique has been presented which allows substantial increases in nozzle reservoir pressure and enthalpy to be achieved simulataneously. In this technique, part of the driven tube is made converging. This technique has been investigated using a one-dimensional, inviscid CFD code with chemical kinetics. The computational techniques were applied to analyze possible modifications of the NASA Ames 16 Inch Hypersonic Shock Tunnel. Contraction ratios for the driven tube diameter of 2 to 1 and 3 to 1 were

studied, the former in more detail. The length, location and shape of the converging section have been varied and partially optimized cases, within the limitations of available computer time, have been found. Data has been presented in the form of pressure and enthalpy histories at the driven tube nozzle reservoir and as snapshots of velocity, pressure and Mach number along the the driver and driven tubes.

For a driven tube diameter contraction ratio of 2 to 1, increases in nozzle reservoir pressure and enthalpy of 2.1 and 1.5, respectively, were obtained for the best cases studied. For a driven tube diameter contraction ratio of 3 to 1, the corresponding numbers were found to be 3.2 and 2.1. Choking in the driven tube was found to be a problem for some cases studied. It was found that choking effects could be minimized by the proper selection of the location, length and shape of the contraction section. Using both 2 to 1 and 3 to 1 diameter contraction ratios, test times during which the nozzle reservoir maintained nearly constant pressure and enthalpy were evaluated. These were found to exceed or equal the experimentally estimated driver-gas-free test time for the Ames Shock Tunnel. Hence, the full test time of the tunnel would appear to remain usable if it were modifed with optimized 2 to 1 or 3 to 1 driven tube contraction profiles.

The gain in nozzle reservoir pressure and enthalpy achieved using the driven tube contraction technique is not obtained without cost. There is a significant reduction in the available volume of gas at the nozzle reservoir conditions. For this reason, there will a tendency for the test time and the size of the test section which can be operated at a given impact pressure to be reduced when the driven tube contraction technique is used. By varying the nozzle throat and test section dimensions, trade-offs can be made between test time, test section size and test section impact pressure. These questions have been studied for the best 2 to 1 and 3 to 1 contraction cases investigated. For these cases, for one set of calculations, it was assumed that when using the contraction technique, it was desired to maintain the full gain in impact pressure in the tunnel test section. Also, allowances were

made for the fact that the test section flows could be stabilized in shorter times since the models and nozzle were smaller and the flows faster (on account of the higher enthalpies) when contraction was used. For these conditions, for the best 2 to 1 contraction case, the model size was found to be 0.707 of that for the baseline case (without contraction) and the test time was found to be 0.577 of that for the baseline case. For the best 3 to 1 contraction case, the corresponding numbers were found to be 0.606 (for model size) and 0.42 (for test time). However, we must point out again that these shorter test times should be fully sufficent to stabilize the flows as well as in the baseline case without contraction. Other combinations of nozzle throat area and test section area have also been discussed. For example, for the best 2 to 1 contraction case, the full impact pressure gain can be maintained and the full model size maintained, with the penalty that the test time drops to 0.29 of that without contraction.

APPENDIX A

This appendix describes a simple zoned, inviscid, ideal gas method of estimating the performance of the driver and driven tubes of a shock tunnel. We refer to the X-T diagram of Fig. 2 of the main text. A description of this diagram is given in Sec. I of the main text and will not be repeated here. The gases are taken to be ideal, with γ values estimated from the enthalpy values of the JANAF tables for roughly estimated temperature ranges for the various zones. With one exception, all friction and heat transfer effects are neglected. The driver gas is initially taken to be $2H_2 + O_2 + 9He$, which burns to $2H_2O + 9He$. The driven gas is air, taken as $3.77N_2 + O_2$. The one dissipative effect which is modelled is that 30% of the energy which would be released upon complete driver gas combustion is assumed to be lost. This was found to bring the calculated shock velocities into rough agreement with experimental values and thus crudely allows for dissociation, heat transfer and frictional losses. Expansion waves, such as E1 and E2 and W (if it is an expansion wave), are treated as simple centered expansion wave systems. The flow from 3' to 3"

is taken to be a simple steady expansion to Mach 1 at 3". Shocks S1, S2, the shock above and to the left of M and W (if it is a shock) are treated by standard shock wave analyses. The flow velocity in zones 2 and 3 is varied until the pressures in these two zones match, to obtain the correct velocity. A similar procedure is applied in the two zones above M to obtain the correct velocity and pressure of these zones. To tailor the operation of the tunnel, the initial pressure in zone 1 is varied until wave W is of zero strength. For equilibrium interface operation, the conditions in zone 5 are first calculated. Then the pressure which zone 3 would reach if brought to rest by a single shock ($p_{3,shock}$) is calculated. The equilibrium interface nozzle reservoir conditions are then calculated by assuming isentropic compression or expansion from state 5 to the pressure $p_{3,shock}$. The code available at Ames can allow for flow through a shock tunnel nozzle of specified area. The calculation is somewhat shorter if the nozzle is taken to be plugged. Results for plugged nozzles were used in the discussion of the main text.

ACKNOWLEDGEMENTS

This research was supported by a grant from NASA to the Eloret Institute (NCC-2-487).

REFERENCES

1. Mirels, H., "Shock Tube Test Time Limitation Due to Turbulent-Wall Boundary Layer," *AIAA Journal*, Vol. 2, January, 1964, pp. 84-93.
2. Bird, K. D., Martin, J. F. and Bell, T. J., "Recent Developments in the Use of the Hypersonic Shock Tunnel as a Research and Development Facility," in *3rd Symposium on Hypervelocity Techniques*, Denver Research Institute, University of Denver, Denver, CO, 17-18 March 1964.
3. Copper, J. A., Miller, H. R. and Hameetman, F. J., "Correlation of Uncontaminated Test Durations in Shock Tunnels," in *Fourth Hypervelocity Techniques*

Symposium, Arnold Engineering Development Center, Arnold Air Force Station, TN, 15-16 November, 1965.

4. Stalker, R. J. and Crane, K. C. A., "Driver Gas Contamination in a High-Enthalpy Reflected Shock Tunnel," *AIAA Journal*, Vol. 16, March 1978, pp. 277-279.
5. Kaegi, E. M. and Muntz, E. P., "Driver-Driven Gas Mixing and Its Effect on Shock Tunnel Test Time," in *3rd Symposium on Hypervelocity Techniques*, Denver Research Institute, University of Denver, Denver, CO, 17-18 March 1964.
6. Richtmyer, R. D., "Taylor Instability in Shock Acceleration of Compressible Fluids," *Commun. Pure Appl. Math.*, Vol. 13, May 1960, pp. 297-319.
7. Meshkov, Y. Y., "Instability of a Shock Wave Accelerated Interface Between Two Gases," NASA TT F-13,079, June, 1970.
8. Shapiro, A. H., "The Dynamics and Thermodynamics of Compressible Fluid Flow," Ronald, New York, 1954, pp. 945-947.
9. "Hypersonic Shock Tunnel, Description and Capabilities," Calspan Corporation, Buffalo, NY, January, 1987.
10. Bogdanoff, D. W., Zambrana, H. A., Cavolowsky, J. A., Newfield, M. E., Cornelison, C. J. and Miller, R. J., "Reactivation and Upgrade of the NASA Ames 16 Inch Shock Tunnel; Status Report," AIAA Paper 92-0327, presented at the 30th Aerospace Sciences Meeting, Reno, NV, January 6-9, 1992.
11. Hornung, H. G. and Belanger, J., "Role and Techniques of Ground Testing for Simulation of Flows Up to Orbital Speed," presented aat the AIAA 16th Ground Testing Conference, Seattle, WA, June 18-20, 1990.
12. Sharma, S. P. and Park, C., "Operating Characteristics of a 60- and 10-cm Electric Arc-Driven Shock Tube-Part I: The Driver," *Journal of Thermophysics and Heat Transfer*, Vol. 4, July 1990, pp. 259-265.
13. Sharma, S. P. and Park, C., "Operating Characteristics of a 60- and 10-cm

Electric Arc-Driven Shock Tube-Part II: The Driven Section," *Journal of Thermophysics and Heat Transfer*, Vol. 4, July 1990, pp. 266-272.

14. Compton, D. L. and Cooper, D. M., "Duplication in a Shock Tube of Stagnation Region Conditions on a Jovian Atmosphere-Entry Probe," *Recent Developments in Shock Tube Research: Proceedings of the 9th International Shock Tubes Symposium*, ed. D. Bershader and W. Griffith, Stanford Univ., Stanford, CA, 1973, pp. 318-329.

15. Stull, D. R. and Prophet, M., project directors, *JANAF Thermochemical Tables*, U.S. Government Printing Office, Washington, DC, NSRDS-NBS 37, June 1971, p. 4.

16. Shapiro, A. H., "The Dynamics and Thermodynamics of Compressible Fluid Flow," Ronald, New York, 1954, pp. 86-87.

Figure Captions

Fig. 1 Sketch of shock tunnel (not to scale).

Fig. 2 x-t wave diagram for shock tunnel. S1 and S2 denote shock waves, E1 and E2 denote expansion wave systems, HE denotes the head of the expansion wave system reflected from the end of the driver, I denotes driver-driven gas interface. 1,2,3,3',3",4, etc. denote thermodynamic states. Also, see text.

Fig. 3 Effect of driven/driver area ratio (A_{dn}/A_{dr}) on ratio of reservoir pressure to driver pressure (P_{res}/P_{dr}). Tailored interface. See text for other details of operating conditions.

Fig. 4 Non-tailored operation of shock tunnel. Abscissa is ratio of driven tube fill pressure to that required for tailored interface operation. On the ordinate are shown the ratios of nozzle reservoir pressure (R_p) and enthalpy (R_h) to those obtained for tailored interface operation. R_r is the volumetric compression ratio of the doubly shocked gas in the nozzle reservoir divided by the corresponding value for tailored interface operation. See text for details of operating conditions.

Fig. 5 Various driven tube contraction profils studied herein. Diameters are to consistent scale, length is not at same scale as diameters.

Fig. 6 Pressure histories at nozzle reservoir for cases 1,0, 2,02, 2,1 and 2,20.

Fig. 7 Pressure histories at nozzle reservoir for cases 2,20, 2,20b, and 2,20t1.

Fig. 8 Pressure histories at nozzle reservoir for cases 2,20t1, 2,20t2 and 2,20t3.

Fig. 9 Pressure histories at nozzle reservoir for case 2,20t1. Parameters shown on curves are ratios of driven tube initial fill pressure to that for the first case calculated. The tailoring effect is shown.

Fig. 10 Pressure and enthalpy histories at nozzle reservoir for cases 1,0, and 2,02t1.

Fig. 11 Pressure histories at nozzle reservoir for cases 1,0, 3,02, 3,20 and 3,20t1.

Fig. 12 Enthalpy histories at nozzle reservoir for cases 1,0, 3,02, 3,20 and 3,20t1.

Fig. 13 Snapshot along driver and driven at time initial shock reaches nozzle entrance. Velocity, cases 1,0, 2,20t1 and 3,20t1.

Fig. 14 Snapshot along driver and driven at time initial shock reaches nozzle entrance. Pressure, cases 1,0, 2,20t1 and 3,20t1.

Fig. 15 Snapshot along driver and driven at time initial shock reaches nozzle entrance. Pressure, cases 1,0, 3,20 and 3,20t1.

Fig. 16 Snapshot along driver and driven at time initial shock reaches nozzle entrance. Mach number, cases 1,0, 3,20 and 3,20t1.

Fig. 17 Snapshot along driver and driven at time initial shock reaches nozzle entrance. Pressure and Mach number, case 2,20h.

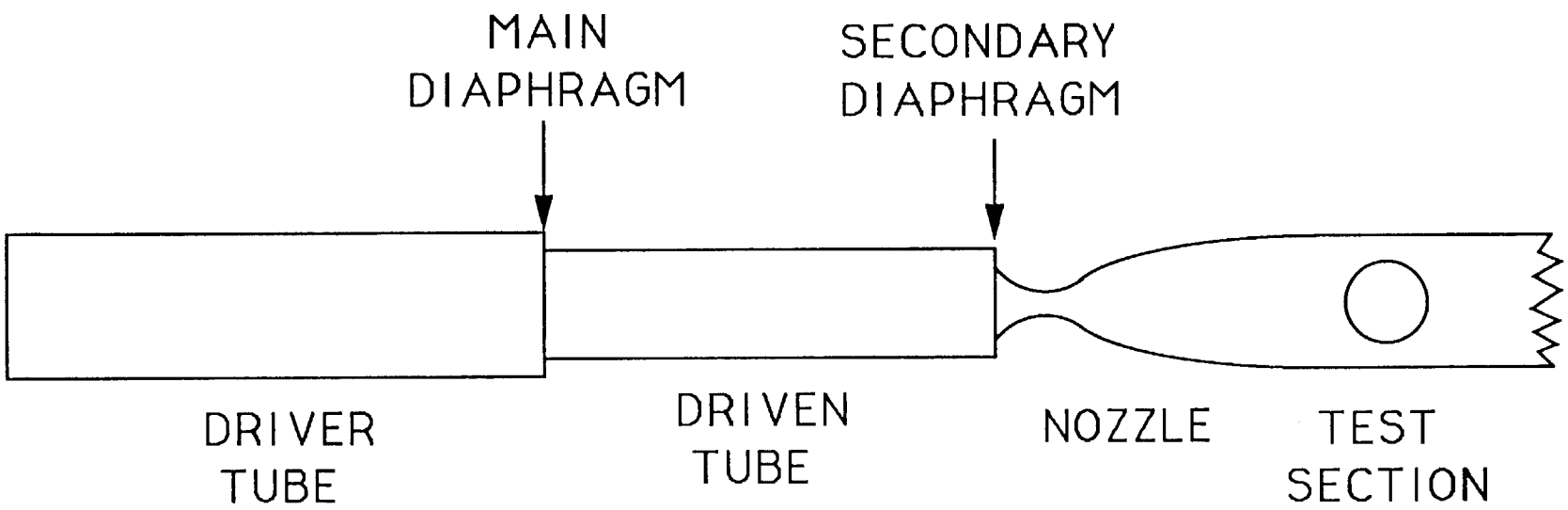

Fig. 1
D. W. Bogdanoff
J.-L. Cambier

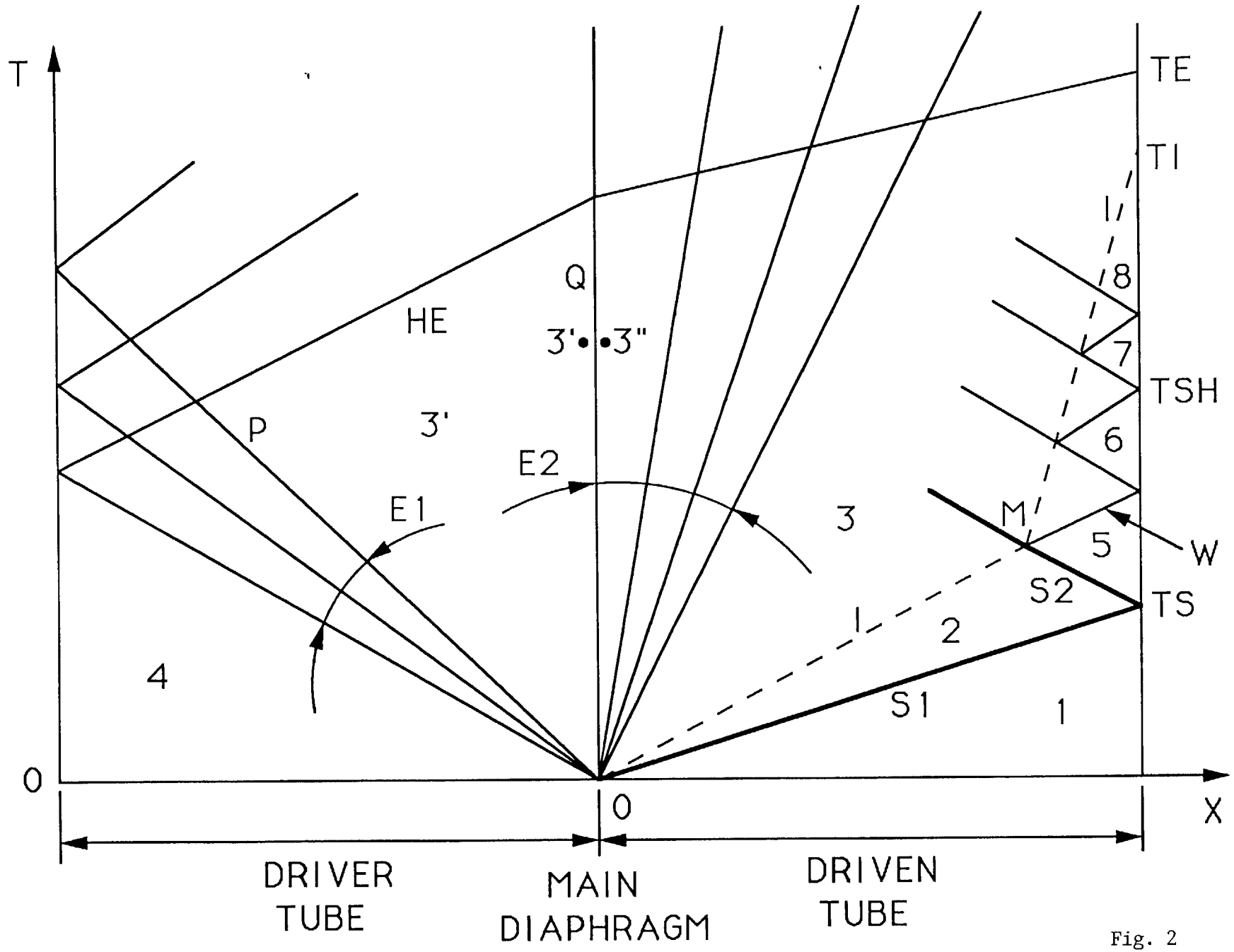

Fig. 2
D. W. Bogdanoff
J.-L. Cambier

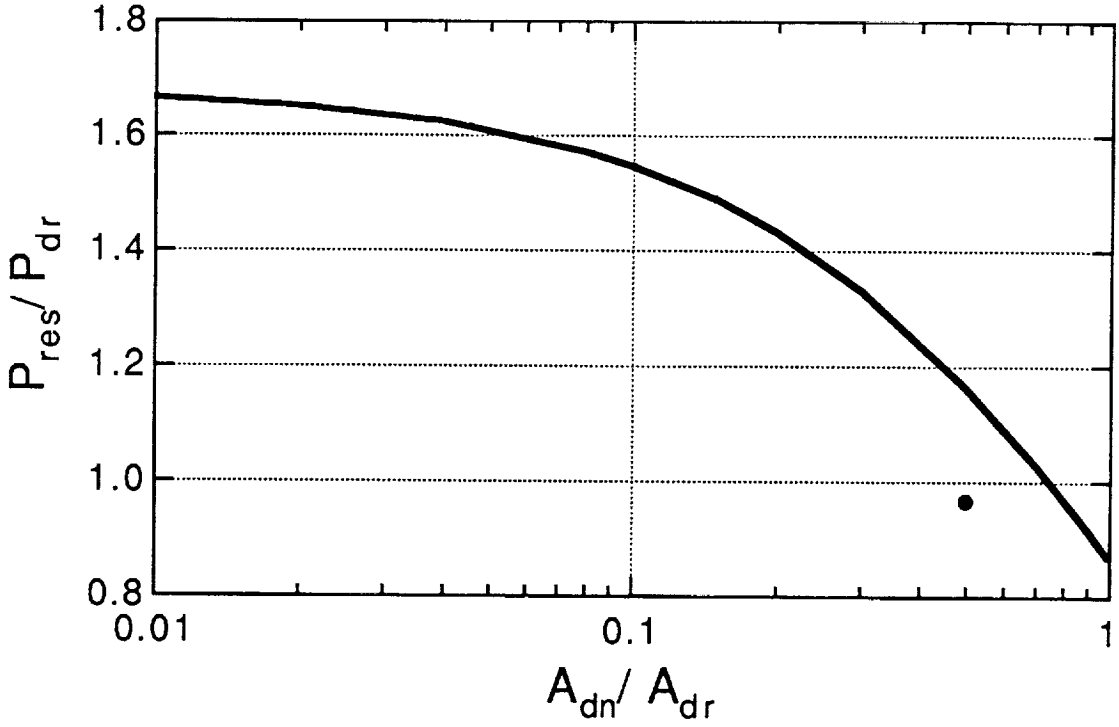

Fig. 3
D. W. Bogdanoff
J.-L. Cambier

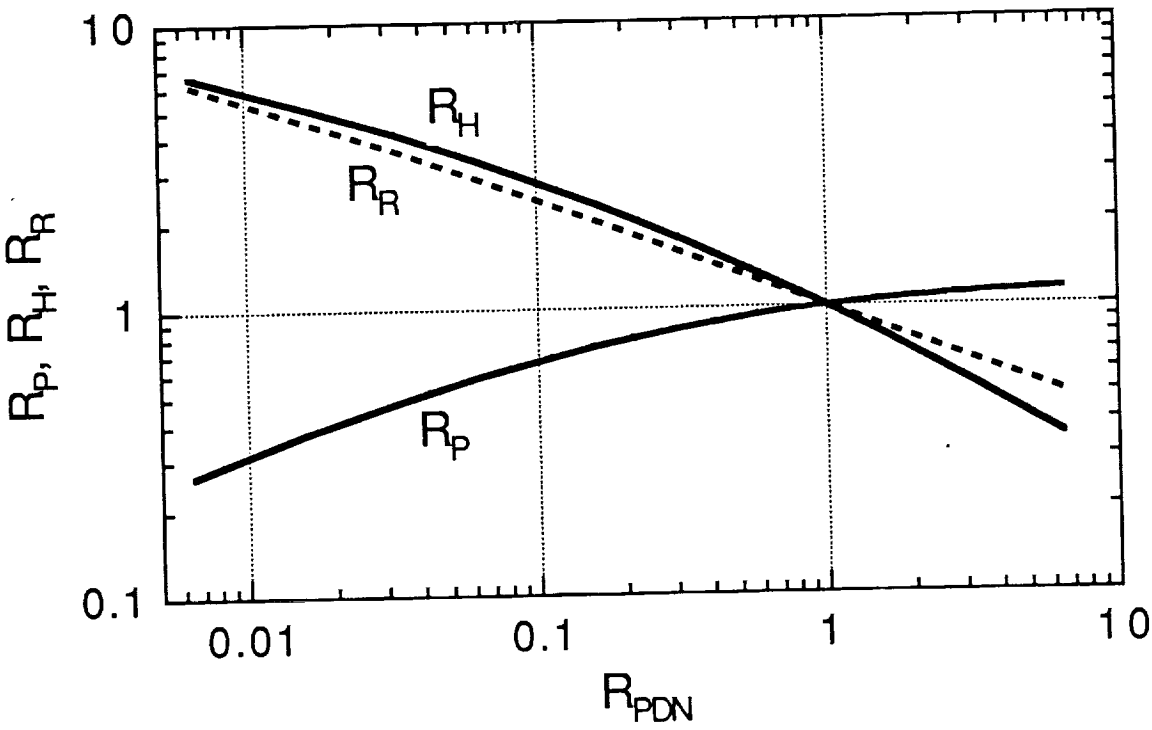

Fig. 4
D. W. Bogdanoff
J.-L. Cambier

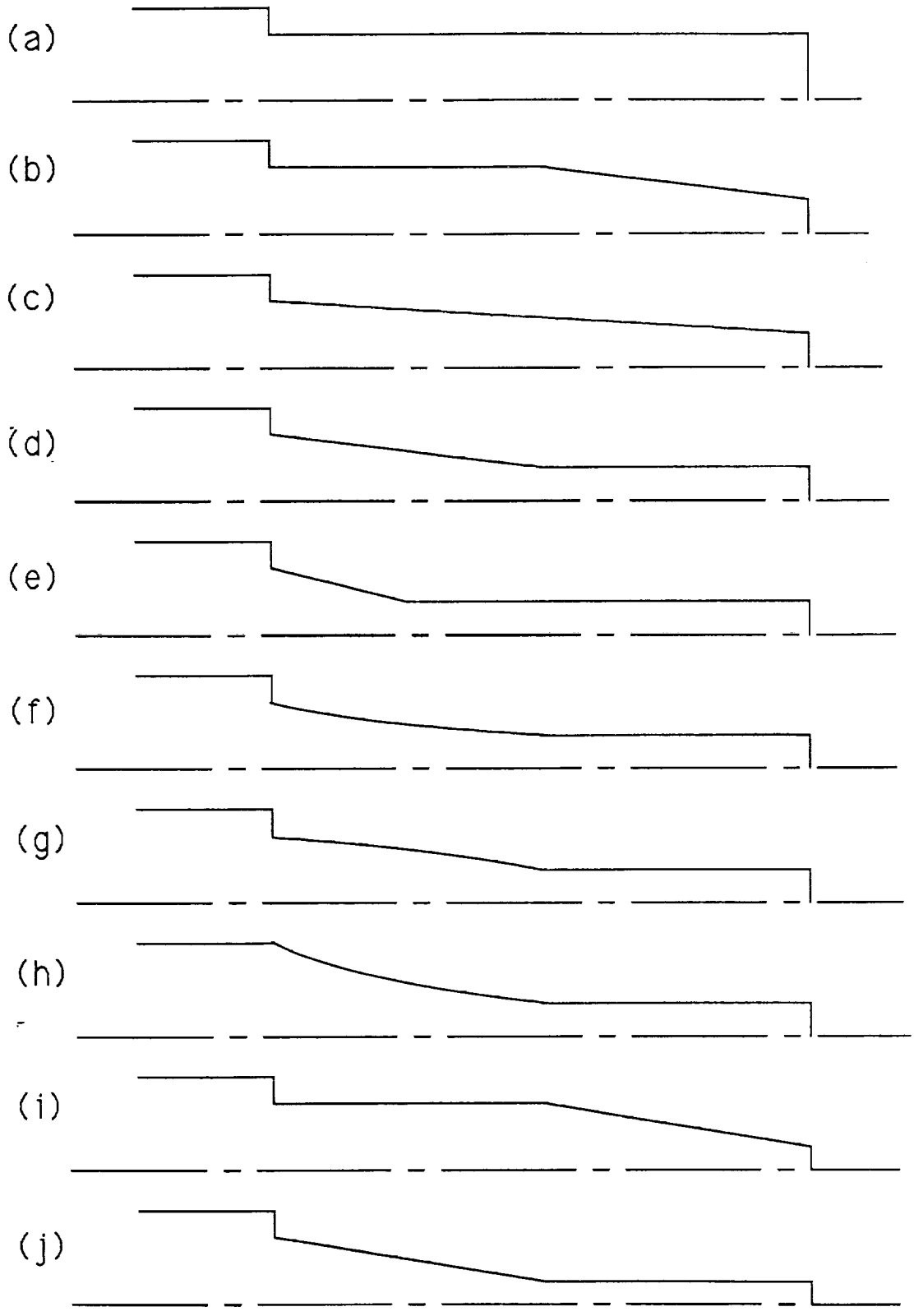

Fig. 5
D. W. Bogdanoff
J.-L. Cambier

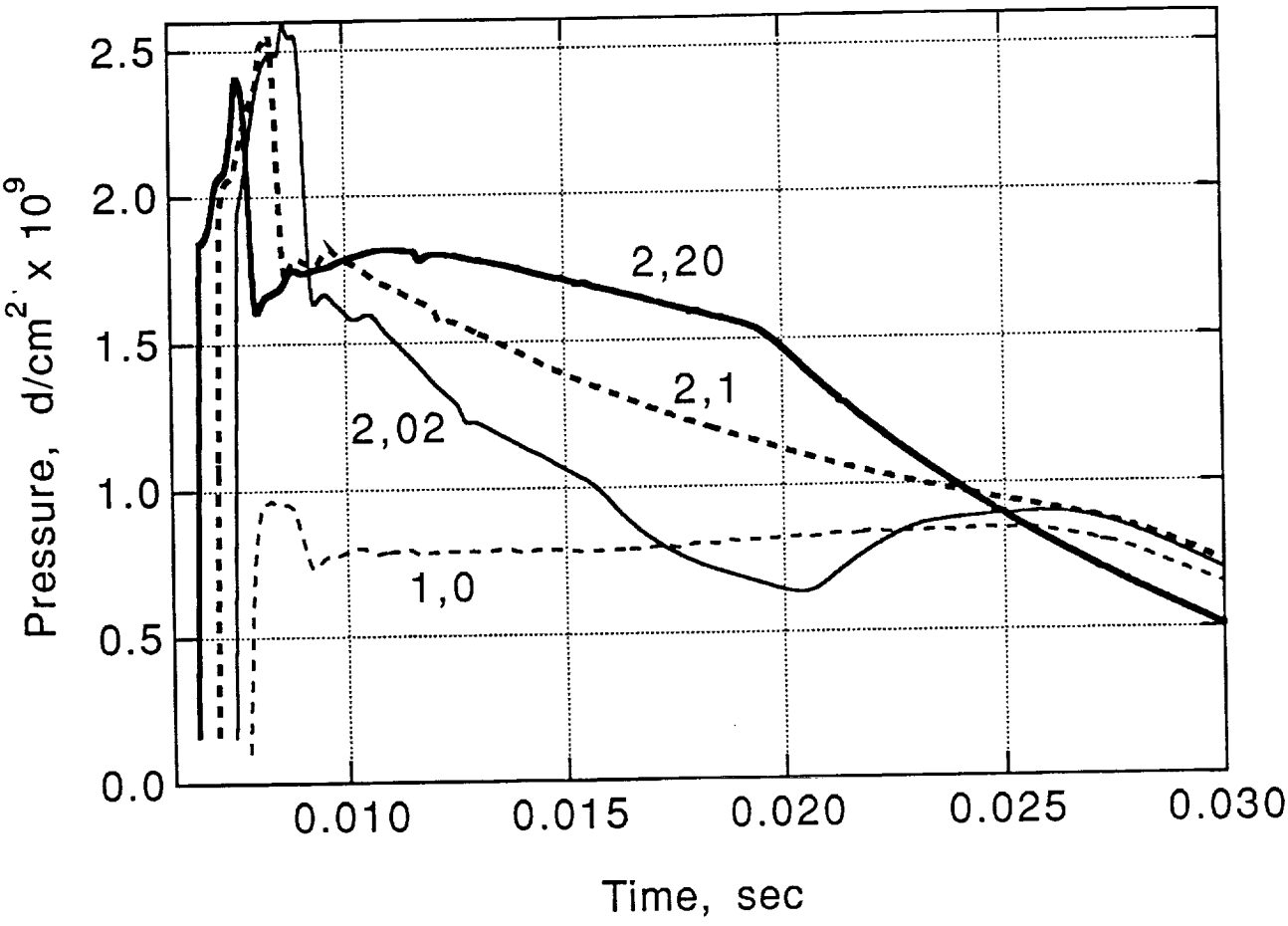

Fig. 6
D. W. Bogdanoff
J.-L. Cambier

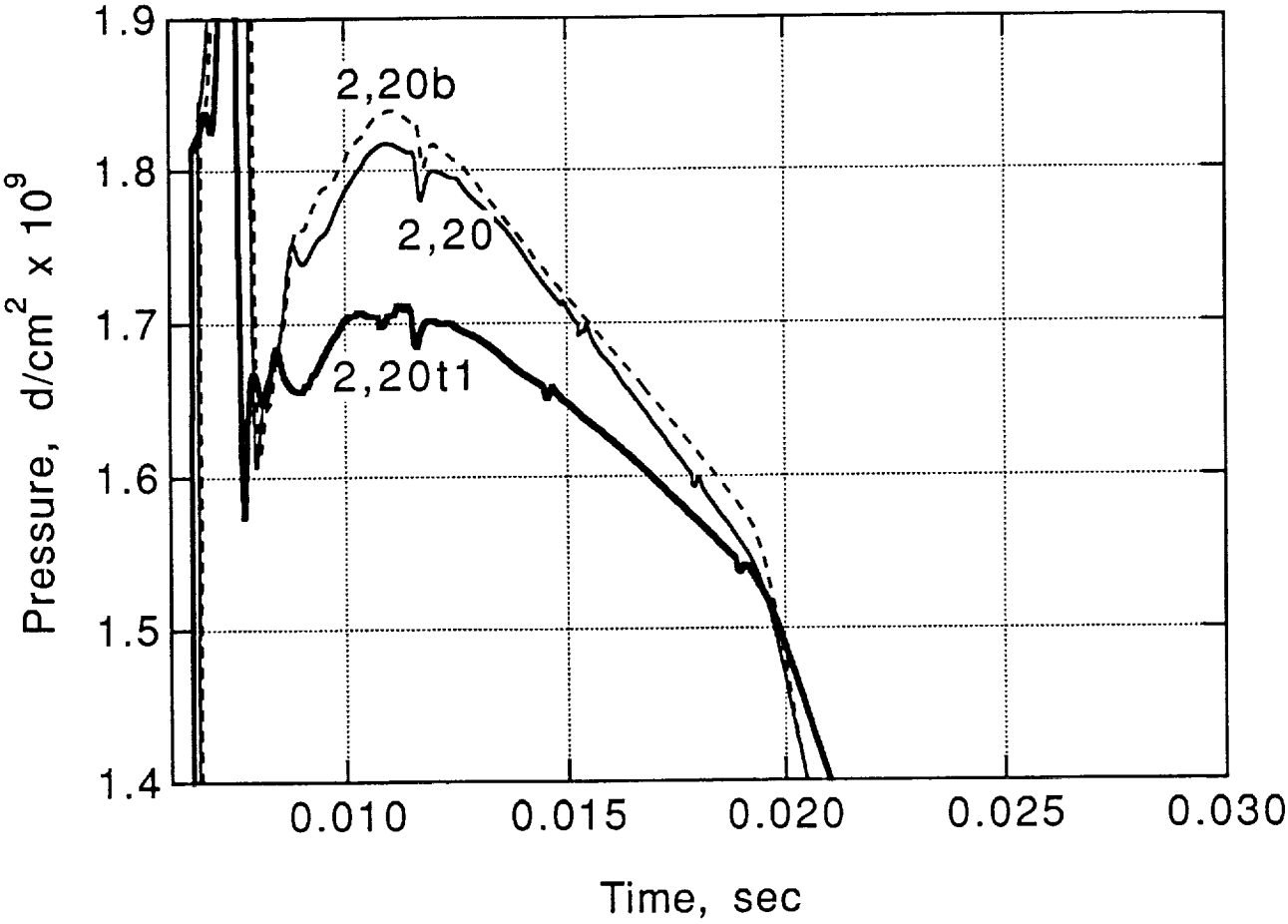

Fig. 7
D. W. Bogdanoff
J.-L. Cambier

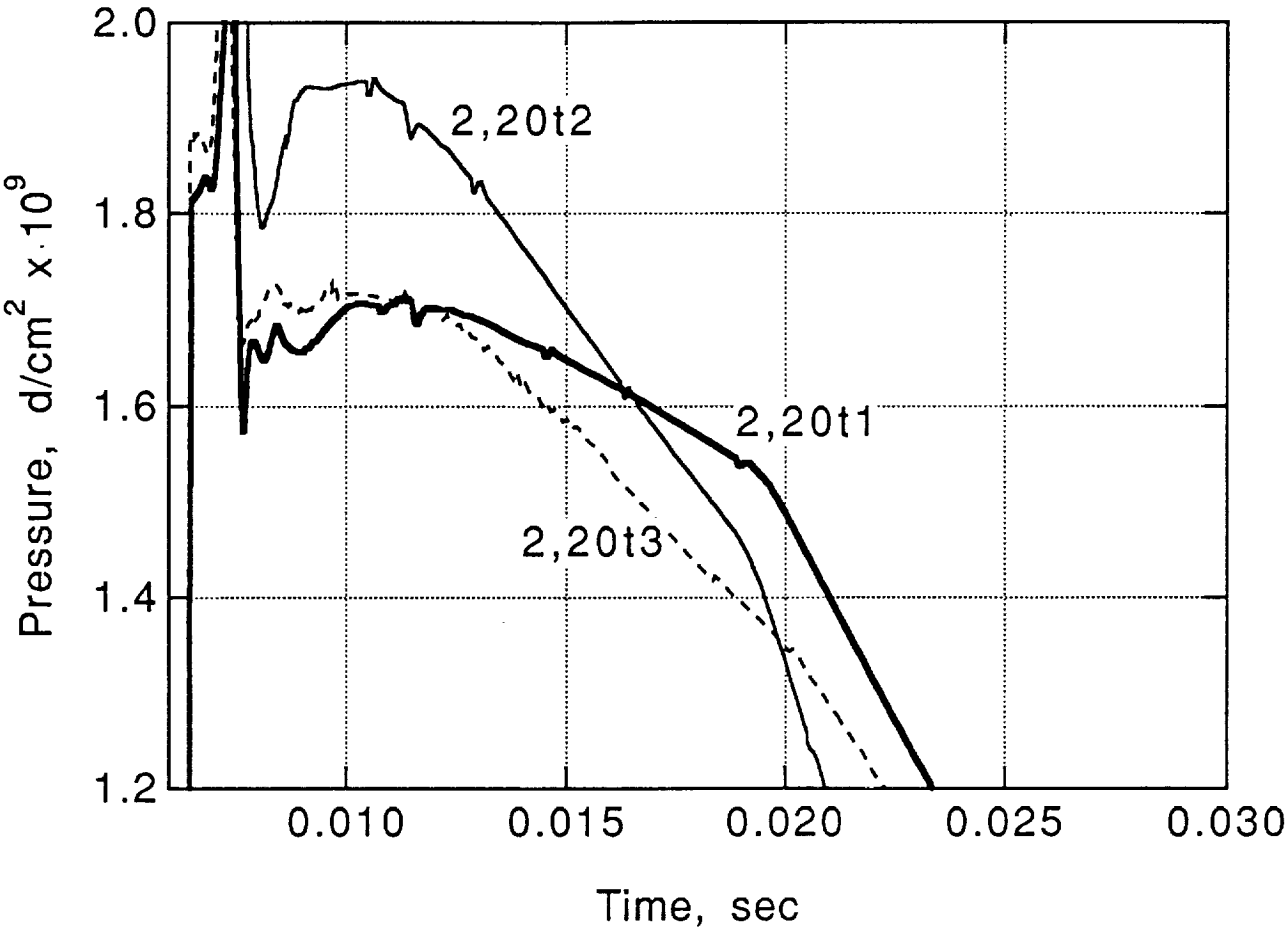

Fig. 8
D. W. Bogdanoff
J.-L. Cambier

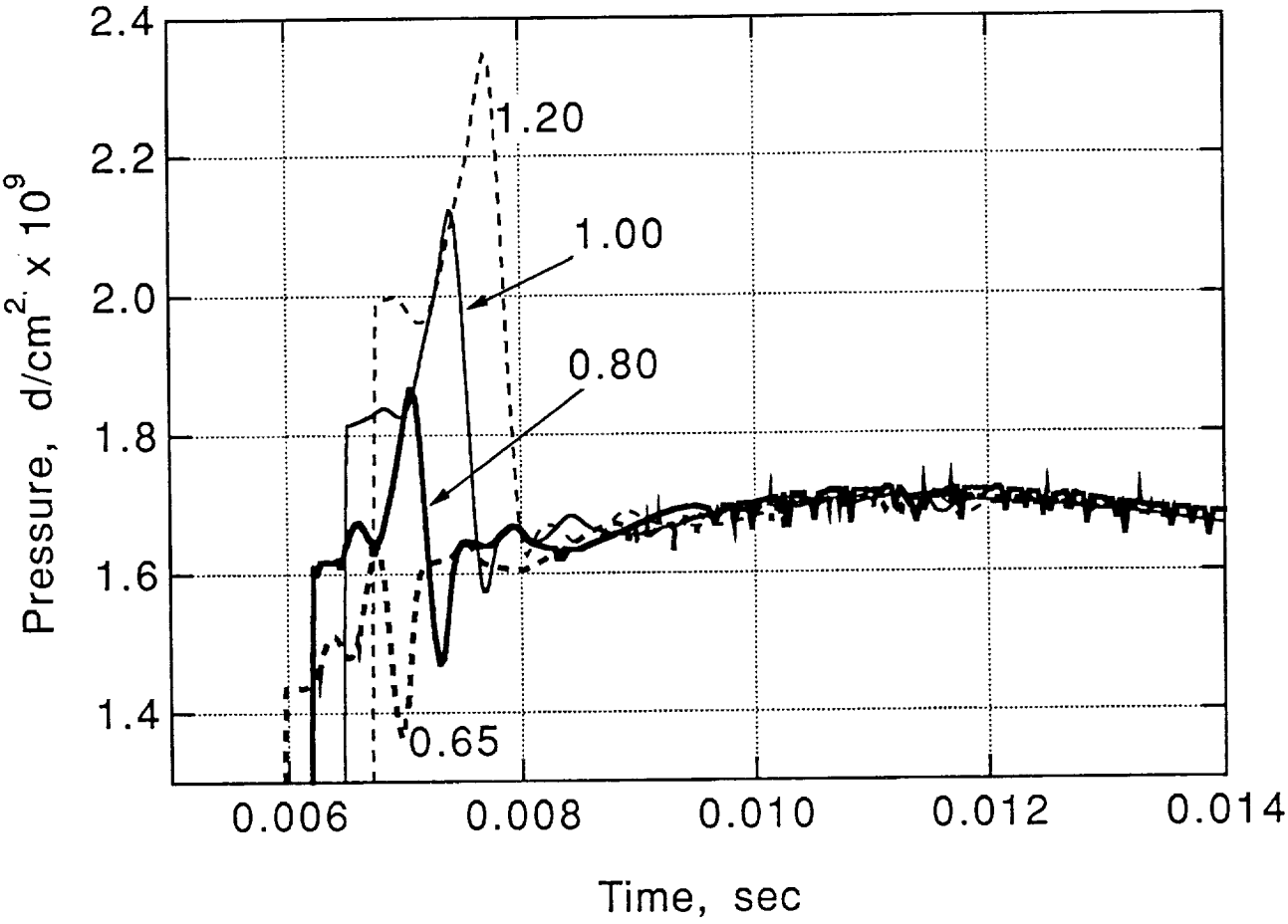

Fig. 9
D. W. Bogdanoff
J.-L. Cambier

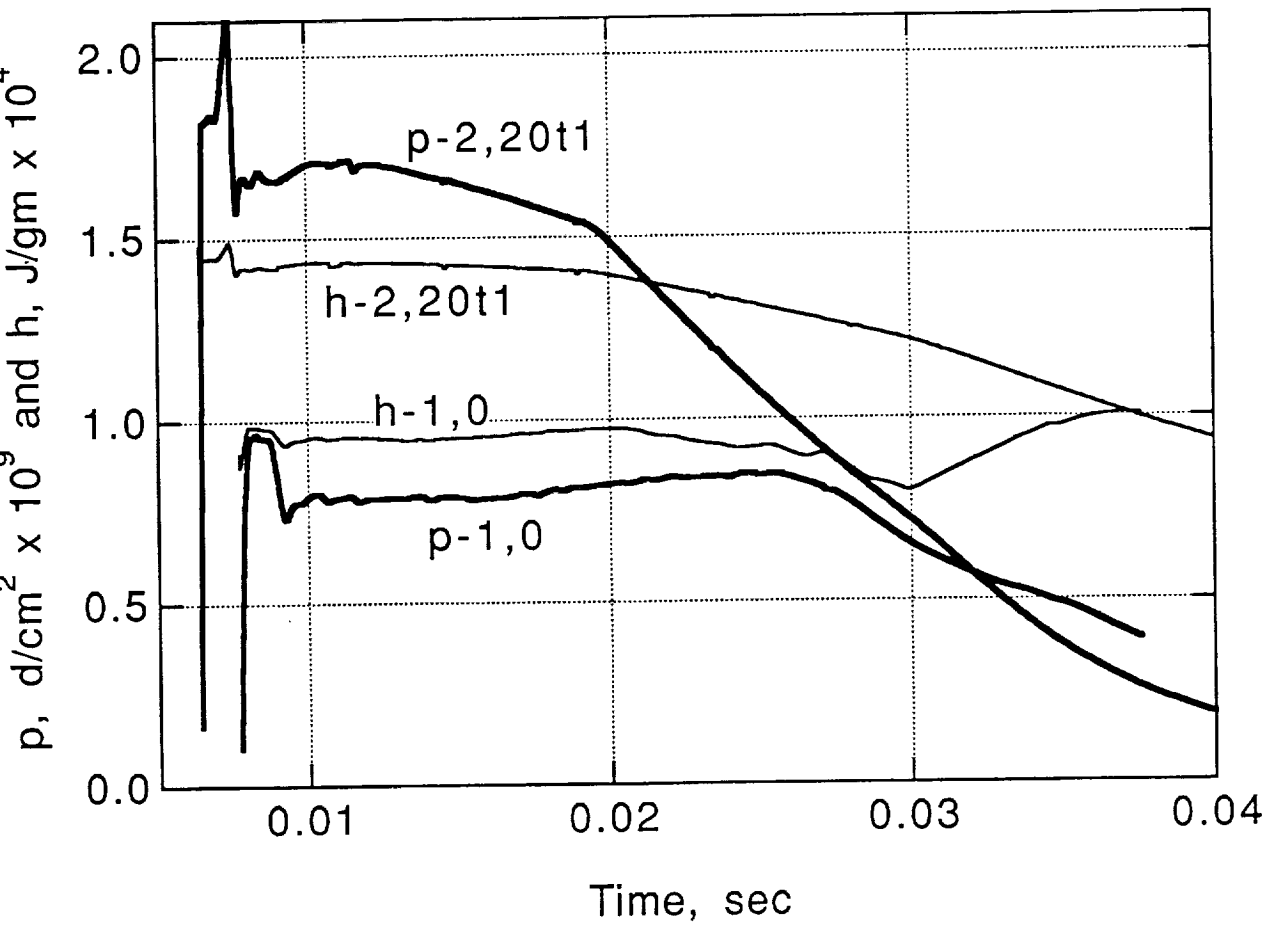

Fig. 10
D. W. Bogdanoff
J.-L. Cambier

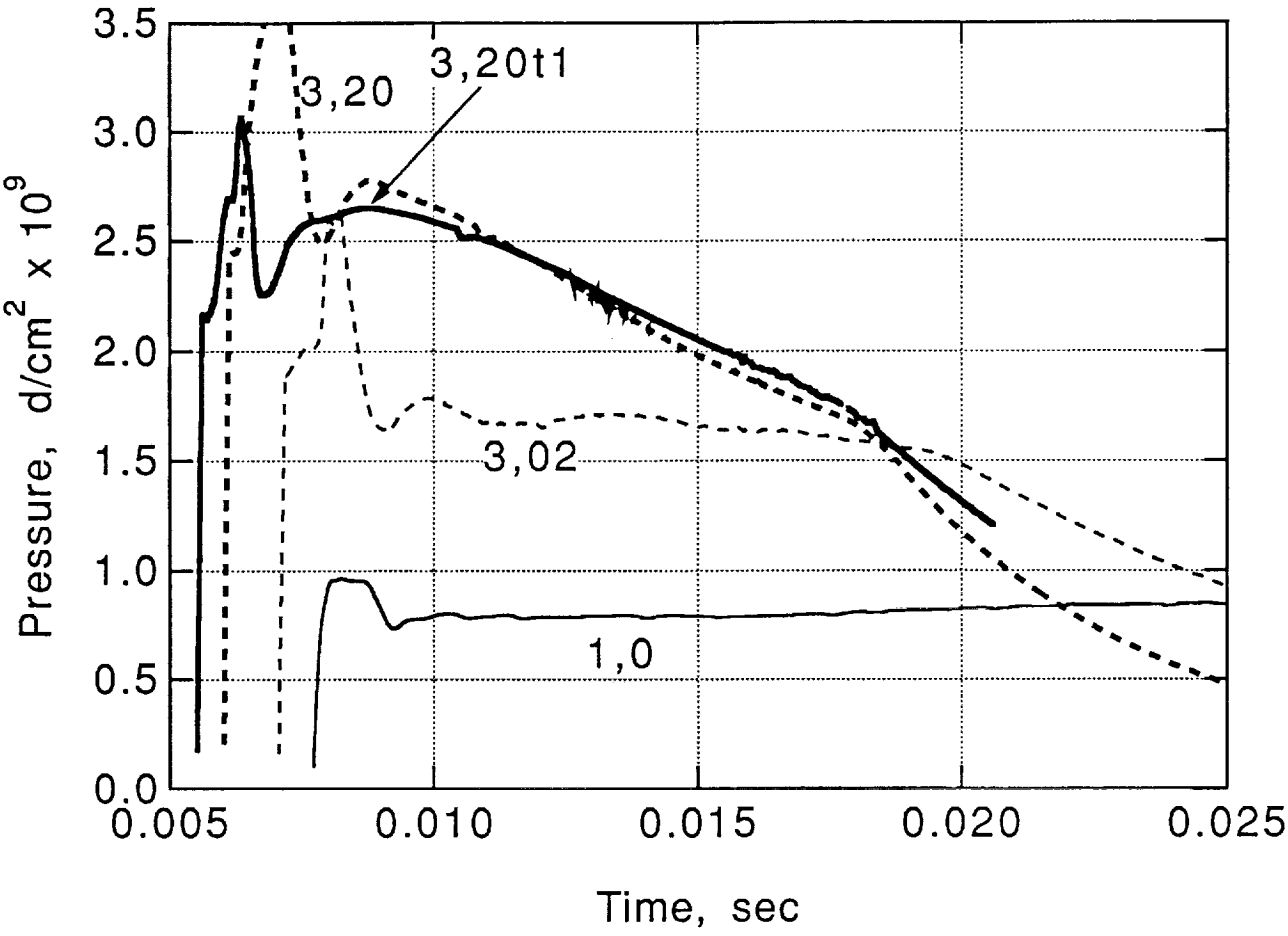

Fig. 11
D. W. Bogdanoff
J.-L. Cambier

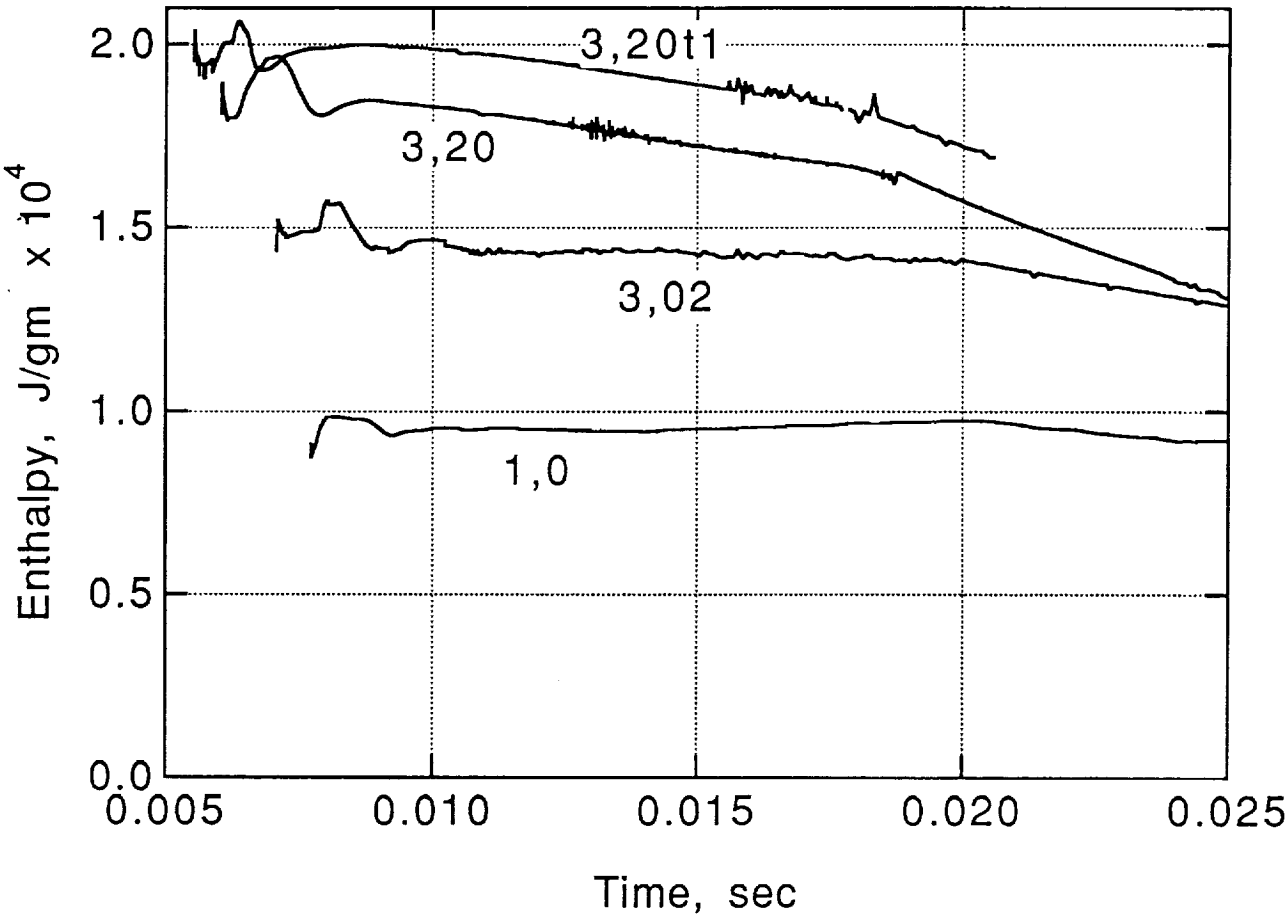

Fig. 12
D. W. Bogdanoff
J.-L. Cambier

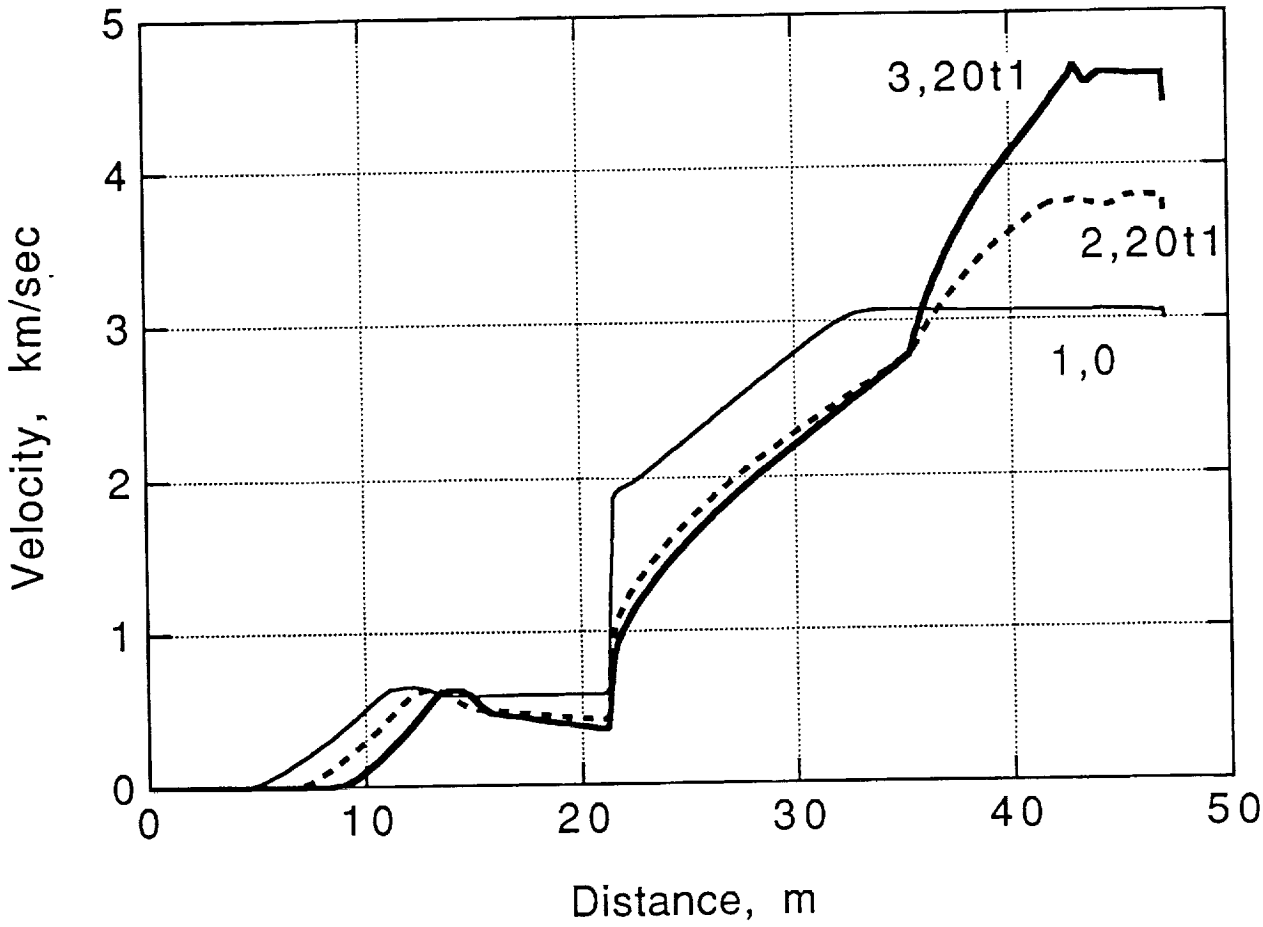

Fig. 13
D. W. Bogdanoff
J.-L. Cambier

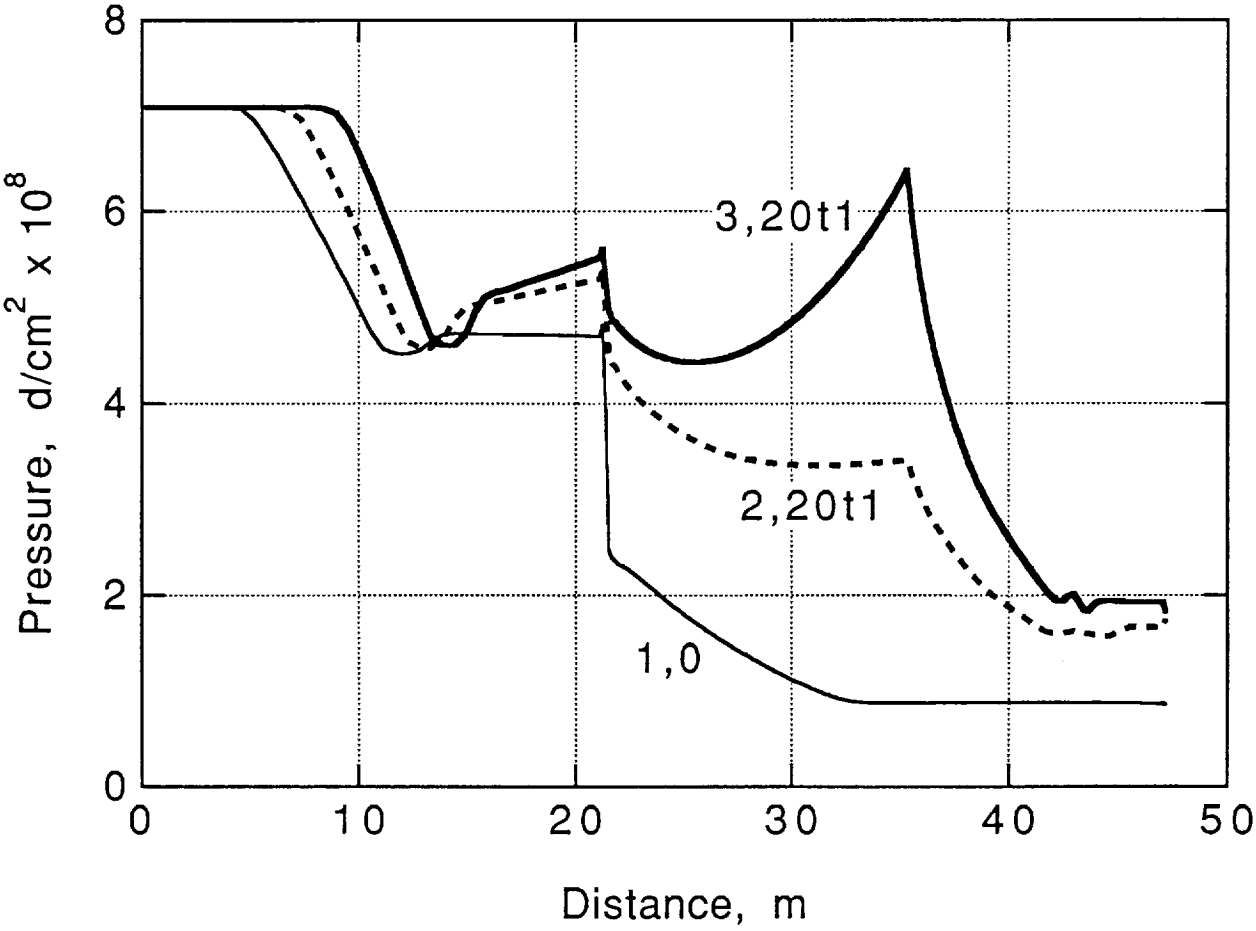

Fig. 14
D. W. Bogdanoff
J.-L. Cambier

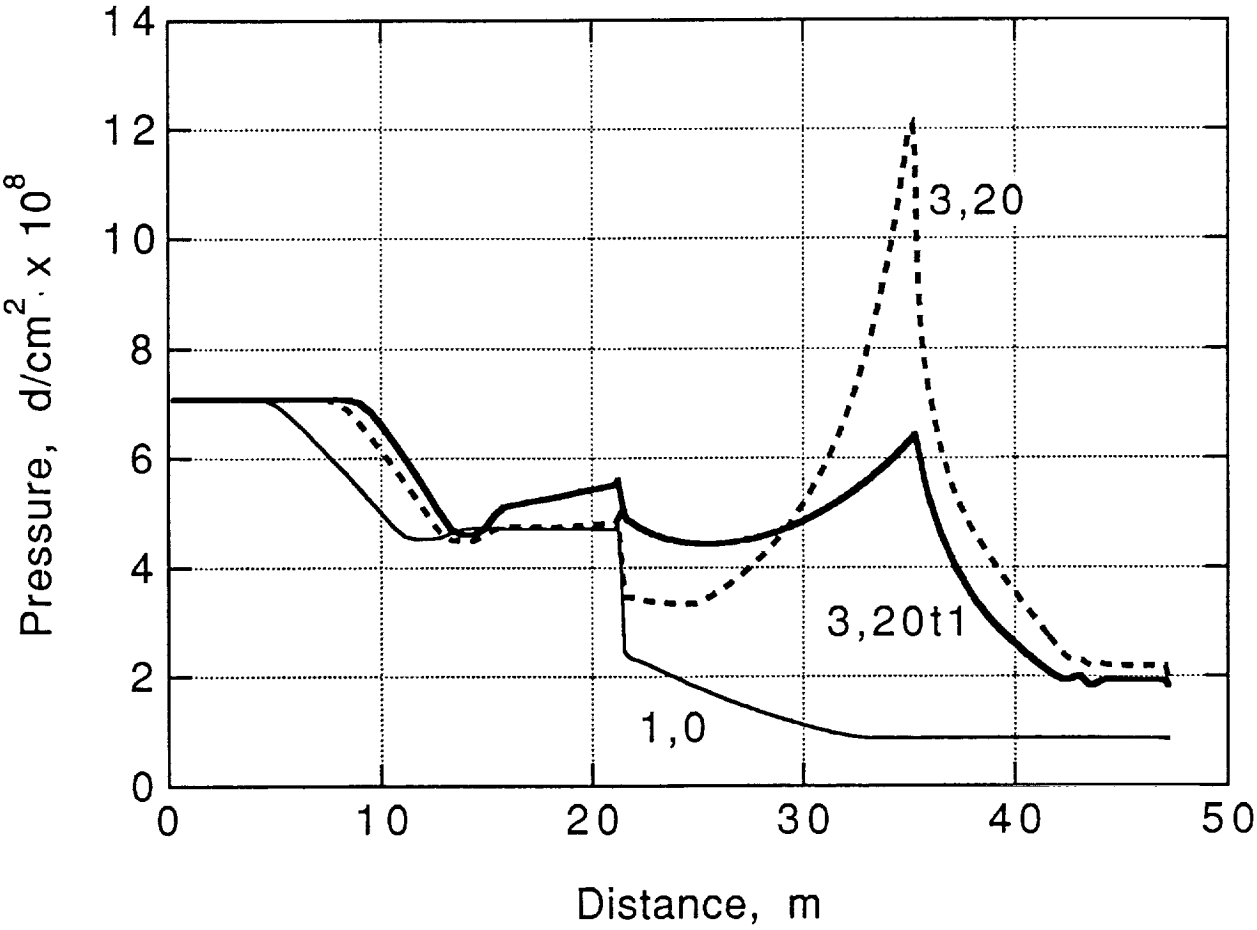

Fig. 15
D. W. Bogdanoff
J.-L. Cambier

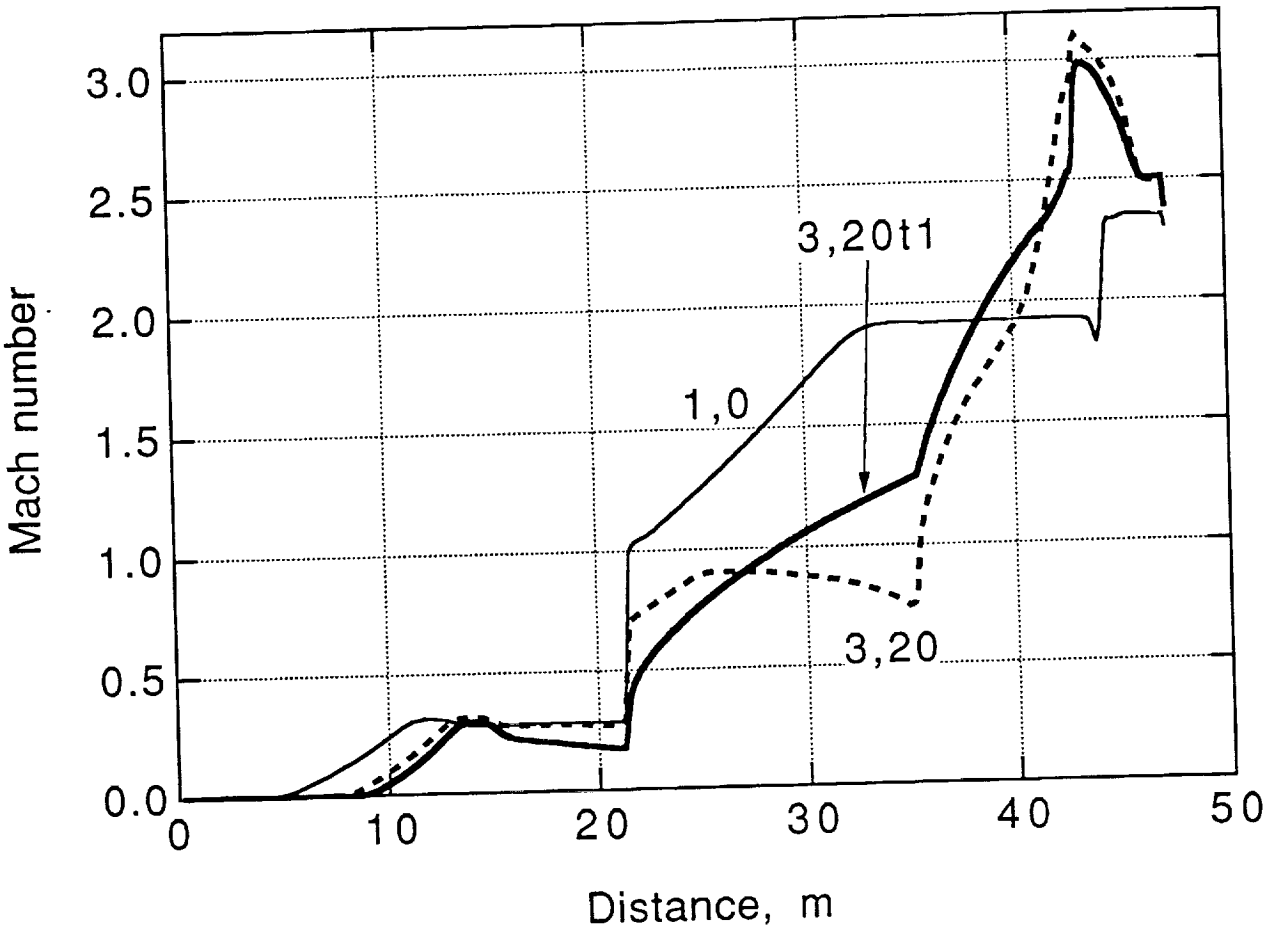

Fig. 16
D. W. Bogdanoff
J.-L. Cambier

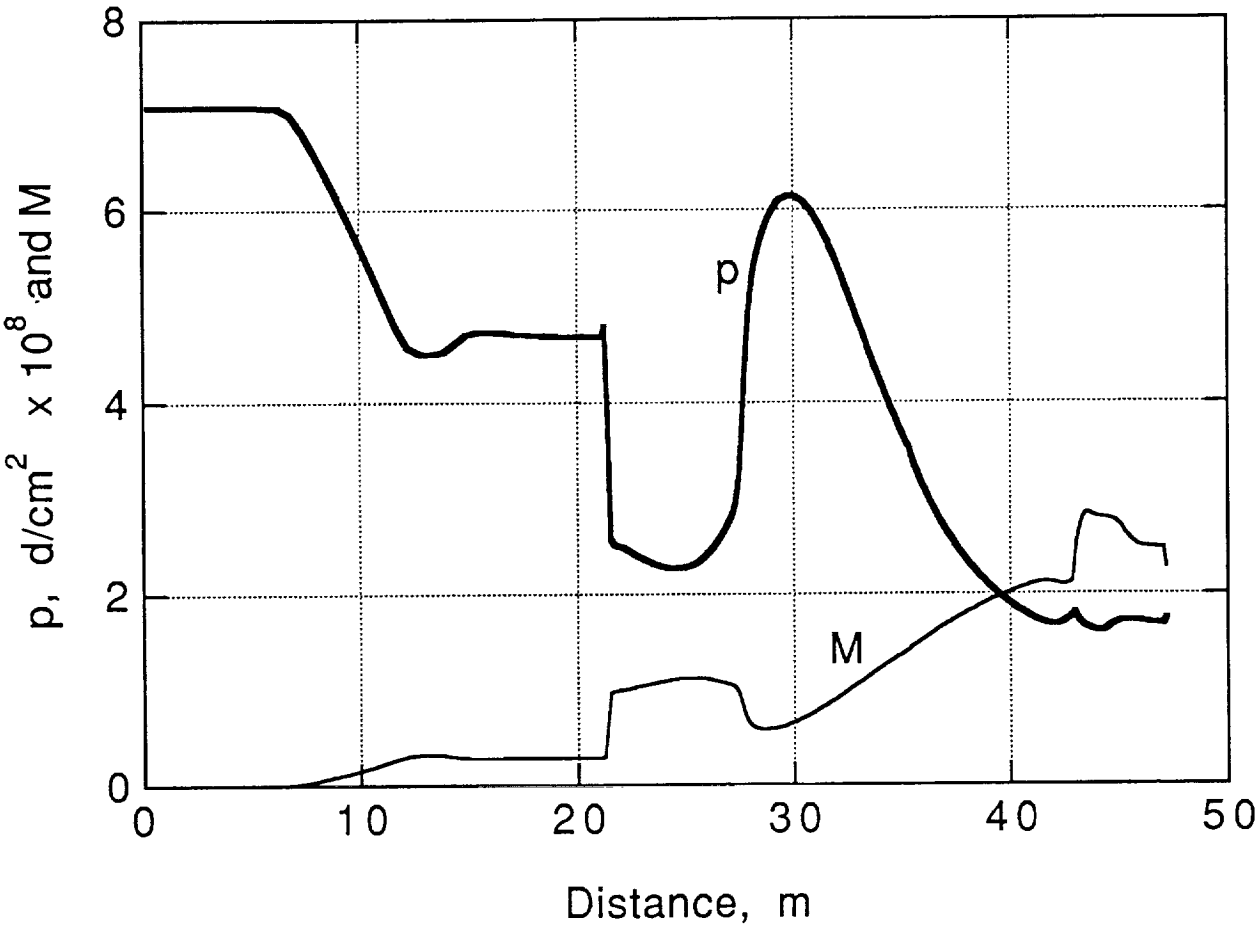

Fig. 17
D. W. Bogdanoff
J.-L. Cambier

AIAA-92-3288

30 DEGREE INJECTORS AT HYPERVELOCITY CONDITIONS

Mark P. Loomis
MCAT Institute, San Jose, CA

Horacio A. Zambrana and David W. Bogdanoff
Eloret Institute, Palo Alto, CA

Tim C. Tam, John A. Cavolowsky, and Mark E. Newfield
NASA-Ames Research Center, Moffett Field, CA

Robert D. Bittner
Analytical Services and Materials, Inc., Hampton, VA

AIAA/SAE/ASME/ASEE
28th Joint Propulsion Conference and Exhibit
July 6-8, 1992 / Nashville, TN

30 DEGREE INJECTORS AT HYPERVELOCITY CONDITIONS

by

Mark P. Loomis*
MCAT Institute, San Jose, CA 95127
and
Horacio A. Zambrana* and David W. Bogdanoff **
Eloret Institute, Palo Alto, CA 94303
and
Tim C. Tam*, John A. Cavolowsky*, and
Mark E. Newfield*
NASA-Ames Research Center, Moffett Field, CA 94035
and
Robert D. Bittner*
Analytical Services and Materials, Inc., Hampton, VA 23665

ABSTRACT

A series of hydrogen-air mixing and combustion experiments were conducted at high enthalpy conditions at the NASA-Ames Research Center 16-Inch Shock Tunnel. The goals of the tests were to demonstrate the facility capability for high speed propulsion testing and to obtain limited data on the performance of 30° flush wall injectors. The experimental results were compared with CFD analysis.

INTRODUCTION

The rebirth of hypersonics research in the U.S. has stimulated the need for ground test simulation of supersonic combustion ramjets at high flight Mach numbers. Until recently, very little data was available at Mach numbers greater than about 8. Ground testing above Mach 8 requires high pressure, high enthalpy facilities such as shock tunnels[1-3] , and expansion tubes.[4] These facilities have test times which are free of driver gas contamination on the order of a millisecond. A notable exception to the short duration, high enthalpy facility tests is a recent set of experiments in the Mach 9-12 regime at the 100 MW arcjet facility at NASA-Ames[5].

As the need for data at high enthalpy conditions becomes more important in the design of scramjet engines, additional facilities are being brought on line for propulsion testing. This paper presents the results of the first high speed propulsion related experiments in the Ames 16-Inch Shock Tunnel simulating combustor inlet conditions at approximately Mach 14. The test program was designed as an initial entry to demonstrate the facility capability and to obtain limited data on the characteristics of 30° flush wall hydrogen fuel injectors.

FACILITY

A brief description of the Ames 16-Inch Shock will be presented. Complete details of its operation and flow characteristics can be found in Refs. 6 & 7. The NASA-Ames 16-Inch Shock Tunnel (Fig. 1) has a 21 m long, 43 cm diameter driver tube and a 26 m long 30 cm driven tube. The facility receives its name from the 16 inch naval cannons that were used to construct the driver tube. The nozzle is contoured and designed for a nominal Mach number of 7 at low enthalpy, however due to the high enthalpy conditions the actual free stream Mach number was about 5.8. The facility was originally built

* Research Scientist, Member AIAA
** Research Scientist, Associate Fellow AIAA

as counterflow to a ballistic range and not as a stand alone shock tunnel. The test section in this entry was at the last station of the ballistic range and was located 2.6 m downstream of the nozzle exit. The test section diameter was 0.99 m. For the present tests, the nozzle was operated with a test section to throat area ratio of 170; however, the nozzle can be run at area ratios as low as 95.

The combustion driver is operated with a $2H_2$ + $1.17O_2$ + 9.36He gas mixture. The gas is ignited by using four 0.019 cm diameter tungsten wires strung the length of the driver tube. The wires are connected in parallel and heated to 2000 K by the discharge from a capacitor bank. The ignition produces smooth combustion with a rise time of approximately 25 ms and produces a pressure rise of approximately 8:1. The maximum pressure ratings of the driver and driven tubes are 680 atm. For the data presented here, the final after burn pressure in the driver tube was 272 atm. Flat, scored diaphragms are used which self break at the completion of the driver burn. The test time which is free of driver gas contamination for the conditions used here was estimated to be 3-5 ms.

TEST ARTICLE & INSTRUMENTATION

The tests were performed on a wedge model 38 cm long, with a 46 cm wide leading edge and with the instrumented surface inclined 11° to the free stream flow. The model is shown in Fig. 2. A spanwise row of five sonic 0.305 cm diameter injector ports was located at 22 cm from the leading edge. The injectors were inclined at 30° to the model surface and were 8.33 diameters apart.

The model instrumentation consisted of pitot probes, static pressure gages and heat flux gages. At the leading edge there was a two probe pitot rake and at the trailing edge there was a seven probe rake. A total of 12 Kulite surface pressure transducers were used, as shown in Fig. 2. In addition there were two hydrogen injector plenum pressure transducers, and two hydrogen flow venturi pressure transducers. The heat transfer gages included 10 Type E coaxial thermocouples, 2 thin skin slug calorimeters and two platinum thin film gages. The gages were arranged mainly in three streamwise rows with a 3.81 cm streamwise separation. The center row of transducers and the trailing edge pitot probe were in line with an injector port and the outboard rows were midway between ports.

Data Acquisition

The data-acquisition system (DAS) included 68 channels of 1-MHz digitizers (LeCroy 8210) with 16 kbytes memory per channel, and 20 channels of digitizers (LeCroy 6810) with up to 5-MHz sampling rate and 512 kbytes of memory per channel. The system was controlled by a stand-alone Macintosh IIfx computer. Amplifiers with gains of 10 and 100 and frequency responses of 70 kHz were used.

Flow Visualization

A versatile laser holographic interferometer (see Fig. 3) was used for flow visualization in the spanwise direction. The technique used was a dual-plate, double-pass system. The dual-plate technique provides system insensitivity to optical nonuniformities and provides flexibility in reconstruction. The double-pass technique provides increased sensitivity at lower pressures. The light source was an injection-seeded, frequency-doubled, Nd:YAG laser producing pulses at 10 Hz, 532-nm wavelength, 200-mJ pulse energy, and 6-nsec pulse width. The beam distribution optics were located directly adjacent to the optical access port at the test section, while the laser light source was remotely located and directed to the test section by a series of mirrors.

TRANSVERSE INJECTION

Transverse injection of hydrogen through discrete holes for application in scramjet combustors has been investigated by several authors, mostly in low enthalpy continuous flow facilities[8-12]. Due to the long run time in these types of facilities, in-stream measurements such as gas sampling, pitot surveys and static pressure surveys were possible. These results have been used for extensive calibration of CFD codes. Since data at high enthalpy conditions is very sparse and in-stream data such as species concentrations is

very difficult to obtain, it would be desirable if the cold flow mixing results could be extended to high enthalpy conditions. In one of the low enthalpy transverse injection experiments, McClinton[10] investigated an array of five injectors inclined at angles from 30° to 90° and found the best mixing and penetration for lowest injection angles. The lower angles were also found to produce less total pressure loss. Another significant advantage of injection at low angles for scramjet applications is that the downstream axial momentum of the jets can produce a sizable fraction of the net engine thrust. Thus, injection at 30° was chosen for this investigation.

TEST CONDITIONS & MATRIX

Tests were performed at the test conditions shown in Table 1. The shock tube conditions were calculated using standard equilibrium shock tube relations. The calculation used the measured shock speed and driven tube initial conditions to compute the conditions behind the reflected shock, and then performed an isentropic expansion from the calculated pressure to the measured pressure to account for the non-tailored interface. The enthalpy of 9.5 MJ/kg is roughly equivalent to the total enthalpy at a flight Mach number of 14. The nozzle exit conditions were calculated using a quasi-1-dimensional nonequilibrium code.[13] The nozzle exit Mach number was approximately 5.8 for these conditions and the flow behind the shock wave had a Mach number of 4.4. The static pressure on the surface was 0.25 atm and the temperature after compression was about 1800 K. The boundary layer thickness was estimated to be on the order of 1 mm. Though the pressure is lower than typical, the velocity, temperature and Mach number are close to the combustor inlet conditions of a scramjet engine at Mach 14.

Three types of tests were run: runs with air flow and no injection (tare); runs with H_2 injection into N_2 flow (mixing), and runs with H_2 injection into air (combustion). An important parameter regarding the penetration of transverse jets is the momentum flux ratio of the injectant to that of the free stream, i.e., $\bar{q} = (\rho V^2_I / \rho V^2_\infty)$, where V is the velocity, and ρ is the density. The fuel will penetrate further into the free stream for higher values of this ratio. For these experiments, the dynamic pressure of the hydrogen jets was approximately equal to that of the shocked flow parallel to the wedge ($\bar{q}$ = 1 condition) for all injection runs except one, for which it was twice as high ($\bar{q}$ = 2 condition). The fuel total pressure for the nominal $\bar{q}$ = 1 condition was 8.8 atm and the discharge coefficient of the orifices was 0.78. Ten runs, including several repeated runs, were made.

CFD ANALYSIS

Code Description

The NASA Langley Research Center (LaRC) SPARK series of codes were used to perform the computational analysis. The two-dimensional elliptic, explicit, finite difference code was originally developed by Drummond (Ref. 15). This code was subsequently extended to three dimensions by Carpenter (Ref. 16) and this has been converted into a parabolized version by Kamath (Ref. 17). The codes have been extensively validated for a variety of flow types. Specifically, the codes have been used to model experiments involving hydrogen injection into a supersonic stream (Refs. 18-20). The codes have a choice of a second order MacCormack, a fourth order cross MacCormack, or a fourth order Gottlieb MacCormack algorithm to solve the mass, momentum, energy, and individual species mass conservation equations. The cross MacCormack algorithm was used exclusively in this investigation. This algorithm achieves fourth-order spatial accuracy at steady state although it is only second-order accurate in space and time during the transient development. Additionally, fourth order damping terms were used which are based on pressure and temperature gradients. The elliptic codes can be run in a time accurate or a local time stepping mode which accelerates the convergence to a steady state solution. Unfortunately, at this time it is impractical to solve a three-dimensional problem with a "real time" approach. Also, the programs include an internal grid generation capability developed by Smith & Weigel (Ref. 21) which were used in this analysis.

The SPARK codes employ a variety of turbulence models. For the analysis contained in this paper, the Baldwin-Lomax (Ref. 22) algebraic model was used. This method has been widely used due to its ease in application. Algebraic methods simply model turbulence as an increase in the transport coefficients. To determine the turbulent portion of the viscosity, or eddy viscosity, a length and velocity scale must be determined. This model bases the velocity scale on the vorticity distribution and the length scale on the distance from the wall. Although this model is not appropriate for injection flowfields, it has been calibrated to some degree for jet mixing through the use of the turbulent Schmidt number as reported by Riggins (Ref. 23). Recently, studies have been performed successfully using a turbulent Schmidt number of 0.5 (Refs. 18-20) and this value has been utilized in this study. Also, to prevent the jet induced vorticity from creating unphysically high turbulent viscosities the eddy viscosity was limited to 1000 times the laminar viscosity. Other models such as the k-e and Reynolds stress have recently been developed and are now in place in some versions of the code. Studies are now underway to evaluate these models for injection and combustion flowfields.

The SPARK codes have a generalized chemistry package wherein the source term can be treated implicitly and the capability exists to include any number of reactions The reacting portion of this work was performed using the seven-reaction-seven-species finite rate model which is a subset of a model used by Drummond (Ref. 15). The reaction rate constants for the chemistry model are given in Table 2. For all the calculations, SPARK carries the nitrogen as an inert species and its value is determined by subtracting the summation of the mass fractions of all other species from one..

Computational Approach

The computational approach taken in this work was typical of injection flowfields. It consists of a sequence of axial blocks as illustrated in Fig. 4. The purpose of the blocking is to only use a level of code complexity that is required in any given region of the flow. The inflow conditions are as specified in the figure. The free stream velocity was broken into two components, one parallel and one perpendicular to the wedge surface to facilitate the modeling of the wedge. For the first zone, the PNS code was run from the leading edge of the test section to five injector diameters upstream of the jet. Since the geometry has no lateral variation upstream of the injection point, this region was solved two-dimensionally. The second zone was solved using the three-dimensional elliptic code. The injection conditions are listed on Fig. 4. All of the elliptic cases were solved using local time stepping to accelerate the convergence to a steady state. As in many problems of this type, the character of the reacting flowfield is no better than quasi-steady so convergence requirements for these cases are in reality relatively unchanging mean values for wall functions such as pressure and skin friction and cross-sectional integrated parameters such as fuel mixing efficiency and mass conservation. The outflow plane from the elliptic solution was then passed to the final zone at a plane five injector diameters downstream of the injection point. Finally, the 3-D PNS code was run from this point to the end of the wedge

Grids and Boundary Conditions

For the upstream PNS solution, a grid of 5 x 80 was used. The domain height was set large enough to completely capture the wedge leading edge shock. These grids were generated using the capability in SPARK and were clustered along the wedge surface. The wedge surface was treated as a no-slip boundary, with a wall temperature of 300 K and non-catalytic kinetics.

The grid for the injection region was of the dimension (71 x 51 x 80). The jet orifice was modeled as a rectangle using two hundred and seventy three nodes with specified temperature, pressure, and velocity. The discharge coefficient was accounted for by a slight change in incoming jet pressure. No slip boundary conditions were again applied on the wedge surface. This grid uses the outflow from the PNS code as an inflow condition. In addition, a supersonic boundary condition was imposed on the outflow plane The lateral domain extended from the jet centerline to between centerlines with both lateral

boundaries modeled as symmetry planes. The resulting lateral domain was 1.27 cm wide. The grid used clustering at the wedge surface in a vertical sense and at the injector in an axial sense. The downstream grid utilizes the same cross-section as the elliptic zone and continues to the end of the wedge. This grid used the plane from the elliptic solution as an inflow condition and was clustered in a similar manner to the other grids.

RESULTS

Facility Performance and Data Quality

One of the primary goals of the experiments was to verify the the facility compatibility for high speed propulsion testing. The key issues in this regard are flow quality, flow contamination, test time and repeatability. Typical data traces are shown in Fig. 5 in this regard. Fig. 5a is a trace of the nozzle reservoir pressure. The trace shows that the pressure is roughly constant for a period of 18 ms after which the pressure drops due to the arrival of the reflection of the expansion fan from the far end of the driver tube. However, it is well known that mixing of the driver gas and the driven gas at the contact surface reduces the period of uncontaminated test time. Previous results have estimated this period to be from 3-5 ms for these conditions in this facility. Fig. 5b shows a typical facility nozzle static pressure trace located at an area ratio (A/A^*) of 45 showing a region of steady pressure followed by a slight drop off. This drop off in static pressure tends to correlate with the arrival of the driver gas due to the fact that the driver gas has a much higher value of the ratio of specific heats. Fig. 5c is a plot of the static pressure on the model surface which also shows a steady period of around 5 ms. The pitot pressure trace in Fig. 5d, taken at the model trailing edge, also shows a reasonably constant period of 5 ms. At most transducer locations, variations of static and pitot pressures and heat flux between the repeat runs ranged from 2% to 7%.

Reference 14 summarizes certain rules of thumb regarding flow establishment time for pulse facility testing. The important parameter is the ratio of the slug length, which is the expanded extent of the slug of uncontaminated gas in the test time t, to the characteristic length of the model L. The criteria are $tu/L > 2$ for attached turbulent flow, and $tu/L > 3$ for attached laminar flow, where u is the flow velocity. For the conditions here, the slug length based on a test time of 3 ms (which represents a conservative estimate of the test time) is about 12 m. Based on this criteria, the facility should be able to test large scale combustors on the order of several meters long. For this experiment, with a model length scale of ~0.5 m, this criteria is easily met and the flow can be said to be fully established in the duration of the uncontaminated test time.

Flow Visualization

The holographic interferograms were reconstructed as shadowgraphs and finite fringe interferograms. Examples of finite fringe interferograms are shown in Figs. 6 and 7 for the cases of tests with and without injection of hydrogen into air. Fig. 6 shows that the shock from the leading edge of the model falls between the fifth and sixth pitot heads, which is what was expected from the free stream conditions and the turning angle of 11°. The fringes are curved in the shock layer most likely due to the three dimensional nature of the flow field around the model.

Fig. 7 shows the wedge shock, the boundary layer, the hydrogen plume and the shock system attached to the plume for the case of hydrogen injection into air with $\bar{q}=1$. The plume shocks begin to merge with the wedge shock upstream of the model trailing edge and force the wedge shock somewhat upwards for cases with hydrogen injection. Fig. 8 is a comparison of a shadowgraph reconstruction corresponding to the same run as in Fig. 7, with a plot of the path averaged density contours from the computation. The fuel penetration height in the computation is defined as the .005 H_2 mass fraction contour, while the fuel mixing layer shown in the shadowgraph corresponds to a region of high density gradients. The comparison shows that the shock structure in the computation agrees with the experiment, however it appears as if the fuel penetrates further in the computation than the experiment. However, this may not be a valid comparison since the low concentrations

associated with the 0.005 H_2 mass contour may not be discernable in the shadowgraph. For the case of injection with matched dynamic pressure, the distance to the edge of the mixing layer in the shadowgraph at the pitot rake, h, was seen to be about 1.3 cm, which corresponds to h/d = 4.3, where d is the jet diameter. The penetration of hydrogen plume was seen to be substantially greater for the higher injector dynamic pressure condition ($\bar{q}$=2), as expected. The edge of the mixing layer at the pitot rake was seen to extend past the third probe, approximately 2.2 cm from the surface which corresponds to h/d=7.2. The strength of the injector bow shock was also greater than for the case with $\bar{q}$ =1.

Pitot Pressure

Figure 9 shows the trailing edge pitot pressure profiles for the tare (no injection), mixing and combustion runs at $\bar{q}$=1 and combustion conditions at $\bar{q}$=2. There were seven pitot heads, numbered outwards from the wedge surface. The sixth head was inoperative for the duration of the tests. All pressure data was averaged over 4 ms, starting shortly after arrival of the starting shock. The tare run shows the wedge shock located outside of the fifth probe head, in agreement with the flow visualization. The impact pressure remains high all the way down to the first probe head. For the mixing and combustion runs, the low dynamic pressure region of the hydrogen plume is apparent adjacent to the wedge surface. It covers the lowest two probe heads for $\bar{q}$=1 and the lowest 3 heads for the $\bar{q}$=2 condition. The plume pitot pressure appears to be about 10% lower for the $\bar{q}$=1 combustion run than for the mixing run. This can be explained by the higher total pressure loss associated with combustion.

For all runs with injection, the impact pressure outside the H2 plume and inside the wedge shock is greater than the corresponding values from the tare run. This is most likely due to the additional compression of the free stream by the plume shock system, which is of course not present in the tare run.

Heat Flux Measurements

Three types of heat flux gages were installed on the model for comparison and evaluation purposes. Platinum thin film gages are commonly used in pulse facilities, however previous experience in the facility nozzle indicated that these gages might not survive the 18 ms period of high impact pressure, which is longer than other typical pulse facilities. This proved to be true for this application also. After the second shot, the platinum thin film gages had been destroyed, showing infinite resistance. For each run, typically less than 2 of the coaxial gages would show anomalous behavior. They would give good data at the start of the run and then open up to infinite resistance. However, these gages could be restored to service by abrading them with an abrasive eraser and burnishing them with a rounded steel rod. At the end of the test series, all coaxial gages were still operational. One slug calorimeter failed during the ninth test run; the other remained operational throughout the test series. Based on this performance, the coaxial gages were a more robust choice for heat flux measurements.

The two slug calorimeters showed agreement with the coaxial thermocouple data to within a few percent, however the slug calorimeters have a much slower response time (~.5 ms) than the coaxial thermocouples, hence only the thermocouple data were presented in Figure 10. Since coaxial thermocouples gages measure surface temperature, the data was reduced to heat flux by the standard equations for transient heat flux to a semi-infinite slab. An automated data reduction scheme was incorporated into the data acquisition system to reduce the raw data to heat flux.

Figure 10 shows the heat flux for the tare (no injection), mixing and combustion conditions at $\bar{q}$=1. The Reynolds number based on the distance to the injectors for the flow compressed by the shock was ~ 0.5 *10^6, which is consistent with that of a laminar boundary layer. The heat flux in this region agrees very well with laminar predictions. For the tare run, along the centerline (Fig 10a), the heat flux rises greatly downstream of the injectors, indicating tripping of the boundary layer by the injector holes.

(Without tripping, the boundary layer should remain laminar all along a model of this size.)

Midway between the injectors (Fig 10b), the heat flux continues to drop downstream of the injectors until x = 32 cm, where it begins to rise somewhat. It is likely that this far downstream, the effect of the tripping of the boundary layer has spread in the spanwise direction sufficiently to effect the outboard gages. With injection, just downstream of the injectors (x = 23.5 cm) high heat flux levels are seen along the centerline, but not midway between the injectors. It is therefore likely that the plume shock does not reach the latter gage. Farther downstream (x = 26.5-35 cm), midway between injectors, large increases in heat flux occur upon injection. It is assumed that these areas must be in the compressed and heated flow aft of the plume shock system. Between x=29 cm and x=35 cm along the centerline, strong hydrogen film cooling is seen along the centerline, but not midway between the injectors.

Surface Static Pressure

Figure 11 shows the surface static pressure profiles for tare (no injection), mixing and combustion runs at $\bar{q}$=1 and combustion runs at $\bar{q}$ =2. Fig. 11a is for the centerline transducers, in line with an injector, while Fig. 11b is for the two outboard rows of transducers, each midway between injectors.

For the run with no injection, (circle symbols), all surface pressures were within a range of 10%. Upstream of the injectors, the pressures for all runs were constant within 9%, showing no effect of the hydrogen plumes or the plume shock system. For the mixing and combustion runs at q = 1, substantial pressure rises were seen at the transducers 1.4 and 4.3 cm downstream of the injectors, showing the effect of the plume shock system. For these cases, the pressures at the transducers 10 and 12.9 cm downstream of the injectors had relaxed to the tare values. Also plotted in Fig. 11 are the CFD results for the combustion case. On the centerline, the calculated static pressure agrees with the experiment reasonably well. However, midway between the injectors the calculated values are slightly higher than those from the experiment. For the combustion run at $\bar{q}$=2, the pressure rises 1.4 and 4.3 cm downstream of the injectors were roughly twice those for $\bar{q}$=1, and a noticeable pressure rise persisted to the center transducer 12.9 cm downstream of the injectors.

From the wedge surface pressures alone, the difference between the mixing and combustion runs at $\bar{q}$=1 was quite small. Figure 12 shows a computation of the wall centerline static pressure for a mixing and a combustion case. The results show that for these conditions, the difference in pressure rise due to combustion is relatively small. This is due to the unconfined nature of the flow and the fact that the pressure upstream of the injector is low. Future tests in the facility will be operated at higher stagnation pressures, which will increase the pressure rise due to combustion.

CONCLUSIONS AND FUTURE PLANS

The results of the first propulsion related entry in the Ames 16 Inch Shock Tunnel were presented. Issues with regard to flow quality, flow contamination, test time and repeatability demonstrated the facility capability for high speed propulsion testing. Limited data on 30° flush wall hydrogen fuel injectors was obtained and the results were compared with a 3-dimensional Navier Stokes code.

Future plans are to extend the operational pressure in the driver tube up to 680 Atm which will greatly enhance the facility simulation capability. Combustor inlet static pressure above 0.5 atm at conditions representing flight at Mach 12-16 will be obtained with this improvement. A new test cabin has been built which will be used to support testing of large scale models for NASP flowpath and NASA hypersonics research.

ACKNOWLEDGEMENTS

This work was supported by NASA Ames Research Center under contracts NCC2-738 and NCC2-487. The authors appreciate the work of the Thermophysics Facility Branch in preparing the facility, especially Robert Miller, Charles Cornelison, Warren Norman, Donald Holt, Daniel Theroux, Donald Bowling

and Tom Kowalski. Thanks go to James Dunn for the fine job of instrumenting the model. The work of Dinesh Prabhu of the Computational Aerothermodynamics Section on the calculation of the laminar heat flux is also acknowledged.

REFERENCES

1. Stalker, R.J., and Morgan, R.G., "Scramjet Testing in Impulse Facilities," 8th International Symposium on Air Breathing Engines, June 14-19, 1987, Cincinnati, OH.

2. Orth, R.C., and Erdos, J.I., "The Use of Pulse Facilities for Testing Supersonic Combustion Ramjet (Scramjet) Combustors in Simulated Hypersonic Flight Conditions," 9th International Symposium on Air Breathing Engines, Sept. 3-8, 1989, Athens, Greece.

3. Dunn, M.G., Lordi, J.A., Wittliff, C.E., and Holden, M.S., "Facility Requirements for Hypersonic Propulsion System Testing," AIAA Paper 89-0184, January 1989.

4. Bakos, R.J., Tamagno, J., Rizkalla, O., Pulsonetti, M.V., Chinitz, W., and Erdos, J.I., "Hypersonic Mixing and Combustion Studies in the GASL HYPULSE Facility," AIAA Paper 90-2095, July 1990.

5. Thompson, M.W., and Friedman, M.A., "Issues Associated with Long Duration High Enthalpy Scramjet Combustor Testing," AIAA Paper 91-5104, December 1991.

6. Bogdanoff, D.W., Zambrana, H.A., Cavolowsky, J.A., Newfield, M.E., Cornelison, C.J., and Miller, R.J., "Reactivation and Upgrade of the NASA Ames 16-Inch Shock Tunnel, Status Report," AIAA Paper 92-0327, January 1992.

7. Cavolowsky, J.A., Newfield, M. Tam T., Loomis, M.P., Zambrana, H.A. and Bogdanoff, D.W., "Flow Characterization in the Ames 16-Inch Shock Tunnel," AIAA Paper 92-3810, July 1992.

8. Rogers, R.C., "A Study of the Mixing of Hydrogen Injected Normal to a Supersonic Airstream," NASA TN D-6114, 1971

9. Rogers, R.C., "Mixing of Hydrogen Injected From Multiple Injectors Normal to a Supersonic Airstream," NASA TN D-6476, 1971

10. McClinton, C.R., "The Effect of Injection Angle on the Interaction Between Sonic Secondary Jets and the Free Stream," NASA-TN D-4631, 1971.

11. Mays, R.B., Thomas, R.H., and Schetz, J.A., "Low Angle Injection Into a Supersonic Flow," AIAA Paper 89-2461, July 1989.

12. Lee, R.E., and Linevsky, M.J., "Shadowgraph Studies of Angular Injection of a Sonic Jet Into a Mach 2.8 Supersonic Flow," AIAA Paper 90-1618, June 1990.

13. Lordi, J.A. , Mates, R.E., and Moselle, J.R., "Computer Program For the Numerical Solution of Nonequilibrium Expansions of Reacting Gas Mixtures," NASA-CR-472 (1966).

14. Anderson, G., Kumar, A., and Erdos, J., "Progress in Hypersonic Combustion Technology with Computation and Experiment," AIAA Paper 90-5254, October 1990.

15. Drummond, J.P., Rogers, R.C. and Hussaini, M.Y., "A Detailed Numerical Model of a Supersonic Reacting Mixing Layer," AIAA Paper 86-1427, June 1986.

16. Carpenter, M.H., "Three-Dimensional Computations of Cross-Flow Injection and Combustion in a Supersonic Flow," AIAA Paper 89-1870, June 1989.

17. Kamath, H., "Parabolized Navier-Stokes Algorithm for Chemically Reacting Flows," AIAA Paper 89-0386, January 1989.

18. Bobskill, G.J., Bittner, R.D., Riggins, D.W., and McClinton C.R., "CFD Evaluation of Mach 17 HYPULSE Scramjet Combustor Data," AIAA Paper 91-5093, December 1991.

19. Eklund, D.R., Northam, G.B. and Fletcher, D.G., "A Validation Study of the SPARK Navier-Stokes Code for Nonreacting Scramjet Combustor Flowfields," AIAA Paper 90-2360, July 1990.

20. Mao, M., Riggins, D.W., and McClinton C.R., "Numerical Simulation of Transverse Fuel Injection" CFD Symposium on Aeropropulsion, April 1990.

21. Smith, R.E. and Weigel, B.L.; "Analytic and Approximate Boundary Fitted Coordinate Systems for Fluid Flow Simulation," AIAA Paper 80-0192, January 1980.

22. Baldwin, B.S. and Lomax, H.; "Thin Layer Approximation and Algebraic Model for Separated Turbulent Flows," AIAA Paper 78-257, January 1978.

23. Riggins, D.W., Mao, M., Bittner R.D., McClinton C.R., and Rogers, R.C., "Numerical Modeling of Normal Injection: Effect of Turbulent Schmidt Number," NASP CR-1043, April 1989.

24. Riggins, D.W., Mekkes, G.L., and McClinton C.R., "A Numerical Study of Mixing Enhancement in a Supersonic Combustor," AIAA Paper 90-0203, Jan. 1990.

25. Jachimowski, C.J., "An Analytical Study of Hydrogen Air Reaction Mechanism with Application to Scramjet Combustion," NASA TP-2791, 1988.

Table 1. Test Conditions

Stagnation Pressure	240 Atm
Stagnation Enthalpy	9.5 MJ/kg
Free Stream Velocity	3919 m/s
Free Stream Static Pressure	.065 Atm
Free Stream Temperature	1207 K
Free Stream Mach Number	5.8
Fuel Total Pressure ($\bar{q}$=1)	8.8 Atm
Fuel Total Temperature	300 K
Fuel Mach Number	1

Table 2. Seven-Reaction Model Arrhenius Rate Coefficients

No.	Reaction	A	N	E, kcal/g-mole
1	H2 + O2 <=> OH + OH	0.17E+14	0.0	48.15
2	H + O2 <=> OH + O	0.142E+15	0.0	16.4
3	OH + H2 <=> H2O + H	0.316E+08	1.8	3.03
4	O + H2 <=> OH + H	0.207E+15	0.0	13.75
5	OH + OH <=> H2O + O	0.55E+14	0.0	7.0
6	H + OH <=> H2O + M	0.221E+23	-2.0	0.0
7	H + H <=> H2 + M	0.653E+18	-1.0	0.0

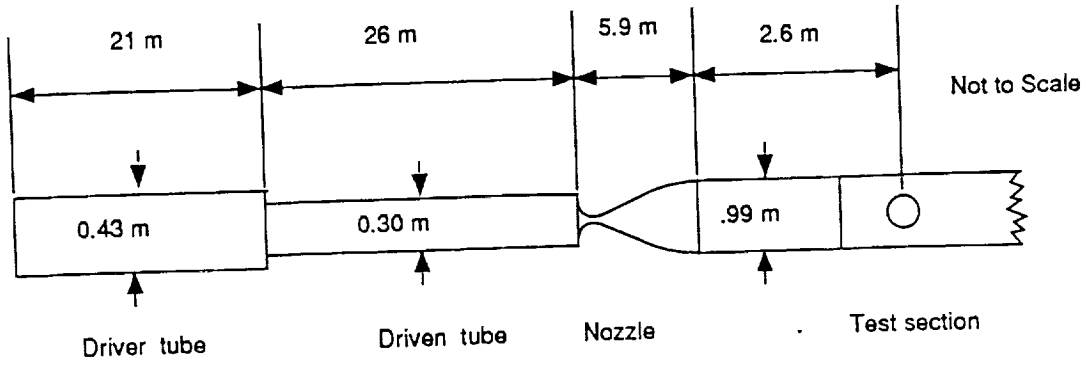

Figure 1. Ames 16-Inch Shock Tunnel

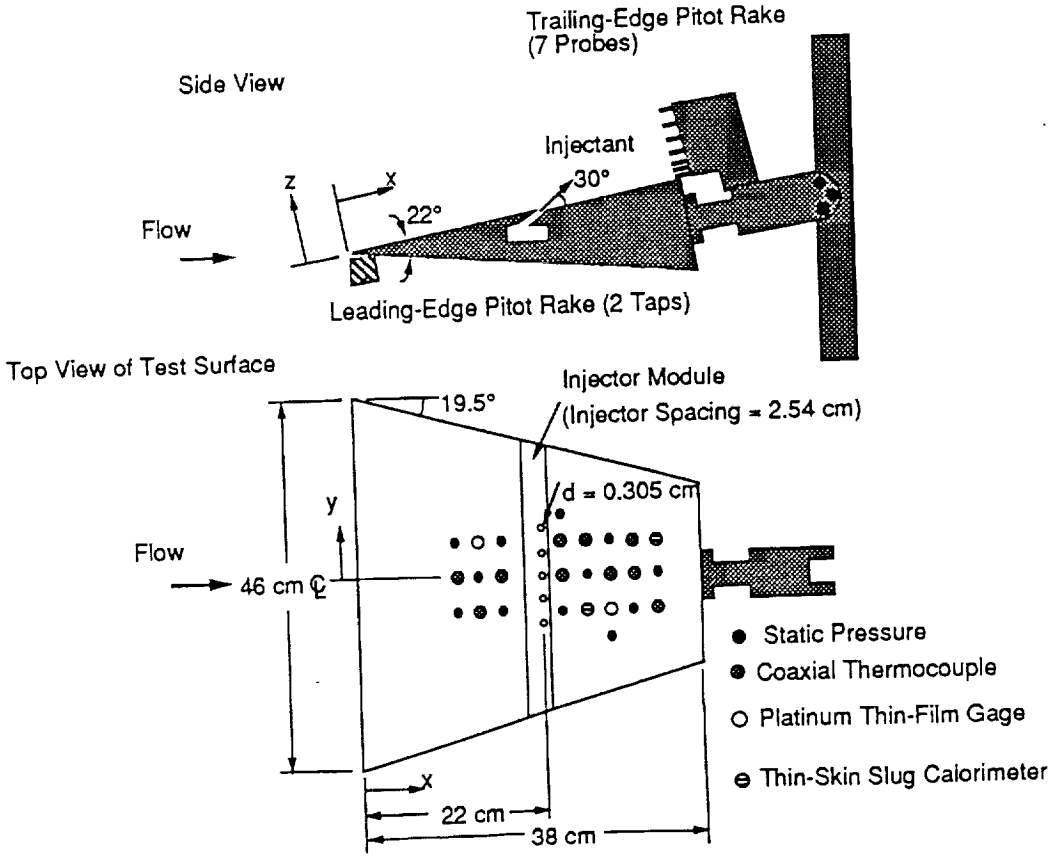

Figure 2. Test Hardware

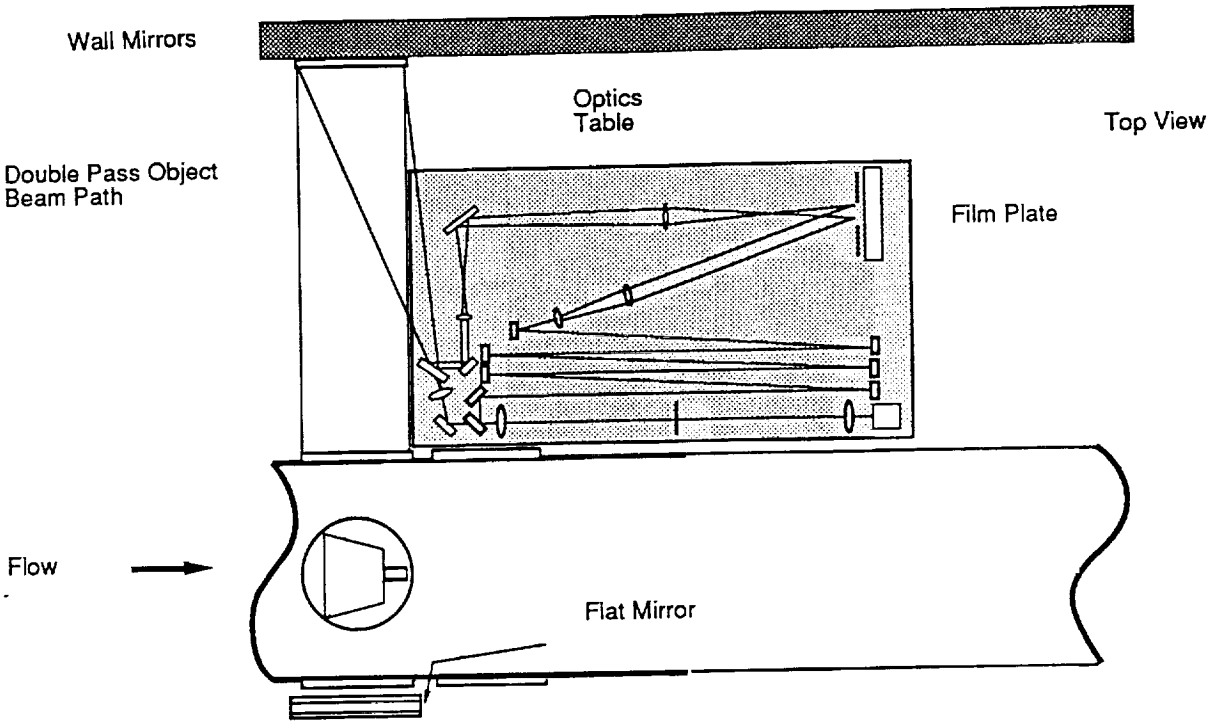

Figure 3. Holographic Interferometry Apparatus

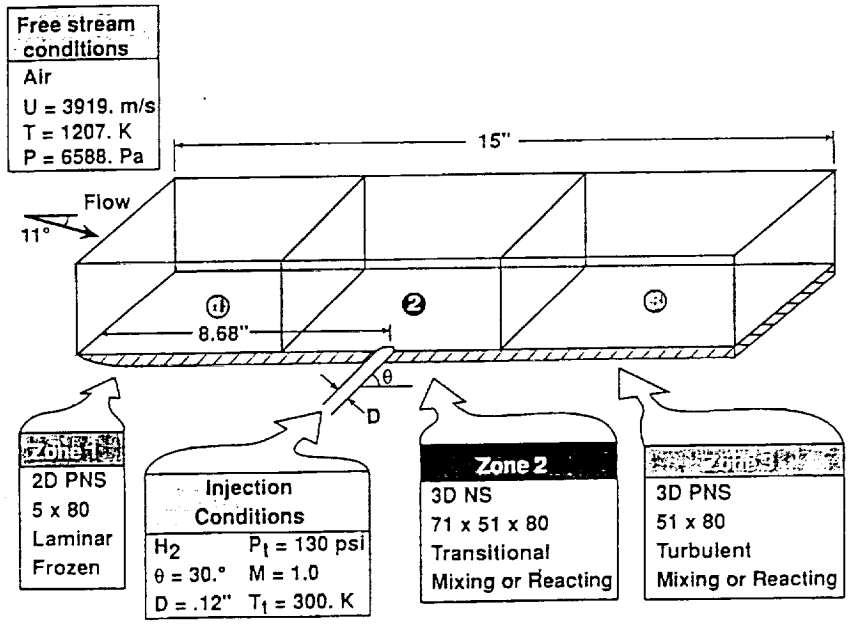

Figure 4. Computational Approach

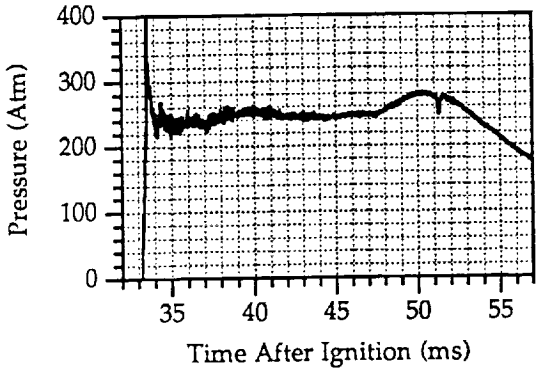

A. Reservoir Pressure

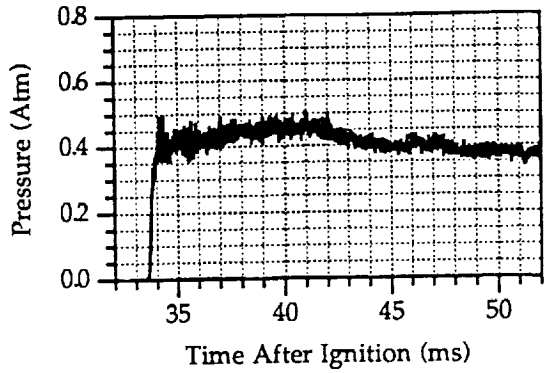

B. Nozzle Static Pressure at A/A*=45

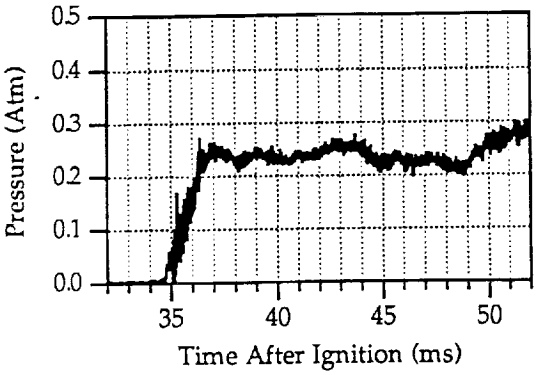

C. Model Surface Pressure

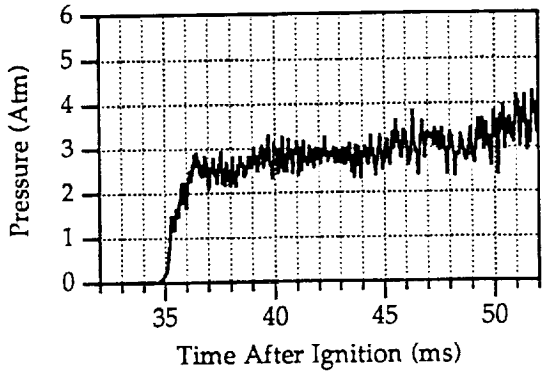

D. Pitot Pressure

Figure 5. Typical Data Traces

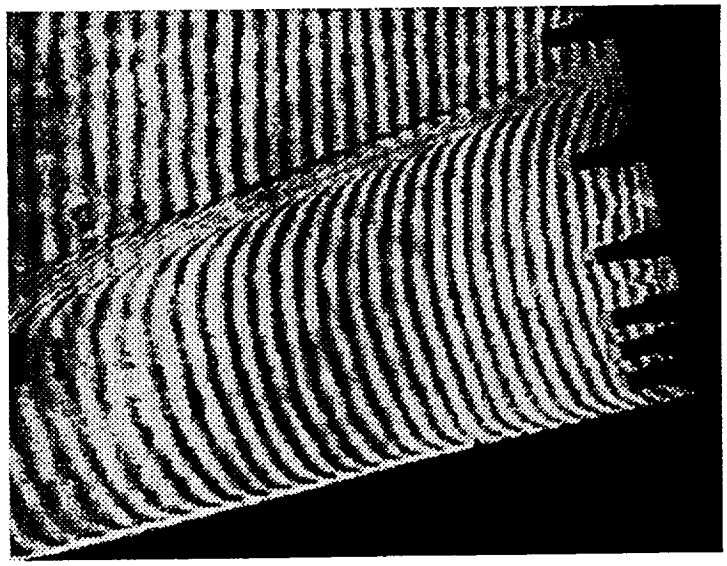

Figure 6. Interferogram for Case with No Injection

Figure 7. Interferogram for Case with Injection of Hydrogen into Air

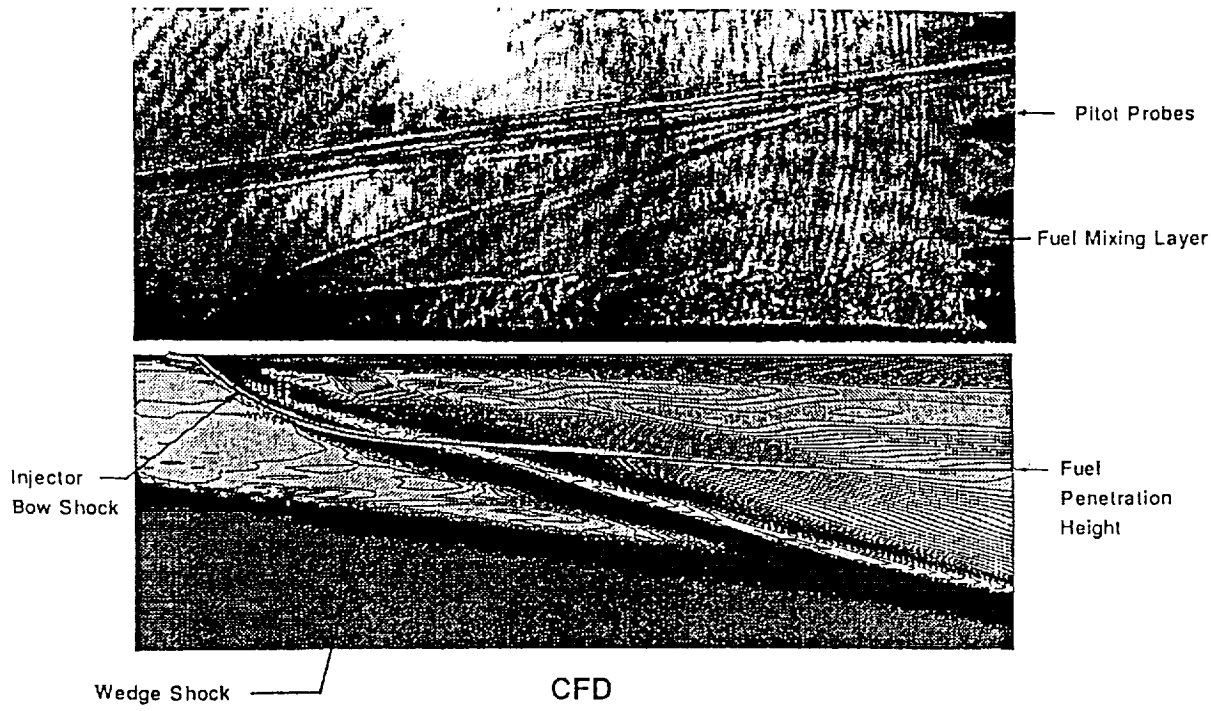

Figure 8. Shadowgraph of Case with Injection of Hydrogen into Air Compared with CFD Laterally Averaged Density Contours

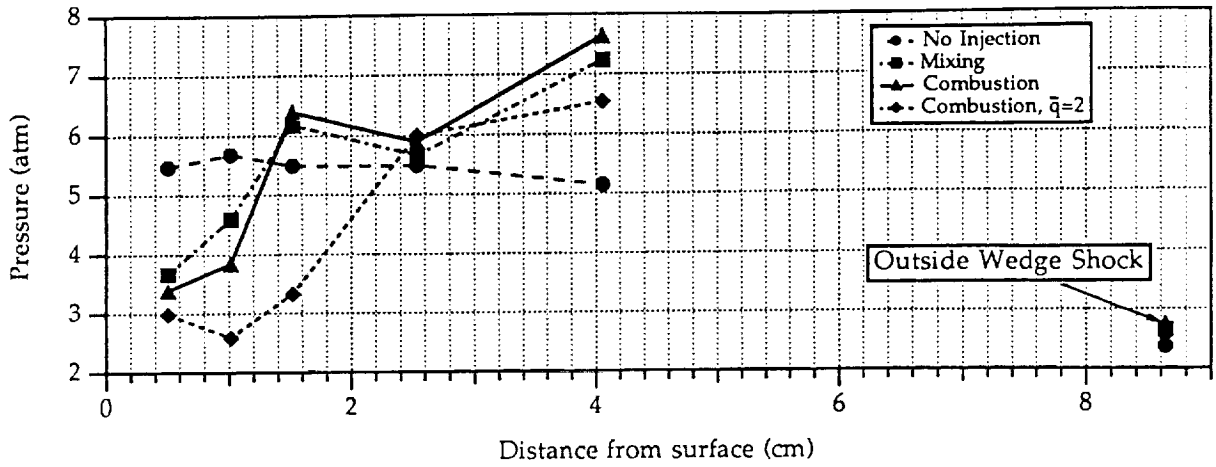

Figure 9. Pitot Pressure Results

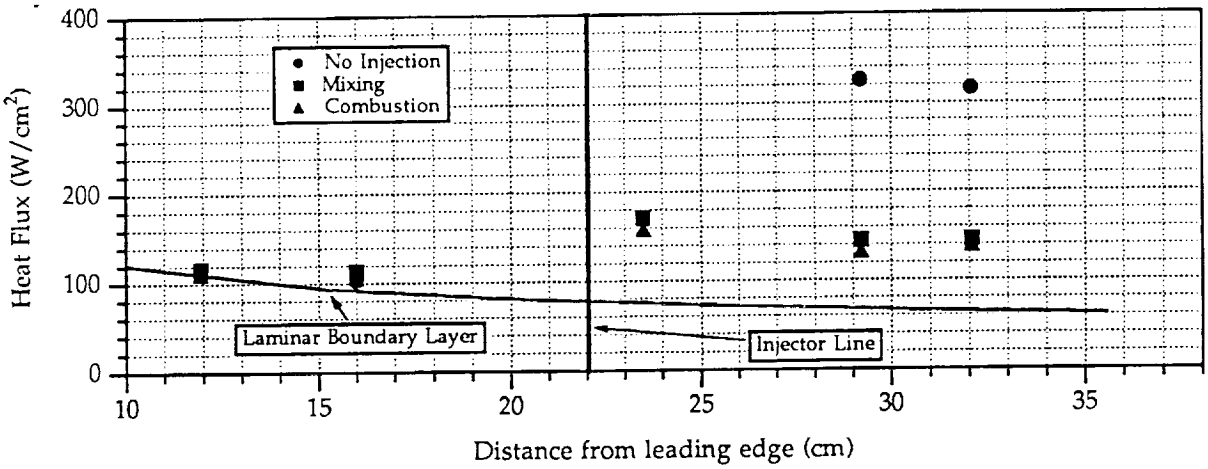

10a. Centerline

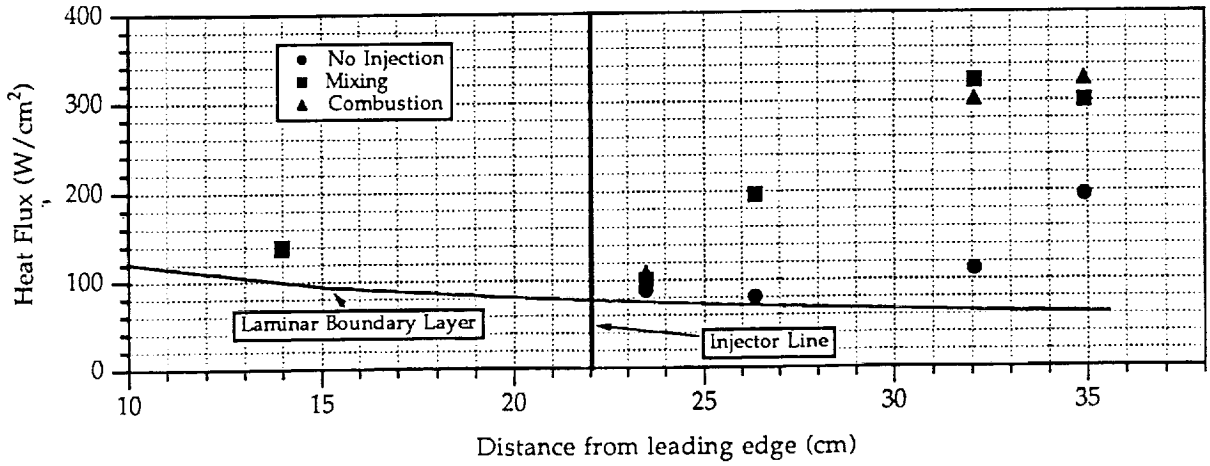

10b. Midway Between Injectors

Figure 10. Heat Flux Results

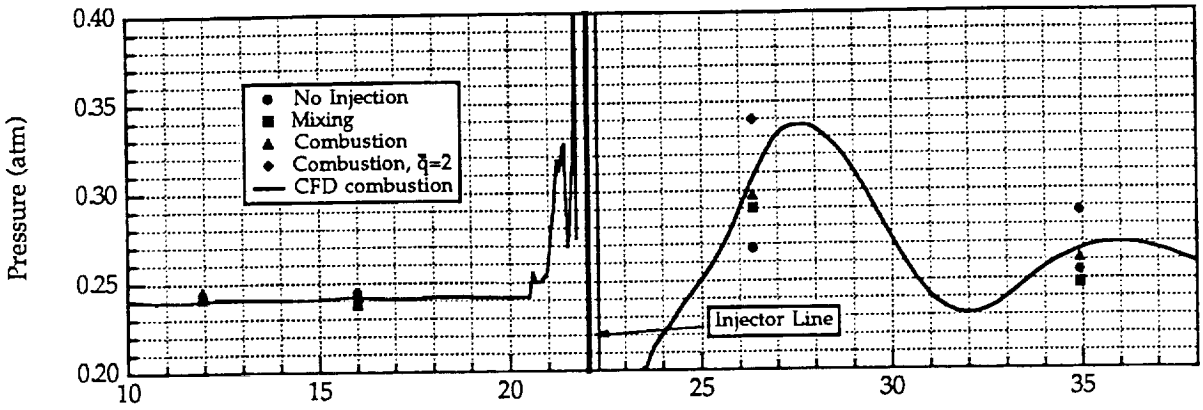

11a. Centerline

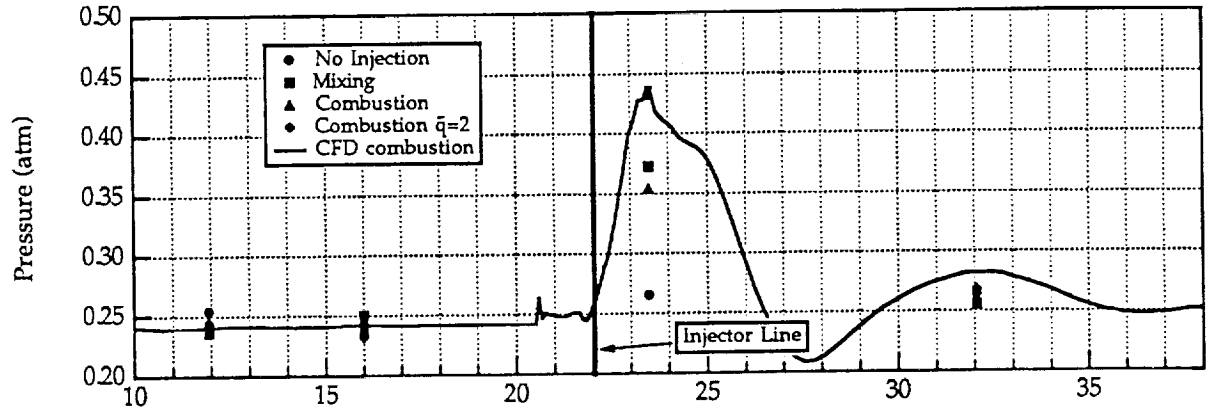

11b. Midway Between Injectors

Figure 11. Static Pressure Results

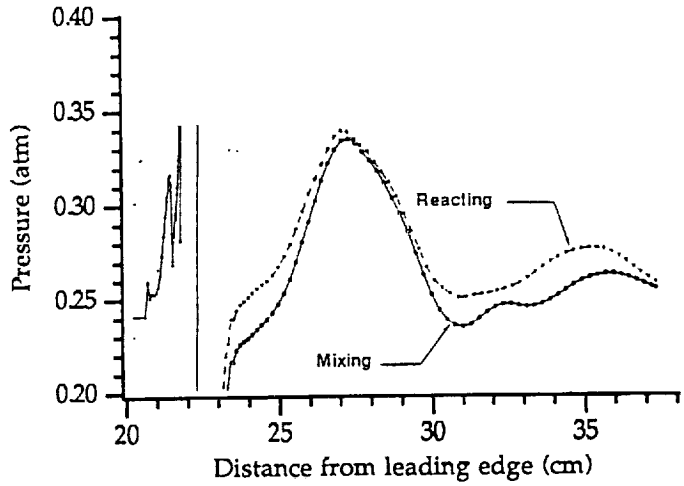

Figure 12. CFD Comparison of Centerline Static Pressure for Mixing and Combustion Runs

AIAA-92-3810

FLOW CHARACTERIZATION IN THE NASA AMES 16-INCH SHOCK TUNNEL

John A. Cavolowsky
NASA Ames Research Center, Moffett Field, CA 94035

Mark P. Loomis
MCAT Institute, San Jose, CA 95127

David W. Bogdanoff and Horacio A. Zambrana
Eloret Institute, Palo Alto, CA 94303

Mark E. Newfield and Tim C. Tam
NASA Ames Research Center, Moffett Field, CA 94035

AIAA/SAE/ASME/ASEE
28th Joint Propulsion Conference and Exhibit
July 6-8, 1992 / Nashville, TN

A92-54180
MIT

FLOW CHARACTERIZATION IN THE NASA AMES 16-INCH SHOCK TUNNEL

by

John A. Cavolowsky*
NASA Ames Research Center, Moffett Field, CA 94035
and
Mark P. Loomis*
MCAT Institute, San Jose, CA 95127
and
David W. Bogdanoff** and Horacio A. Zambrana*
Eloret Institute, Palo Alto, CA 94303
and
Mark E. Newfield* and Tim C. Tam*
NASA Ames Research Center, Moffett Field, CA 94035

ABSTRACT

Flow characteristics of the 16-Inch Shock Tunnel at NASA Ames Research Center have been determined for purposes of providing hypersonic propulsion simulation capability. The key tunnel operating parameters are the incident shock speed and reservoir pressure and enthalpy. Flow characteristics of concern are the nozzle exit pressure, temperature, Mach number, Reynolds number, chemical composition, and flow uniformity. Surface mounted gages (for pressure and heat transfer) and nonintrusive optical flow diagnostics (emission and absorption spectroscopy and holographic interferometry) are used to verify tunnel conditions. Experimental measurements are used to validate computational analysis for predicting facility performance, and CFD is used to interpret the free stream optical diagnostic measurements.

INTRODUCTION

The 16-Inch Shock Tunnel at the NASA Ames Research Center has recently been identified as a viable facility for performing hypersonic propulsion research. It was designed and constructed in the early 1960's as part of a counter flow free-flight facility for purposes of simulating flight conditions for study of reentry aerothermodynamics. The facility was reactivated and upgraded under the National Aerospace Plane Technology Maturation Program to provide a test bed for large scale X-30 flowpath testing at Mach numbers in excess of 12. This requires high dynamic pressure, high enthalpy flow corresponding directly to an airbreathing ascent vehicle trajectory. All Mach number simulation capabilities presently developed in the 16-Inch Shock Tunnel are with specific regard to an airbreathing ascent vehicle with a constant dynamic pressure of 1,000 psf.

The operational characteristics of the shock tunnel are primarily determined by wall surface measurements of pressure and heat transfer. In the shock tube portion of the facility, the critical operational parameters are the incident shock speed, reservoir pressure, and enthalpy. These parameters are either measured directly by surface gages or computed using shock tube codes. Accurate determination is essential to ascertain flow characteristics, since reservoir

* Research Scientist, Member AIAA
** Research Scientist, Associate Fellow AIAA

parameters serve as the initial conditions for computations. At the nozzle exit, flow characteristics of concern are pressure, temperature, Mach number, chemical composition, and flow uniformity. Wall surface mounted gages for pressure and heat transfer and optical diagnostics (emission and absorption spectroscopy and interferometry) are used to verify these tunnel operation conditions. Experimental measurements are used to validate computational codes for predicting facility performance. Conversely, instrumentation is not readily available for measuring all flow parameter profiles, so computational fluid dynamics must be used to compute the free stream properties. Similarly, CFD is used to interpret the optical diagnostic measurements and calibrate some in situ probes.

This paper will document the current capability of the 16-Inch Shock Tunnel by: confirming surface and flow field measurements with CFD computations; extending the understanding of the physics of facility operations by using computational models which allow the determination of system parameters not presently measurable; and performing data interpretation of flow field optical diagnostic results. Formal calibration of the shock tunnel flow properties with due regard to data precision and accuracy resulting from a thorough error analysis has not yet been completed.

HYPERSONIC PROPULSION SIMULATION REQUIREMENTS AND CAPABILITY

The use of continuous flow facilities for high speed propulsion testing is currently limited to flight Mach numbers of 12 or less. Simulation at higher Mach numbers requires the use of a pulse facility[1,2], since it is only in these facilities that the high pressures, high enthalpies and relatively uncontaminated flow can be produced. A major concern in using pulse facilities for propulsion testing is the validity of the combustion data recorded during the relatively short test time. The test time in such facilities is on the order of milliseconds. Facilities of this type currently available are reflected shock tunnels and expansion tubes. At the higher Mach numbers, expansion tubes[3,4] may have an advantage over reflected shock tunnels in that that they may not stagnate the test gas, thus avoiding the production of a dissociated test flow. However, shock tunnels tend to produce longer run times, and currently operate at higher pressures. There are several types of shock tunnels, differing mainly in the method of operation of the driver tube. These types are the resistance heated driver[5], the combustion heated driver[6-8], and the free piston driver[9].

Proper flight simulation requires that the facility provide a combustor inlet flow with the suitable pressure, temperature, Mach number, Reynolds number, and test gas composition. Also of concern is that the test time be long enough for flow to become fully established[10], which is on the order of the time required for several model lengths of test gas to pass through the combustor. Due to its method of operation and unparalleled large scale, the Ames 16 Inch Shock Tunnel has a unique capability for providing proper inlet conditions for high enthalpy (Mach 12-16) combustor testing using large scale test components combined with relatively long run time.

FACILITY OVERVIEW AND OPERATIONAL PROCEDURE

A schematic of the 16-Inch Shock Tunnel is shown in Fig. 1. Details of the driver tube configuration and operation can be found in Ref. 8. The driver section consists of a tube 70 ft (21 m) long with an inside diameter of 17 in (43 cm). The driven section is 85 ft (26 m) long with an inside diameter of 12 in (30 cm). The shock tunnel received its name for the 16-inch naval cannons used to construct its driver section. The shock tunnel is rated at 10,000 psia maximum driver pressure. The primary diaphragm is a flat, 304 stainless steel plate, pre-scored to a depth of approximately 15% of its thickness. The diaphragm thickness is 1/16 in per 1,000 psia of driver pressure. The facility operates as a reflected shock tunnel with a thin sheet of Mylar separating the driven tube from the nozzle and test section. The driver tube is instrumented with pressure transducers at three axial locations evenly distributed along the length of the tube. The driven tube is instrumented with pressure transducers and shock detectors at five axial locations.

The contoured Mach 7 facility nozzle is 19 ft (5.8 m) long and has an exit diameter of 39 in

(0.99 m). Interchangeable throat sections are used to vary the nozzle area ratio. Recent results have been obtained for area ratios of 190, and a minimum of 95 is attainable without sacrificing test time or ideal shock tube end wall behavior. The nozzle contains ports at six axial locations for surface mounted instrumentation and optical access. The test cabin is a 72 in long by 54 in square cross section box located immediately downstream of the nozzle exit. It is designed with large doors on four sides providing easy personnel and optical access to test articles. Nozzle exit conditions are measured in this test cabin using a 35 probe pitot rake. Probes are located at one inch intervals and provide measurement of impact and static pressure and stagnation point heat flux.

Operating conditions are achieved by combustion heating helium with a nearly stoichiometric mixture of hydrogen and oxygen. The gases are loaded into the driver tube through a 2 in inside diameter manifold which rests along the bottom of, and spans the entire length of, the driver tube. The manifold has small (0.020 in diameter) orifices evenly spaced along its length and is designed to promote uniform gas mixing. The loading procedure introduces the hydrogen first followed by the premixed combination of helium and oxygen. This combustible charge is ignited by four tungsten wires strung down the center of the driver and heated to approximately 2,000 K by the discharge from a high voltage capacitor bank (C=150 μF and V=14 KV). Combustion is complete approximately 25 ms after ignition, and the flat, prescored diaphragm breaks at the predetermined pressure.

The shock speed, which determines the reservoir enthalpy and hence the flight equivalent Mach number, is varied by adjusting the ratio of the driver tube post-combustion pressure to the driven tube pre-test fill pressure. Thus, for the Mach 12, 14, and 16 conditions, the driver tube initial parameters remain identical. Driver tube operation has been recently demonstrated at pressures of 8,000 psia; however, efforts are being made to increase the operational pressure to the maximum rating of 10,000 psia.

RESERVOIR CONDITIONS

Reservoir conditions are those behind the reflected shock at the end of the driven tube. These conditions can be computed using standard shock tube relations. Variables in these relations are incident shock speed, initial fill pressure, measured reservoir pressure, and test gas composition. Equilibrium calculations are used to determine the conditions across the incident and reflected shocks. For a range of shock speeds, the shock tube can be operated in either the tailored interface mode or the non-tailored interface mode. For tailored interface operation, the reflected shock passes through the contact discontinuity without reflection. The reservoir conditions are those behind this single reflected shock. This is seen in reservoir pressure traces as a rapid rise to a constant pressure plateau. For non-tailored operation, shock or expansion waves successively reflect off the contact discontinuity and driven tube end wall causing a variation in the reservoir properties. These waves will decay quickly, usually after one or two reflections. This condition is marked by a more gradual settling to the constant pressure plateau. This method of operation, also referred to as the equilibrium interface[11] method, defines the beginning of the test time as that time after which reservoir properties cease to change significantly. For the equilibrium interface method of operation, if the calculated pressure behind the reflected shock is not equal to the measured pressure, an isentropic expansion to the measured pressure is performed to establish the equilibrium reservoir conditions. The test time is complete when the contact discontinuity reaches the reservoir and driver gases begin to enter the nozzle. Determination of this time period will be discussed in greater detail later in the paper.

A graphical representation of this equilibrium interface generation process is shown in Fig. 2a (Ref. 21). The computed density contours are plotted on an X-T diagram along the full length of the shock tube. The computation begins with a simulation of the pressure distribution in the driver tube prior to diaphragm rupture and includes time dependent behavior, geometry variations, an approximation of viscous losses, and full chemical kinetics. The test gas region is shown at the far right of the diagram and in the expanded region of the plot. Evident is the incident shock generated upon primary diaphragm rupture and the several successive shock reflections establishing the pressure rise and the equilibrium interface condition. Figure 2b shows a comparison of experimental and computational driver gas pressure. The

computation which includes a sinusoidal pressure gradient in the driver tube agrees well with the measured pressure. Examining the results of this same computation for pressure at the driven tube reservoir also shows reasonable agreement with experiment (see Fig. 2c). This simulation capability allows for detailed examination of tunnel operating behaviors not previously available. Future expansion of the shock tunnel operational envelope will make use of these computations to optimize performance.

Facility operation has been demonstrated at shock speeds ranging from 2.6-3.5 km/s. Figures 3 and 4 show that these conditions match total enthalpies corresponding to Mach 12 to 16 for the X-30 flight trajectory. Experimentally it is found that, using nitrogen as the test gas, tailored interface operation is approximately achieved for a shock speed near 3 km/s (Mach 14 enthalpy). However, preliminary data indicates that using air as the test gas, tailoring is not achieved for shock speeds over our demonstrated operating range. It is found that for these conditions the equilibrium interface is established about 2 ms after arrival of the incident shock. Reservoir pressures are nearly constant from this point until the arrival of the expansion wave, approximately 17 ms after incident shock arrival for present conditions.

NOZZLE EXIT CONDITIONS

The facility nozzle exit conditions were computed using the nonequilibrium nozzle code NENZF[12]. This is a standard inviscid nonequilibrium 1-D engineering code which has been updated with NASP standard chemical kinetic rate coefficients. Inputs to the code are reservoir conditions and nozzle contour. An effective nozzle area ratio of 170 is used in the sample calculations instead of the actual area ratio to account for viscous displacement effects. This was determined from experimental measurements of reservoir, pitot, and static pressures. Based on recent experimental results discussed below, the code appears to be satisfactorily predicting nozzle exit conditions.

A recent experimental study of injection and mixing in hypersonic flows[13] provided an opportunity to measure free stream static pressure. The tunnel operating conditions used in this study are included in Table 1. For this test, a flat plate was installed at an 11 degree angle of attack to the flow and hydrogen was injected from the surface at an angle of 30 degrees. The model was inclined to the flow in order to increase the static pressure. For the highest tested driver operating pressure, 408 atm (6,000 psia), the resulting reservoir pressure was 347 atm (5,100 psia). At this reservoir pressure, it was seen that the static pressure as measured on the surface of the flat plate was just over 1/3 atm (5 psia). The measured pressure agreed with the pressure as predicted by NENZF to within 5%.

More detailed computations using an axisymetric viscous code with finite rate chemistry and a quasi-one-dimensional code are complete and have been reported in Ref. 14. Comparisons of results from these two codes with NENZF results are shown in Figs. 5a, b, and c. Detailed computations predict gas temperatures at nozzle exit to be almost 30% lower than those computed using NENZF, while comparisons of static pressure and axial velocity are good to within about 6%. A lower O-atom recombination rate chosen for use in the detailed computations can account for the difference in temperature. The axisymetric flow code predicts a pressure gradient of about 6% across the inviscid core. A static pressure profile to be measured later in the program will provide a valuable validation for these computations.

In order to achieve higher static pressures recommended for future combustor testing, the driver tube will be operated at pressures of at least 544 atm (8,000 psia). Table 2 contains computed nozzle exit conditions for future tests to be run at Mach 12, 14, and 16 equivalent enthalpy at the 544 atm reservoir pressure condition.

Another important nozzle exit parameter is the extent of the inviscid core flow. A previous calibration of the facility[6] measured the core flow at a position well downstream of the nozzle exit to be roughly 50% of the tunnel diameter. Correlations for boundary layer development indicate that for the new test cabin the core flow should be 70% of the diameter at the nozzle exit. Recent measurements with the instrumented pitot rake in the test cabin show a core flow of approximately 70% of the nozzle exit as predicted from earlier measurements (see Fig. 6). Uniformity of the inviscid core flow is also important. The pitot pressure profile shows a standard deviation in impact pressure of less

than 5%. As further evidence of uniformity, Fig. 7 shows a shadowgraph of flow over individual pitot heads on the facility rake for a Mach 16, 6000 psia driver pressure test condition. The shock structure on the pitot heads is clear, and there is no evidence of shocks from the nozzle disturbing the core flow. Plans for the calibration of the facility with the new test cabin and rake will be discussed in the conclusion.

Turbulence simulation requirements for scramjet propulsion testing are not fully understood as of the present, and modelling of turbulent flows is not yet a mature technology. It is clear, however, that a fully turbulent boundary layer must be ingested by the combustor to simulate X-30 conditions. The free stream unit Reynolds number provided at nozzle exit for the 8,000 psia driver pressure condition is determined to vary from $6x10^6$/m to $2x10^6$/m for the range of Mach numbers from 12 to 16 (see Table 2). Using a boundary layer transition criteria developed at Calspan[20] and found to be valid in their shock tunnel, the predicted transition point Reynolds number is about $1.5x10^6$. Given the large scale of the 16-Inch Shock Tunnel, a long enough inlet can be accommodated to provide ingestion of a fully turbulent boundary into the combustor.

TEST TIME CONSIDERATIONS

Though reservoir pressure may be nearly constant for a relatively long period, the composition of the gas passing through the nozzle is contaminated by driver gas much earlier. The arrival of driver gas contamination is dependent on several mechanisms including shock wave boundary layer interactions, contact discontinuity instability, and simple drainage of the test gas through the nozzle. With the current throat size, all of the test gas should drain from the reservoir in about 12 ms if there were no mixing of the driver and driven gases. This represents a 30% reduction in test time based on reservoir pressure alone. Mixing of the driver and driven gases at the contact discontinuity reduces the uncontaminated test flow even further. Several measurements have been used to determine the time of arrival of the helium (the primary constituent of the driver gas) including nozzle wall static pressure, heat transfer, free stream static pressure, and spectroscopic methods such as total radiation and laser absorption measurements[15,16]. Similar conclusions are drawn from all of these measurements: initially there is a period of 2-3 ms dedicated to nozzle start up and decay of equilibrium interface transients followed by a nearly constant property flow period of 3-5 ms. As helium infiltrates the test gas, the nozzle wall static pressure and heat flux decreases (Fig. 8a and b). This is due to the increase in value of the ratio of specific heats of helium. Figure 8c shows the free stream static pressure as measured by a special static pressure probe adapter mounted on the pitot rake. This indicates that the nozzle start-up process is expanded in time as measured in the test section far downstream of the nozzle. Since helium and the other driver gas constituents are necessarily colder than the shock heated driven gas, the value of total radiation will also decrease as the helium contamination increases (Fig. 8d). The free stream OH temperature measured with a scanning laser absorption system[16] is shown in Fig. 8e. (These temperature measurements are limited to at a few, low area ratio, nozzle locations.) For a few selected tests, the driven tube air was saturated with water. The shock heating process formed OH which was detected by the laser absorption diagnostic when expanded in the nozzle. Since detectable OH could only be present in the driven gas, the test time was assumed to be complete when the OH signal disappeared. The character and duration of the nozzle start up transient is well captured in the temperature measurements, and the constant temperture region is consistent with the test time. The unreduced OH absorption trace (not shown) illustrates the decay in driven gas OH mole fraction commensurate with the end of test time. An axisymetric, nonequilibrium nozzle expansion flow code[17] was used to compute the temperature at the first nozzle port. Fig. 8e shows the average measured temperature to agree with the computed temperature to within 1 percent.

Nozzle wall static pressure is currently used on each run as the primary measure of test time. Recent results of these nozzle wall static pressure measurements are shown in Fig. 9. An initial transient period is indicated, followed by a period of approximately constant pressure, defined as the data averaging period. The indicated drop in static pressure correlates with the arrival of driver gas contamination confirmed by other methods of measurement, and is here used to indicate the end of the data averaging

period. Following this decrease in static pressure there is a period of nearly constant pressure, which is interpreted as flow of entirely driver gas. Therefore, three distinct test time periods can be defined: 1) a period of about 17 ms over which the reservoir pressure is nearly constant, 2) a period of uncontaminated test gas flow which includes the 2-3 ms for nozzle start up and the time to reach equilibrium interface, and 3) an averaging period of 3-5 ms in which the flow properties are essentially constant.

Figure 10 plots test time as per definitions 2) and 3) for different flight Mach numbers, and Fig. 11 plots test gas slug length. Slug length is defined by the expression, tU/L, where t is the facility test time, U is the flow velocity, and L is the characteristic length of the test article. These figures emphasize an important characteristic of the 16-Inch Shock Tunnel, namely its large temporal scale. When performing propulsion testing in pulse facilities, it is generally considered necessary that three gas exchanges through the combustor take place to assure flow establishment and hence proper assessment of mixing and combustion efficiency[10]. For facilities where test time is modest, the combustor model must be of a small scale to accommodate this criterion. For the Ames 16-Inch Shock Tunnel, however, with its long test times and commensurately long slug lengths (in excess of 10 m), virtually full scale X-30 combustor modules can be tested with confidence that the flow establishment criteria is sufficiently satisfied.

CHEMICAL STATE OF TEST GAS

As indicated in Tables 1 and 2, the reservoir gas temperature is between 4,600 and 7,000 K. These high temperatures are characteristic of all reflected shock tunnels, and indicate a highly dissociated reservoir gas. The nozzle expansion process is nonisentropic and the test gas becomes chemically frozen[18]. The result is a test gas which contains NO and dissociated oxygen. These species are known to affect combustion due to their influence on the ignition delay process and heat release[19]. For current operating conditions in Tables 1 and 2, the amount of NO in the test gas is about 5%. This is, however, not necessarily considered important in the scramjet combustion environment, since the reduction in ignition delay caused by NO will not significantly effect the mixing limited combustion process controlling propulsion at Mach number greater than 14. The dissociated oxygen entering a combustor, however, will produce a higher pressure rise due to combustion, since the recombination of atomic oxygen creates a mixture with an effective higher heating value. The amount of free stream oxygen depends, in general, on pressure, nozzle expansion rate, and nozzle length. Higher pressure promotes more collisions and hence higher recombination rates reducing O-atom mole fraction. More rapid expansion in the nozzle reduces collisions and allows higher mole fractions of O-atoms prior to the chemical freezing point. Longer nozzles produce less dissociated oxygen due to the longer residence time in the nozzle available for recombination collisions. The scale of the 16-Inch Shock Tunnel allows for a long nozzle (5.8 m) and a small area ratio (typically 170 for results presented here and as low as 95), resulting in relatively low mole fractions of NO and dissociated oxygen. Assumed is a constant reservoir pressure of 375 atm and values of A/A^* as shown specific to each Mach number. A plot of the variation of both NO and O-atom mole fraction versus Mach number and reservoir temperature is shown in Fig. 12. Although the NO mole fraction remains virtually constant for the considered range of Mach numbers at a level of about 5%, dissociated oxygen varies by more than an order of magnitude, from over 5% near Mach 16 to less than 0.2% at Mach 12.

CONCLUSIONS AND FUTURE PLANS

The NASA Ames 16-Inch Shock Tunnel has been successfully reactivated and its nozzle exit flow parameters characterized for purposes of hypersonic propulsion testing in the Mach number range of 12 to 16. An extensive experimental and computational effort have served to verify its applicability for X-30 flowpath testing as defined by the NASP program office. Nozzle exit static pressures are sufficiently high to provide combustor inlet plane pressures in excess of 0.5 atm (i.e. pressure achieved after the flow is processed by a cowl shock). The measured test time (3 to 5 ms) and test gas slug length (more than 10 m) coupled with its large nozzle diameter and core flow fraction allow proper flow establishment in full

scale combustor modules. Free stream Reynolds numbers and dissociated oxygen and NO mole fractions have been identified. Computational tools for shock tube analysis and nozzle exit flow quality have been developed and are serving to allow enhanced understanding of facility operation.

An extensive calibration of the facility with its new test cabin will soon be completed. This calibration will include three different sets of conditions: Mach 12, 14, and 16 flows using air as test the gas. The primary purpose of this calibration process is to provide a matrix of documented conditions for X-30 combustor flowpath testing. The predicted conditions are given in Table 2. Throat sizes (hence, the nozzle area ratio) will, in general, be different for each condition.

The primary goal of this calibration period will be to obtain experimental measurements including impact pressure, static pressure, and stagnation heat transfer at the nozzle exit rake. These results will be correlated with tunnel operating conditions computed using the measured quantities of shock speed and reservoir pressure to verify total enthalpy and, therefore, flight equivalent Mach number. Impact pressure measurements will be used to determine the extent of the inviscid core flow and the uniformity of the gas passing through the combustor. The static pressure probe data will be used primarily for determining test gas mass flow correlations, since this parameter is more sensitive than impact pressure to changes in reservoir conditions and in effective area ratio. The static pressure is also a sensitive indicator of test time. Included in this primary goal is the requirement of validating the computational fluid dynamics models that are being used to predict nozzle exit flows. Validation of these codes is essential to the future use of the facility given that all free stream parameters of interest cannot be measured experimentally. In fact, the static pressure probes used on the pitot rake require a computational calibration to provide for their quantitative use. This computational calibration effort is currently underway.

All of these data will be critical for determining combustor inlet mass capture, a parameter essential for proper use of this facility as a propulsion test bed. The combustor planned for the first entry in the shock tunnel will be instrumented with inlet and cowl leading edge pressure transducers to assess the free stream flow parameters; however, CFD analysis will be required to mate the measured tunnel operating parameters with combustor inlet geometries and provide a more precise value of combustor inlet mass capture.

It is important to note that although the present facility flow characterization and calibration effort is directed toward propulsion testing and research studies, the 16-Inch Shock Tunnel is not restricted to this use. Its will be valuable to experimental and computational research involving real-gas blunt body aerothermodynamics. This includes flight trajectories for spacecraft that will be studied as part of the Mars mission program and NASA's efforts to return to the lunar surface. Future plans will include calibration of test conditions required for these and other flight programs.

ACKNOWLEDGEMENTS

Operation of any facility of this scale requires the concerted efforts of a large team of dedicated personnel. The authors appreciate the work of the Thermophysics Facility Branch in preparing the facility and performing the tests and especially thank Robert Miller, Charles Cornelison, Warren Norman, Donald Holt, Daniel Theroux, Donald Bowling, and Tom Kowalski. The authors also thank Jean-Luc Cambier, Dinesh Prabhu, Susan Tokarcik, Gregory Wilson, and Seung-Ho Lee of the Computational Aerothermodynamics Section for their tremendous computational support and analysis of shock tunnel performance.

REFERENCES

1. Dunn, M.G., Lordi, J.A., Wittliff, C.E., and Holden, M.S., "Facility Requirements For Hypersonic Propulsion System Testing," AIAA Paper 89-0184.

2. Neuman, R.D., "Requirements in the 1990's for High Enthalpy Ground Test Facilities for CFD Validation," AIAA Paper 90-1401.

3. Orth, R. C. and Erdos, J. I., "Use of Pulsed Facilities for Testing Scramjet Combustors in Simulated Hypersonic Flight Conditions," Proc. 9th Intl. Symp. on Air Breathing Engines, Sept. 1989, Athens, Greece.

4. Tamagno, J., Bakos, R., Pulsonetti, M., and Erdos, J., "Hypervelocity Real Gas Capabilities of GASL's Expansion Tube (HYPULSE) Facility," AIAA Paper 90-1390.

5. Dunn, M.G., Moller, J.C., and Steele,R.C., "Development of a New High Enthalpy Shock Tunnel," AIAA Paper 88-2782.

6. Bogdanoff, D. W., Deiwert, G. S., Strawa, A. K., and Cavolowsky, J. A., "Ames Shock Tunnel Facility Calibration and Initial Test Results (U)," presented at the Seventh National Aerospace Plane Technology Symposium, October 23-27, 1989, Cleveland, OH.

7. Cavolowsky, J. A., Hanson, R. K., and Bogdanoff, D. W., "Test and Diagnostic Capability for High Mach Number Propulsion Testing in the Ames Pulse Facility (U)," Tenth National Aerospace Plane Technology Symposium, April 23-25, 1991, Monterey, CA.

8. Bogdanoff, D. W., Zambrana, H. A., Cavolowsky, J. A., Newfield, M. E., Cornelison, C. J., and Miller, R. J., "Reactivation and Upgrade of the NASA Ames 16-Inch Shock Tunnel, Status Report," AIAA Paper 92-0327.

9. Stalker, R.J. and Hornung, H.G., "Two Developments with Free Piston Drivers," Proc. Seventh International Shock Tube Symposium, 1970.

10. Anderson, G., Kumar, A., and Erdos, J., "Progress in Hypersonic Combustion Technology with Computation and Experiment," AIAA Paper 90-5254.

11. Copper, J.A., "Experimental Investigation of the Equilibrium Interface Technique," Physics of Fluids, Vol. 5, No. 7, 1962.

12. Lordi, J.A. , Mates, R.E., and Moselle, J.R., "Computer Program For the Numerical Solution of Nonequilibrium Expansions of Reacting Gas Mixtures," NASA-CR-472 (1966).

13. Loomis, M. P., Zambrana, H. A., Bogdanoff, D. W., Tam, T. C., Cavolowsky, J. A., Newfield, M. E., and Bittner, R. D., "30 Degree Injectors at Hypervelocity Conditions," AIAA Paper 92-3288.

14. Cambier, J.-L., Tokarcik, S., and Prabhu, D., "Numerical Simulation of Unsteady Flow in a Hypersonic Shock Tunnel Facility," AIAA Paper 92-4029.

15. Cavolowsky, J. A., Chang, A. Y., DiRosa, M. D., Hanson, R. K., and Strawa, A. W., "Laser Absorption Measurement of OH in Shock Tunnel Flows (U)," presented at the Seventh National Aerospace Plane Technology Symposium, October 23-27, 1989, Cleveland, OH.

16. Cavolowsky, J. A., Newfield, M. E., and Loomis, M. P., "Laser Absorption Measurements of OH Concentration and Temperature in Pulsed Facilities," AIAA Paper 92-0142.

17. Lee, S.-H., Bogdanoff, D. W., Cavolowsky, J. A., and Park, C., "Nonequilibrium H_2-Air Reactions in Shock Tunnel Nozzle," AIAA Paper 90-1751.

18. Lordi, J.A., Boyer, D.W., and Dunn, M.G., "Description of Nonequilibrium Effects on Simulation of Flows About Hypersonic Vehicles," AIAA Paper 88-0476.

19. Rogers, R.C., "Effects of Test Facility Contamination on Supersonic Hydrogen-Air Diffusion Flames," 23rd JANNAF Combustion Meeting, Oct. 1986.

20. Grace, J. M., et al., "Hypersonic Shock Tunnel: Description and Capabilities," Arvin/Calspan Corporation Report, January 1987, Buffalo, New York.

21. Wilson, G. J., "Quasi 1-D Time Dependent Simulations of High Enthalpy Pulsed Facilities," to be presented at the 4th AIAA International Aerospace Planes Conference, December 1-4, 1992, Orlando, FL.

Flight Mach Number	Mach 14	Mach 16
Reservoir Conditions		
Pressure, Atm	245	347
Enthalpy, MJ/kg	9.6	12.2
Temperature, K	5750	6850
Nozzle Exit Conditions		
Pressure, Atm	0.074	0.12
Temperature, K	1280	1720
Mach Number	5.7	5.6
Re/m, 10**6	1.5	1.7
Model Surface Conditions		
Pressure, Atm	0.27	0.35
Temperature, K	1865	2400
Mach Number	4.5	4.4
Re/m, 10**6	3.0	3.4

Table 1. Hypersonic Mixing and Injection Test conditions.

Flight Mach Number	Mach 12	Mach 14	Mach 16
Reservoir Conditions			
Pressure, Atm	517	490	463
Enthalpy, MJ/kg	6.6	9.2	12.2
Temperature, K	4650	5730	6930
Nozzle Exit Conditions			
Pressure, Atm	0.16	0.15	0.13
Temperature, K	832	1235	1676
Density, kg/m**3	0.067	0.042	0.027
Velocity, m/s	3345	3868	4366
Mach Number	5.9	5.7	5.6
Re/m, 10**6	6.0	3.4	2.1

Table 2. Conditions for 544 atm (8,000 psia) driver pressure operation.

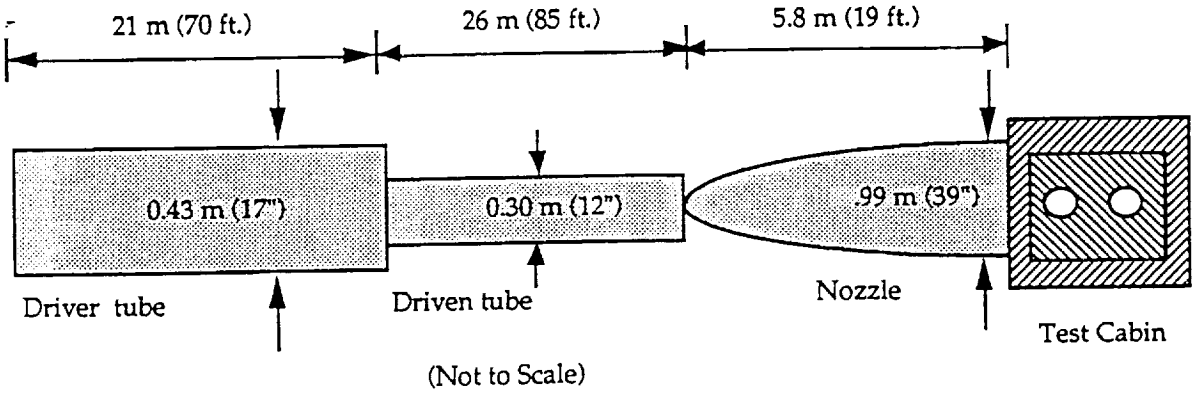

Figure 1. Ames 16-Inch Shock Tunnel

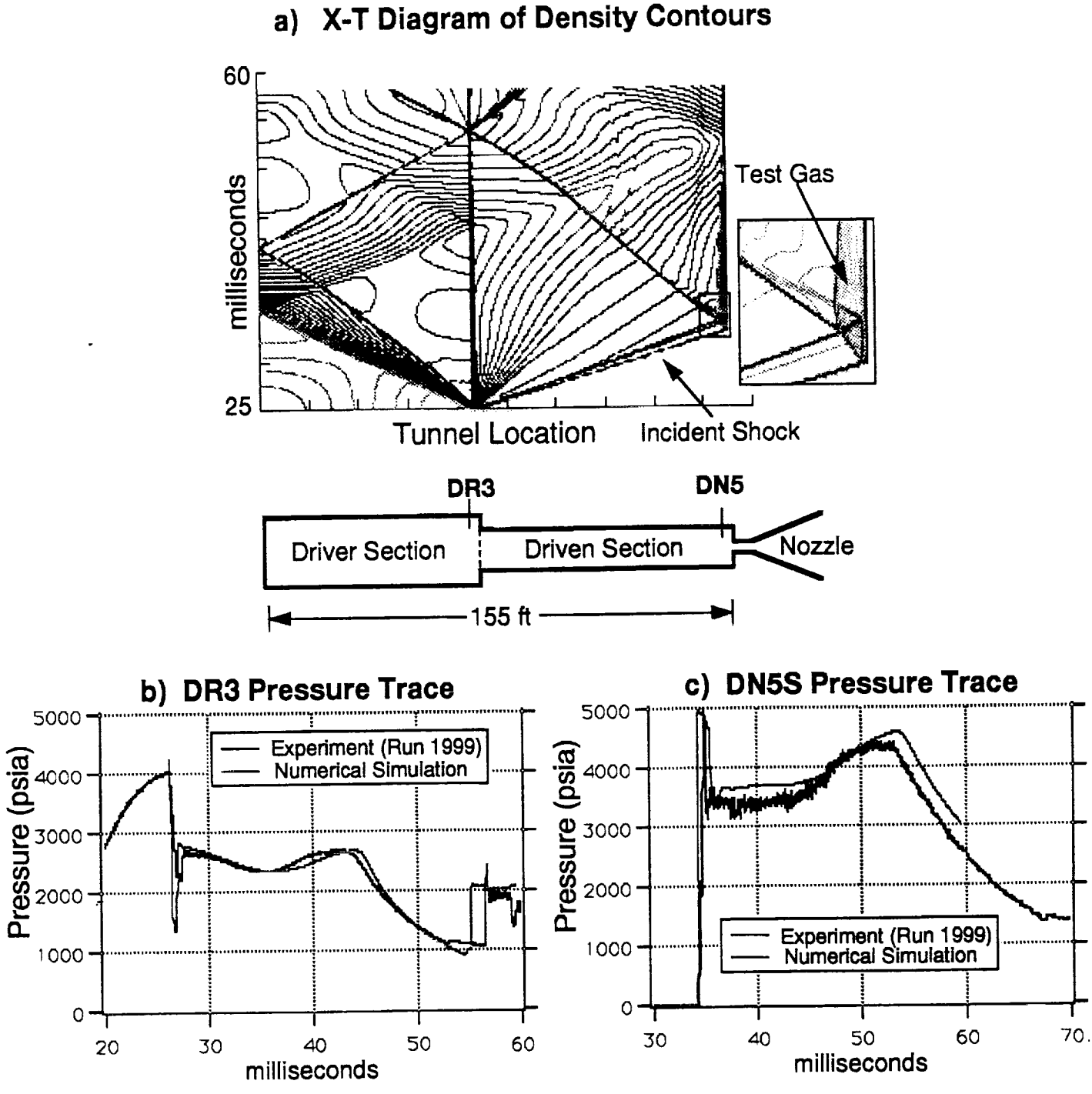

Fig. 2. Ames 16-Inch Shock Tunnel: Comparison of simulation with experimental measurements

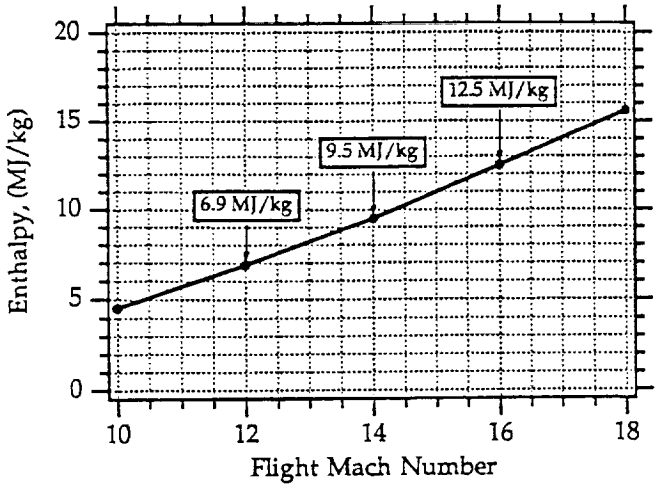

Figure 3. Total Enthalpy vs. Simulated Flight Mach Number

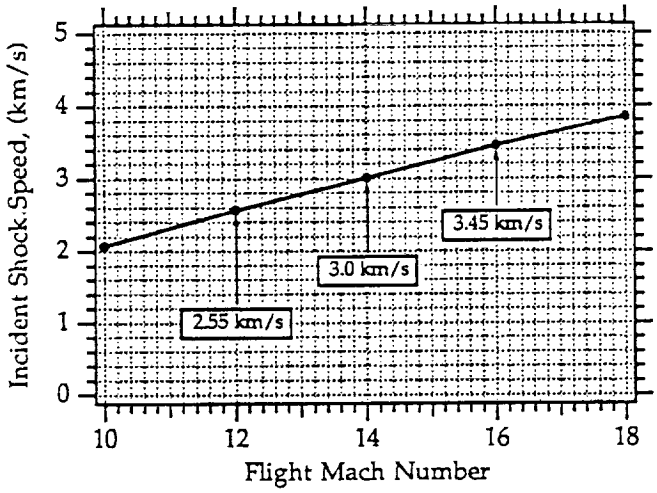

Figure 4. Incident Shock Speed vs. Simulated Flight Mach Number

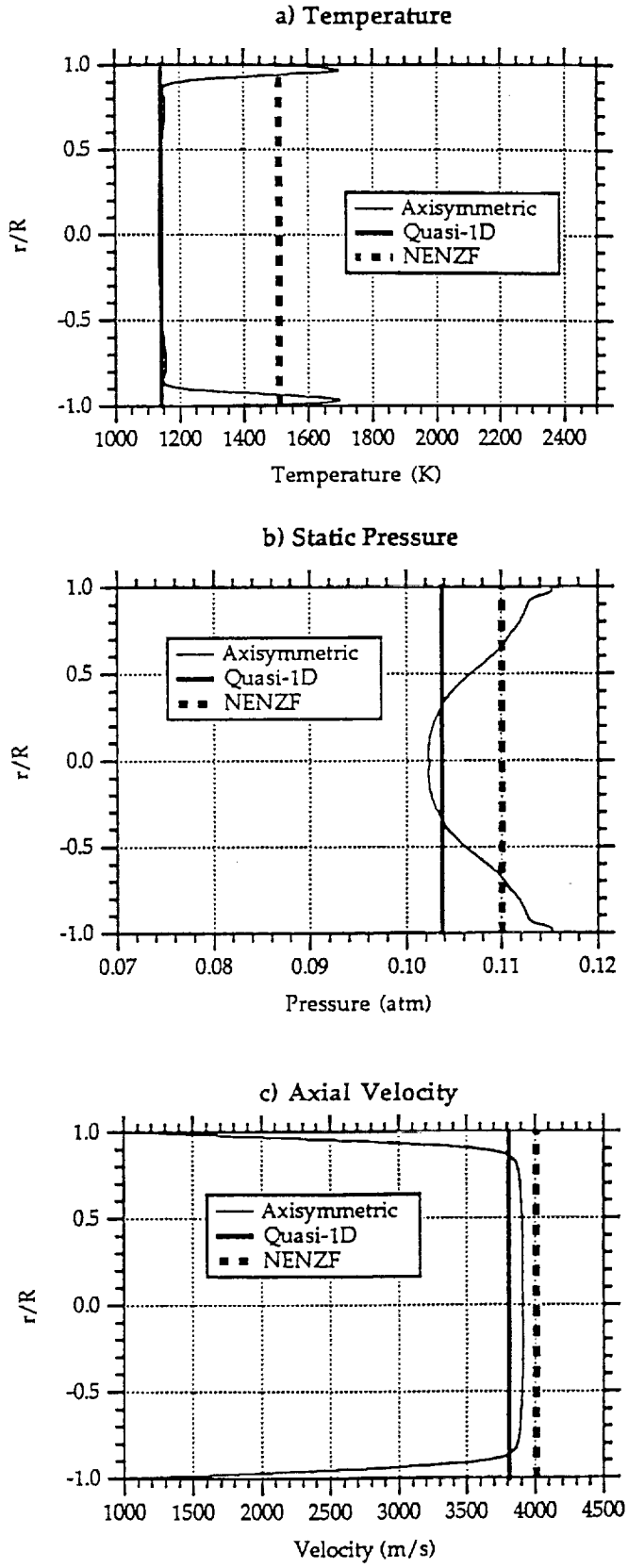

Fig. 5. Nozzle flow code comparisons: Nozzle exit profiles

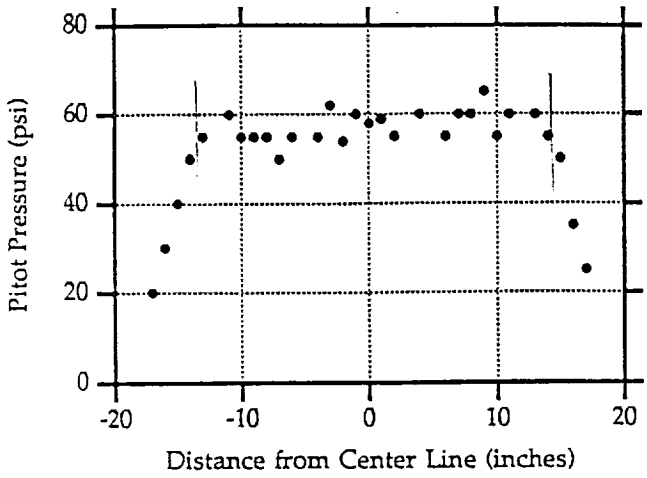

Fig. 6. Pitot pressure profile at nozzle exit.

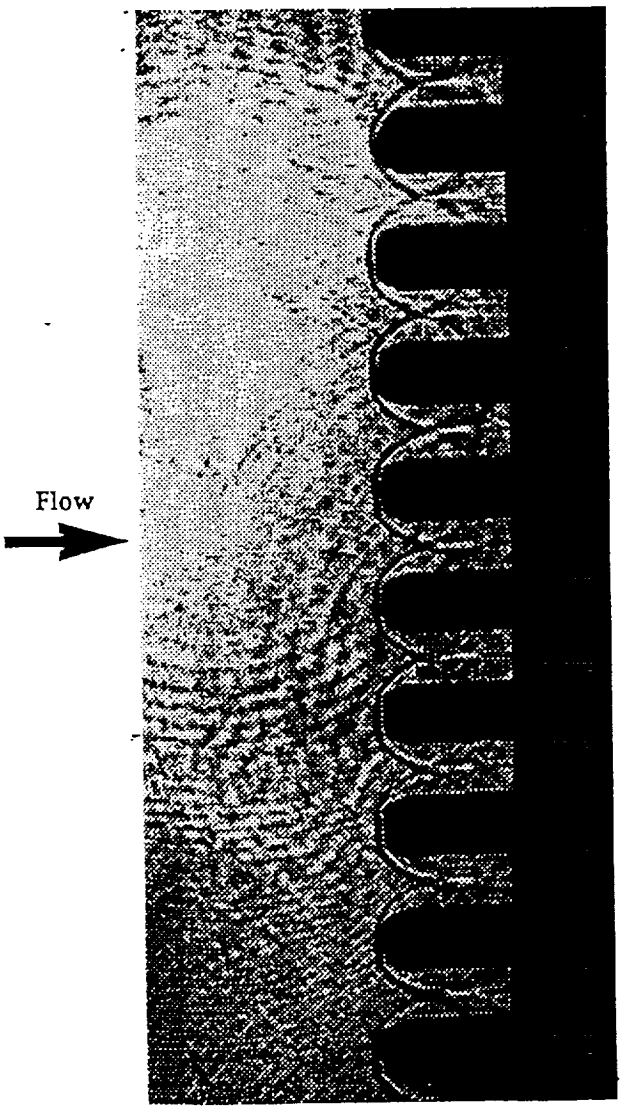

Fig. 7. Shadowgraph of flow over rake in the test cabin.

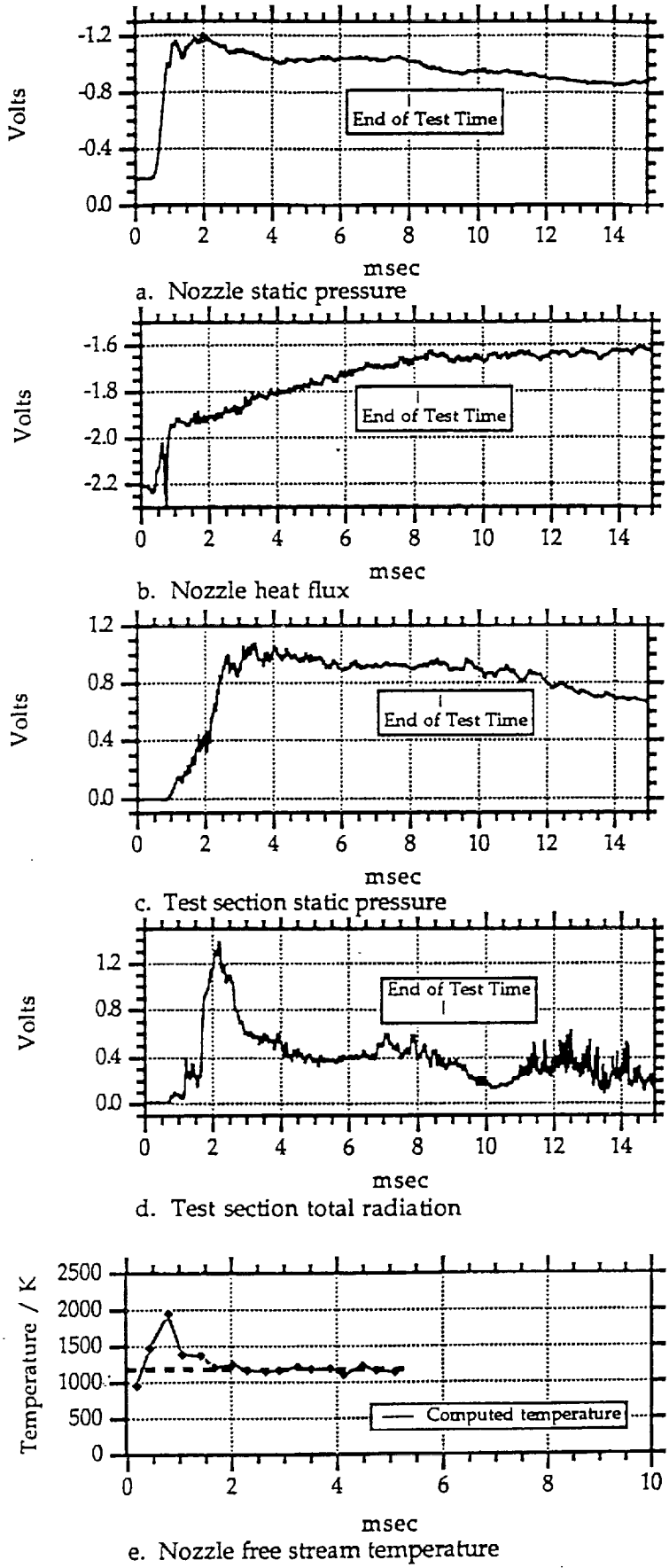

Fig.8. Test time correlations:
Key parameters plotted vs. time.
Nozzle measurements are made at an area ratio of 70.
Test section measurements are made at the nozzle exit.
All data is plotted as voltage signals.

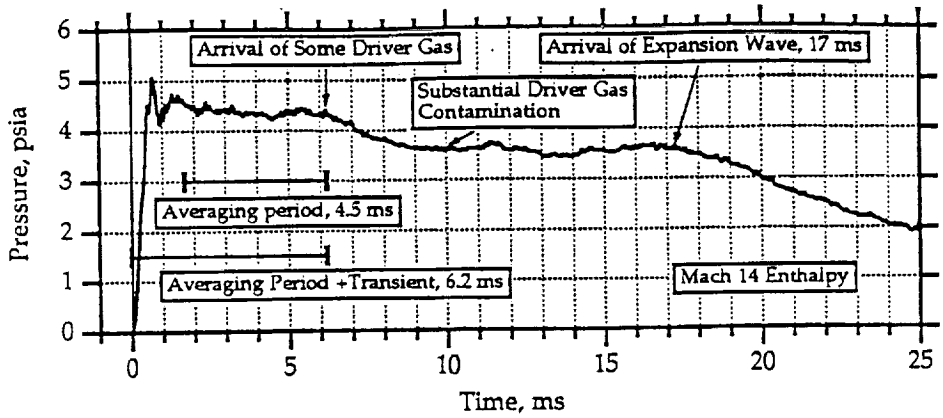

Fig. 9. Expanded and annotated nozzle pressure trace.

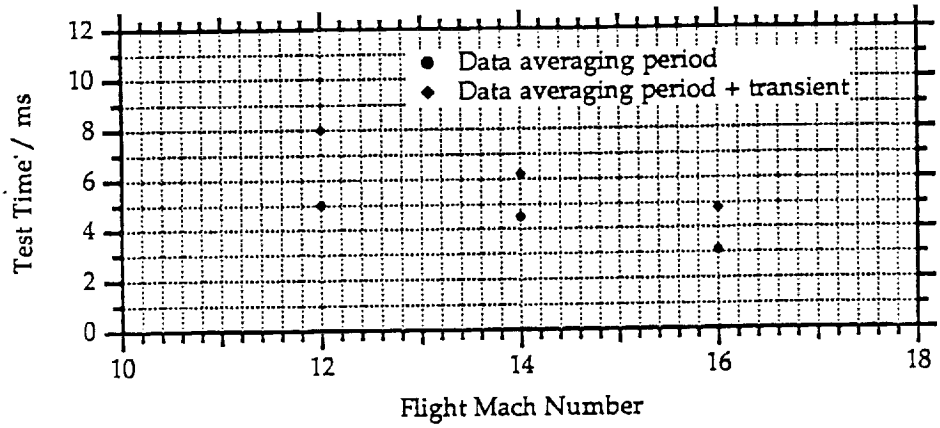

Fig. 10. Test Time versus Simulated Flight Mach Number

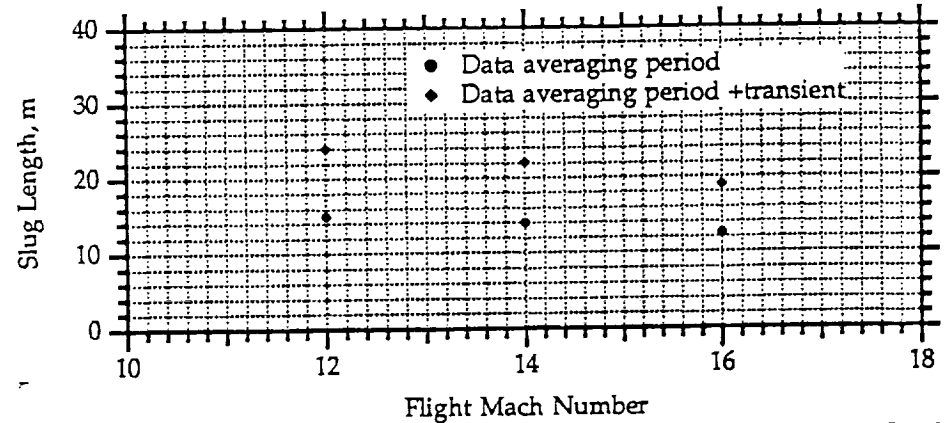

Fig. 11. Slug Length of Test Gas versus Simulated Flight Mach Number

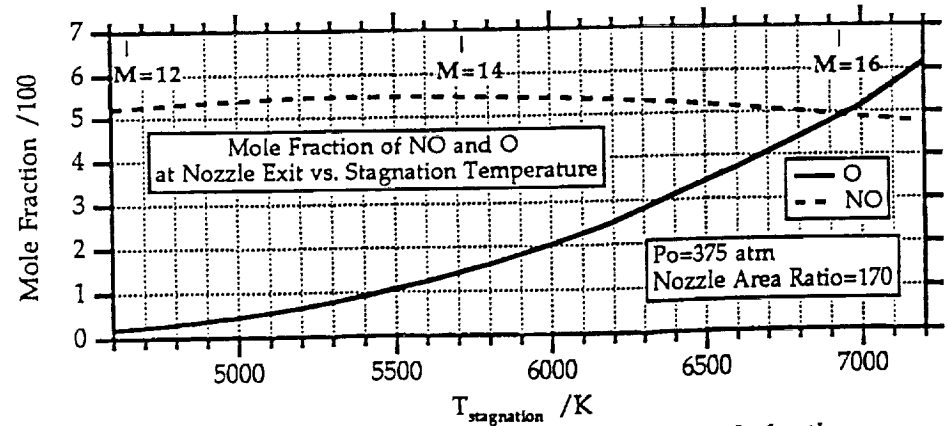

Fig. 12. NENZF computations of NO and O-atom mole fractions versus stagnation temperature and simulated flight Mach number.

AIAA-92-2973

NUMERICAL SIMULATIONS OF NONEQUILIBRIUM SHOCK LAYERS WITH HIGHLY EFFICIENT IMPLICIT SCHEMES

Jean-Luc Cambier and Dinesh K. Prabhu
Eloret Institute
Palo Alto, CA

AIAA 23rd
Plasmadynamics & Lasers Conference
July 6-8, 1992 / Nashville, TN

NUMERICAL SIMULATIONS OF NON-EQUILIBRIUM SHOCK LAYERS WITH EFFICIENT IMPLICIT SCHEMES

Jean-Luc Cambier *, Dinesh K. Prabhu †
Eloret Institute, 3788 Fabian Way, Palo Alto, California 94303

Abstract

Current and future calculations of nonequilibrium shock layers require the use of a very large number of equations, due to a multiplicity of chemical species, excited states, and internal energy modes. The computational cost associated with the use of standard implicit methods becomes prohibitive; it is, therefore, desirable to examine the potential of several methods and determine if any can be projected to be more efficient and accurate for large systems of equations. In this paper we examine the performance of several implicit schemes on some simple practical examples of reacting flows. The Euler equations are solved by three different implicit methods, and two methods of coupling between the fluid dynamics and the chemistry are studied. Several cases of stiffness are considered, and both one and two-dimensional examples are computed. We conclude on with some remarks on the accuracy, stability and efficiency of these various methods.

I. Introduction

The modern Computational Fluid Dynamics (CFD) tools are becoming increasingly useful in computing complex flow conditions, which generally include non-equilibrium phenomena. There is a general need for increasingly complex modeling of the thermo-chemical properties of the gas, and for the modeling of larger systems. For example, the modeling of shock layers around ablating bodies requires a very large set of chemical species and chemical reactions. Although some approximate formulations can be used in the preliminary design phase of space vehicles or experiments, the modeling of the complete kinetics is desirable or even required when the non-equilibrium effects become dominant: this happens for example as the flow expands around the shoulder of a vehicle, or when the object is reduced in size for insertion into an experimental facility. The situation can be further complicated due to the fact that most flows realized in ground-based experimental facilities are themselves not in chemical or thermal equilibrium. Another example concerns highly ionized and radiating flows, which are likely to be found at high re-entry velocities, or their equivalent. It may be required, for these cases of plasma conditions, to account for non-Boltzmann distribution of the excited states. This problem may also require us to model the plasma with a complete collisional-radiative model of the plasma, and convect all the excited states, forcing us to use a large number of equivalent species. In addition, the internal relaxation processes will be locally stiff and difficult to model. These upcoming challenges in CFD technology will require the development of efficient methods for a very large number of species, and for possibly stiff couplings to complex internal processes. Since we want a method that allows us to reach the steady state with minimal computational effort, it seems desirable to use an implicit method. On the other hand, since we may need to couple the hydrodynamics to several other physical processes (collisional-radiative processes, radiation transport, electro-magnetic couplings, etc..), we may favor the use of the Operator-Splitting (OS) method. The latter must be contrasted with the Fully-Coupled (FC) approach, which attempts to provide a more accurate and more stable way to couple the different processes. It is not clear a priori which method is more accurate, stable, efficient, or practical; the use of one method versus the other may depend on the type of flows being computed, the type of computer architecture used, or even the personal preferences of the modeler. During the course of the present work, we will compare the FC and OS methods (for chemistry) and therefore add fuel to the debate. Our search for an efficient numerical method, extendable to large systems, will also include the effect of required grid accuracy on the solution, and its impact on the efficiency of the numerical approaches used.

*Senior Research Scientist, member AIAA. Mailing address: NASA Ames Research Center, MS 230-2, Moffett Field, California 94035.

†Research Scientist, member AIAA

II. Numerical Methods

II-A: The $N \times N$ Block-Tridiagonal method

The Euler equations describe the convective process, and are written (in 1D) as:

$$\frac{\partial}{\partial t}\begin{pmatrix}\rho_1\\ \vdots\\ \rho_n\\ \rho u\\ E\end{pmatrix}+\frac{\partial}{\partial x}\begin{pmatrix}u\rho_1\\ \vdots\\ u\rho_n\\ P+\rho u^2\\ uH\end{pmatrix}=0 \qquad (1)$$

where E, H are respectively the total energy and total enthalpy, per unit volume. The internal energy is $E_i = \sum_s \rho_s \int^T dT' C_{vs}(T')$, and the gas mixture follows the ideal equation of state:

$$P = NkT = (\gamma-1)E_i = (\gamma-1)(E-\frac{1}{2}\rho u^2)$$

The individual species densities are denoted by ρ_s, and $\rho = \sum_s \rho_s$. This formulation is for a single fluid (one mass-averaged velocity), in thermal equilibrium (one temperature). This equation is discretized over a finite size mesh to yield the form:

$$\frac{\Delta \mathbf{Q}_i}{\Delta t} = \mathbf{F}_{i-\frac{1}{2}} - \mathbf{F}_{i+\frac{1}{2}} \qquad (2)$$

where

$$\mathbf{Q} = \begin{pmatrix}\rho_1\\ \vdots\\ \rho_n\\ \rho u\\ E\end{pmatrix}\cdot\mathcal{V} \qquad \mathbf{F} = \begin{pmatrix}u\rho_1\\ \vdots\\ u\rho_n\\ P+\rho u^2\\ uH\end{pmatrix}\cdot\mathcal{S}$$

The subscripts $i, i\pm\frac{1}{2}$ indicate that the variables are evaluated at computational cells (center) i, and cell interfaces $i\pm\frac{1}{2}$. $\mathcal{V}$ and $\mathcal{S}$ are respectively the cell volumes and surfaces. This finite-volume formulation will be used throughout the paper. The equation has been discretized in time as well, and the expression $\Delta\mathbf{Q}$ describes the difference between the flow variable evaluated at two time levels, n and $n+1$. The expression on the RHS of equation (2) must be further specified: the fluxes are a function of $\mathbf{Q}$, and can be evaluated at time level $n+\theta$ through the linearization approximation:

$$\mathbf{F}^{(n+\theta)}_{i+\frac{1}{2}} \simeq \mathbf{F}^{(n)}_{i+\frac{1}{2}} + \theta\mathbf{A}(\mathbf{Q})(\Delta\mathbf{Q})_{i+\frac{1}{2}} \qquad (3)$$

where $\mathbf{A} = \frac{\partial \mathbf{F}}{\partial \mathbf{Q}}$ is the Jacobian matrix. The explicit Euler system of equations is obtained for $\theta = 0$, the implicit system for $\theta = 1$, while second-order time accuracy is obtained for $\theta = 1/2$. Second-order spatial accuracy is achieved by evaluating the fluxes at the cell interfaces $i\pm\frac{1}{2}$:

$$\mathbf{F}_{i\pm\frac{1}{2}} = \frac{1}{2}(\mathbf{F}_i + \mathbf{F}_{i\pm1})$$

A final modification to the fluxes is made to assure monotonicity. The Euler system is an hyperbolic system, and has a set of real eigenvalues (characteristic speeds). The Jacobian can then be written in the form:

$$\mathbf{A} = \mathbf{T}^{-1}\cdot\mathbf{\Lambda}\cdot\mathbf{T} \qquad (4)$$

where the matrix of eigenvalues

$$\mathbf{\Lambda} = \begin{pmatrix}u & & & & \\ & \ddots & & & \\ & & u & & \\ & & & u+c & \\ & & & & u-c\end{pmatrix} \qquad (5)$$

is diagonal and real only, $\mathbf{T}, \mathbf{T}^{-1}$ are transfer matrices between the space of primitive variables $\mathbf{Q}$ and 'characteristic' variables, and c is the speed of sound. The spectrum of eigenvalues can be split into and positive and negative values, which indicate the direction of flow of the characteristic variables at the cell interface. The flux at an interface can now be written as:

$$\mathbf{F}^{(n+\theta)}_{i+\frac{1}{2}} \simeq \mathbf{F}^{(n)}_{i+\frac{1}{2}} + \theta\mathbf{A}^+(\mathbf{Q})\Delta\mathbf{Q}_i + \theta\mathbf{A}^-(\mathbf{Q})\Delta\mathbf{Q}_{i+1} \qquad (6)$$

where

$$\mathbf{A}^\pm = \mathbf{T}^{-1}\cdot\mathbf{\Lambda}^\pm\cdot\mathbf{T}$$

and $\mathbf{\Lambda}^\pm$ is the set of eigenvalues which are respectively positive (negative), zero otherwise. Using this formulation, the discretized version of the Euler equations becomes:

$$\begin{aligned}&[-\theta\Delta t\mathbf{A}^+_{i-\frac{1}{2}}]\Delta\mathbf{Q}_{i-1}\\ &\quad+[1+\theta\Delta t\mathbf{A}^+_{i+\frac{1}{2}} - \theta\Delta t\mathbf{A}^-_{i-\frac{1}{2}}]\Delta\mathbf{Q}_i\\ &\quad+[\theta\Delta t\mathbf{A}^-_{i+\frac{1}{2}}]\Delta\mathbf{Q}_{i+1} = \mathbf{F}^{(n)}_{i-\frac{1}{2}} - \mathbf{F}^{(n)}_{i+\frac{1}{2}}\end{aligned} \qquad (7)$$

The RHS of equation (7) can be modifed for monotonicity, while conserving its second-order accuracy in space. The technique used throughout this work follows closely the TVD method of Harten [1]. Greater stability is generally obtained if the implicit LHS of equation (7) has its spatial accuracy reduced to first order. This consists in evaluating the Jacobian matrices at the cell centers, according to the

characteristic flow direction. The final version of the system is obtained for the fully implicit case ($\theta = 1$):

$$[-\mathbf{A}^+_{i-1}\Delta t]\Delta\mathbf{Q}_{i-1} + [1 + \mathbf{A}^+_i\Delta t - \mathbf{A}^-_i\Delta t]\Delta\mathbf{Q}_i + [\mathbf{A}^-_{i+1}\Delta t]\Delta\mathbf{Q}_{i+1} = RHS^{(n)} \quad (8)$$

This is a tridiagonal system of $N \times N$ block matrices, where $N = N_s + D + 1$, N_s is the number of species, D is the spatial dimensionality. Solving this system can be done by the standard technique of gaussian elimination and back substitution, with LU decomposition of the block matrices (see for example [2]). This requires that the matrices that compose the diagonal band be inverted twice for each grid point. It turns out that the corresponding algorithm has a number of operations that scales as N^3. This technique is called the $N \times N$ Block-Tridiagonal solver, and will be used in this paper.

A similar approach can be used for 2-dimensional flow, leading to a pentadiagonal system of $N \times N$ bock matrices. Another approach, which consumes less memory and has a lower number of operations, uses the technique of dimensional splitting [3]: we effectively solve the tridiagonal system twice, once for each direction†. This is the approach used here.

II-B: The Scalar Tridiagonal method

It is clear that as the number of species grows, the N^3 dependence of the computational load will rapidly make this technique impractical. It is desirable then to search for a method that scales less rapidly with the number of species. One such method can be easily obtained by considerable simplification of the matrix structure. Note that the split Jacobians are bounded respectively from below and above:

$$\mathbf{A}^+ = \mathbf{T}^{-1}.\mathbf{\Lambda}^+.\mathbf{T} < \max\{\lambda\} \cdot \mathbf{1} \quad (9)$$

$$\mathbf{A}^- = \mathbf{T}^{-1}.\mathbf{\Lambda}^-.\mathbf{T} > \min\{\lambda\} \cdot \mathbf{1} \quad (10)$$

where we have used the (signed) maximum and minimum eigenvalue present in $\mathbf{\Lambda}$. The Jacobian matrices, thus replaced into equation (8) are proportional to the unit matrix. There is only a scalar operation to perform, instead of a full block matrix inversion. The number of operations now scales as N: this scheme is called the Scalar-Tridiagonal solver, and will be compared to the previous one.

†This splitting *is* a form of Operator-Splitting.

There are several disadvantages to the scalar technique: the first, loss of time accuracy, is not of immediate relevance, since we are mostly concerned with the achievement of steady-state. The second is a loss of accuracy: this is specially of concern in subsonic regions, where the spectrum of eigenvalues is originally very different from the maximum (minimum) value. In supersonic or hypersonic regions, this is not a problem, since $u >> c$, and $\Lambda \simeq u\mathbf{1}$, i.e. the spectrum is nearly scalar. We may expect therefore some loss of accuracy, or even stability, when using the scalar method.

II-C: The N_s-Split Tridiagonal method

We will also investigate another method, based on the formulation of a multi-fluid system of equations. Let us consider the following system of equations:

$$\frac{\partial}{\partial t}\begin{pmatrix}\rho_s\\ \rho_s u\\ E_s\end{pmatrix} + \frac{\partial}{\partial x}\begin{pmatrix}u\rho_s\\ P_s + \rho_s u^2\\ uH_s\end{pmatrix} = 0 \quad (11)$$

and similar systems for other species. In this formulation, each species is attributed its own momentum density and energy density. In the limit of very strong coupling between the momentum and energy densities of each fluid component, we can enforce a unique velocity and unique temperature for this multi-fluid description. If we were to solve each subsystem by the block tridiagonal method, we would require the inversion of a 3×3 (4×4 in 2 dimensions) matrix. We repeat the method for each species, and the overall cost now scales as N_s. For a large number of species, we expect a cross-over between this method and the $N \times N$ block method, by comparing the costs; for example, $4^3 N_s$ versus $(N_s + 3)^3$. However, a further reduction in cost can be achieved with the following approximation. Assuming that all species have nearly equal molecular masses, and that their individual specific heats are nearly equal, we can replace the partial pressure:

$$p_s = n_s \hat{R} T \simeq \frac{\rho_s}{\rho} P$$

and use a constant average $\bar{\gamma}$ in the formulation of the derivatives which compose the Jacobians. These Jacobian matrices become then identical. This has a rather drastic effect: the block matrix inversions need to be performed once, instead of once for each species. This lowers considerably the overall CPU requirement. This formulation of the solver will be called N_s-Split Tridiagonal solver, and will compared with the two previous ones.

II-D: Hydrodynamics-Chemistry Coupling

In the equations considered so far, the source terms on the RHS are non existent; for a reacting gas, there will be a source term $\dot{\mathbf{W}}$ which operates on the species densities only. The total energy now includes the energies of formation:

$$E = E_i + \frac{1}{2}\rho u^2 + \sum_s e_s^o$$

and is not not affected by the chemical reactions: the internal energy is obtained from the conserved total energy, after subtracting the kinetic and formation energies. The change in formation energy of the mixture, due to chemical reactions, will thus be converted into a change of temperature.

The chemical source term can be treated implicitely as well: if Ω is the corresponding Jacobian for the source term ($\Omega = \frac{\partial \dot{\mathbf{W}}}{\partial \mathbf{Q}}$), solving for the chemistry alone would read as:

$$[1 + \Omega_i \Delta t]\Delta_{\text{ch}}\mathbf{Q} = \dot{\mathbf{W}}_i^{(n)}\Delta t \qquad (12)$$

By solving separately for the convective and chemical terms, one obtains two variations at the end of the computational step: the global variation will then be a direct sum of the the contribution from each process.

$$\Delta\mathbf{Q} = \Delta_{\text{cv}}\mathbf{Q} + \Delta_{\text{ch}}\mathbf{Q} \qquad (13)$$

This procedure is called† the Explicit-Coupling method (EC).

We see that in effect, we have split the computation in two parts, for each physical process. For that reason, this method is also called the Operator-Splitting (OS) method (see for example [3]). Another form of operator splitting consists in using the change induced by one process as a starting point for the other process: a temporary solution $\tilde{\mathbf{Q}}$ is used, such that:

$$\tilde{\mathbf{Q}} = \mathbf{Q}^{(n)} + \Delta_{\text{cv}}\mathbf{Q} \qquad (14)$$

$$\mathbf{Q}^{(n+1)} = \tilde{\mathbf{Q}} + \Delta_{\text{ch}}\tilde{\mathbf{Q}} \qquad (15)$$

where now the change induced by chemistry is obtained by using the modified solution $\tilde{\mathbf{Q}}$ in the expression of the source term and Jacobian, $\dot{\mathbf{W}}, \Omega$ in eq. (12). This formulation of the Operator-Splitting method is based on fractional steps, and is best described in [4]. Since we will examine both methods, we will reserve the term Explicit-Coupling (EC) for the method described in eq. (13), and the term Operator-Splitting (OS) when using the method described by eqs. (14) and (15).

† Also called the Loosely-Coupled approach.

Another approach is to solve for both the convective and chemical processes simultaneously. The chemical Jacobians can be brought into the LHS, and equation (8) is modified to:

$$\begin{aligned}[-\mathbf{A}_{i-1}^{+}\Delta t]\Delta\mathbf{Q}_{i-1} \\ +[1 + \mathbf{A}_i^{+}\Delta t - \mathbf{A}_i^{-}\Delta t + \Omega_i\Delta t]\Delta\mathbf{Q}_i \\ +[\mathbf{A}_{i+1}^{-}\Delta t]\Delta\mathbf{Q}_{i+1} = RHS^{(n)}\end{aligned} \qquad (16)$$

where now the RHS includes the evaluation of the chemical source terms at time level (n). This method is called the Implicit, or Fully-Coupled (FC) approach. The Ω matrix is dense, and the FC approach described above is possible only when combined with the $N \times N$ Block-Tridiagonal solver. Including it in the N_s-Split solver would require serious modifications, and has not been attempted here. Similarly, by approximating the Jacobian Ω by a scalar (using again the maximum eigenvalue), one could use the FC approach with the Scalar Tridiagonal solver. We found that in many cases this approximation usually leads to very poor results for the chemistry, and will not be used here.

II-E: Chemistry Sub-Cycling

There are additional modifications one can make when using the OS or EC approaches: since the fluid dynamics and chemistry are computed separately for a global time step Δt, one has considerable flexibility in the methods used for each process. Notably, the accuracy of the chemistry can potentially be improved by sub-iterating (more precisely subcycling) the chemistry by using smaller time steps δt. This may be required to improve the accuracy, because the chemical reactions are non-linear processes: linearization errors become important in some highly non-equilibrium situations. The coupling of the chemistry to the temperature can also be estimated at each sub-step, by looking at the change induced in the average formation energy of the mixture. When the chemistry is sub-iterated (SI), the global variation is obtained by using eq. (13), but when the global change due to chemistry is obtained as follows, using sub-iterations ($m = 1, 2, \ldots$) of the chemistry:

$$\Delta_{\text{ch}}\mathbf{Q}^{(m+1)} = \Delta_{\text{ch}}\mathbf{Q}^{(m)} + [\mathbf{1} + \Omega\delta t]^{-1}\,\dot{\mathbf{W}}\delta t \qquad (17)$$

Finally, the coupling of the chemistry to the convection can also be computed at each sub-step. For

example, after computing the variation $\Delta_{cv}\mathbf{Q}$ using one of the Tridiagonal solver listed above, one can linearize it during the global time interval. The global variation (for both processes) is then obtained as follows:

$$\Delta\mathbf{Q}^{(m+1)} = \Delta\mathbf{Q}^{(m)} + [1 + \Omega\delta t]^{-1}\dot{\mathbf{W}}\delta t + \frac{\Delta_{cv}\mathbf{Q}}{\Delta t}\delta t \qquad (18)$$

This formulation replaces equation (13). We will reserve the term Sub-Iterated Coupling (SIC) to describe this particular form of the splitting method between chemistry and convection.

II-F: Performance

The methods used can be classified, according to the treatment of the convective process and the method of coupling with the chemistry: the designation of the methods which will be studied are listed in Table 1.

The relative performance of all schemes is demonstrated in Figure 1. Figure 1-a (top) shows the CPU spent (per iteration and per grid point) by an implicit method, normalized by the same quantity for the explicit method. Since the explicit method scales almost exactly as the number of equations, both the Scalar and the N_s-Split method will show a nearly flat behavior when plotted versus the number of species. This is confirmed in Figure 1-a. Notice also that the relative cost of the Scalar method is very small, while the $N \times N$ Block method climbs very rapidly: the latter is still quite expensive, even for a small number of species. The leftmost data point at $N_s = 5$, for example, shows that the $N \times N$ Block method is 10 times more expensive than the explicit method. Although this number is not an absolute, and can be reduced after a strong effort in code writing (by 'hard-wiring' the operations, for example). At best, this time may be reduced by a factor of two. Still, the conclusion is inevitable: as the number of species grows, the implicit scheme is efficient only if it can be operated at large CFL numbers. Practically speaking, stability limitations will limit the CFL to the neighborhood of 4-5. These stability problems arise from transient phenomena, dimensional split errors and/or coupling errors with the chemistry or other internal relaxation processes. Higher values of CFL number can potentially be achieved when the flow is very close to the steady state and when the flow is non-stiff. Since we are mostly interested into reaching the steady state (and having to go through the transients) and into stiff problems, this is of little interest to us. These limitations will be demonstrated on some practical sample cases in the next sections.

III. One-Dimensional Shock

As a first test case, we will model the propagation of a 1-dimensional shock, from an impulsive start. This case will mimic the establishement of a two-dimensional shock layer around a blunt body. We use a grid of 200 cells, evenly spaced, with a perfectly reflecting wall on the right hand side. The flow is incoming from the left at high velocity, and impinges on the wall. A shock is created at the reflection and propagates back upstream into the hypersonic flow. Although strictly speaking this flow is unsteady, the profiles become steady in a frame attached to the shock. The gas is air, composed of 5 species (N, O, N_2, O_2, NO), the free stream Mach number is $M_\infty = 15$, the free-stream temperature is $T_\infty = 300°K$. Three cases of free-stream pressure will be considered, leading to three stiffness conditions:

$$\begin{aligned} \text{case1}: &\quad P_\infty = 10^{-5}\text{atm} \\ \text{case2}: &\quad P_\infty = 10^{-4}\text{atm} \\ \text{case3}: &\quad P_\infty = 10^{-2}\text{atm} \end{aligned}$$

The stiffness is defined as the ratio of the largest time scale (here presumably the convective one) to the smallest (chemistry). The convective time scale is obtained from the choice of Courant (CFL) number we choose to run the simulation at. The chemistry time scale can be defined in two ways:

- an intrinsic time scale, obtained from the maximum rate of change of any chemical specie. For example, the chemical time scale will be the time required for a specie molar fraction to change by more than 10%, provided it is not close to zero initially.
- a coupling time scale, defined as the time required for the chemistry to modify any flow variable by (say) more than 5%. Since the chemistry affects mostly the temperature, this is the variable used in that case.

The second time scale provides a global limitation on the time step to be used: if the chemical effects dramatically change the formation energy of the mixture during the time step, and if this δe^o is large compared to the internal energy, the numerical solution becomes rapidly unstable. This has a profound effect on the choice of numerical methods to be used, for example, in combustion. In the remainder of this

paper, we always limit the global time step such that the estimated relative change in temperature, induced by chemical reactions, is smaller or equal to 5%. We allow the use of large (CFL> 1) global time steps provided this condition is satisfied. Let us emphasize that this restriction still allows us to consider stiff problems, where the stiffness is defined by using the intrinsic chemical time scale. Chemical equilibrium can be reached rapidly, without significantly modifying the temperature; the flow conditions simply must be such that the equilibrium values are not very different from the initial values, or that the energies of formation are relatively small compared to the internal energy.

The results presented in this section are obtained using the following methods†:

1 FC/Block tridiagonal
2 OS/Block tridiagonal
3 EC/Block tridiagonal
4 EC/Scalar tridiagonal
5 EC/N_s – Split tridiagonal

The chemistry is always computed with a single iteration.

Let us look first at case 1, for $P_\infty = 10^{-5}$ atm. The profiles of temperature are shown (left scale on the plots) as well as the mole fractions of N and O atoms (right scale on the plots). Figure 2 shows these profiles for a calculation at CFL=2 and 4. Figure 2-a shows only the results for the FC/Block, EC/Scalar and EC/N_s-Split methods: the remaining cases of EC/Block and OS/Block would show profiles exactly identical to the FC/Block method. The agreement between the other methods is also quite good. This is also true for the CFL=4 case (Figure 2-b, bottom), although to a lesser extent: in this figure, the curves for the EC/Block case are omitted, since they are identical to the FC/Block results. It appears therefore for this case that the EC and OS methods are as accurate as the FC method. The N_s-Split method shows slight errors in species concentrations near the shock, in the region of highest concentration gradients, which worsen as the CFL number grows. The Scalar method has an overshoot at CFL=2, and cannot be operated at larger CFL numbers. All methods fail for larger CFL values.

Figure 3 shows the same profiles (obtained when the shock reaches the same position) for a slightly stiffer problem (case 2). Again, we had perfect agreement between the OS/Block, EC/Block and FC/Block methods, and the EC/Block profiles were omitted for clarity. The overshoots in mole fraction near the shock, for the N_s-Split method, are worse for this stiffer case. Again, the Scalar method works reasonably well for CFL=2, but fails for larger values. These calculations were done using the standard *minmod* limiter in the convective fluxes, as described by Harten [3], with an entropy fix $\epsilon \simeq 0.1$. When using a more compressive flux-limiter, such as the 'Superbee' limiter, the calculation could proceed as well, although with very slight oscillations. Reducing the entropy parameter to $\epsilon \simeq 0.01$ would lead to more severe oscillations. Therefore the rapid elimination of the transients can be best achieved by ensuring that sufficient numerical diffusion is present. The final flow solution therefore would need to be further sharpened, when the steady state is nearly achieved.

Figure 4 shows the stiffest case for CFL=2. All methods failed for larger CFL values. It is remarkable that the FC/Block method failed for this case, while the EC/Block method gives the best results. The OS/Block method (which uses the fractional step approach) gives very similar results, and can be considered as accurate. Surprisingly, the EC/Scalar method is stable, although the species profiles show an unphysical kink in the relaxation region. In order to better determine which method is more accurate, we computed the same case on a larger grid (2000 points) using the FC/Block method. By increasing the grid density, we achieved a ten-fold reduction of the stiffness of the problem. The FC/Block was then run successfully, and gave a very short relaxation zone (see Figure 4b). We also attempted to better reproduce this relaxation on the coarse (200 points) grid by either 1) sub-cycling the chemistry or 2) reducing the time step. Figure 4b shows the comparison, for example between the FC/Block results computed on the high-density grid, with the EC/Scalar with 10 sub-iterations of the chemistry and an explicit calculation (CFL=0.2). The two latter cases are not very different from the results of Figure 4a, i.e., neither the sub-iterations nor the time step reduction greatly improve the solution. It seems that all methods tend to overestimate the length of the chemical relaxation zone in stiff cases, although the final equilibrium result is accurate. We must conclude also that the EC or OS methods are more stable than the FC method in stiff cases: we also observed this feature on other stiff cases. The mixing of non-diagonal elements in the global Jacobians, between convective and chemical terms, may make the

†The notation used has been mentioned in the previous section, and is summarized in Table 1.

matrices more prone to ill-conditionality, and reduce the stability.

It seems therefore that only relatively small values of the CFL number can be effectively used for the transients, and therefore only the Scalar method, so far, is efficient. However, it is not accurate enough when the chemistry is very stiff. It also appears that the N_s-Split method, in its current form, suffers from unphysical numerical species diffusion in the region of strong gradients, and for large time steps (this error is inexistent in the explicit regime). Since there are other cases where implicit methods can have a significant impact, we will look also at expanding flows in the next section.

IV. One-Dimensional Nozzle

We will model a converging/diverging nozzle, with 150 grid points in the axial direction: the calculations were performed using two-dimensional codes, and the grid used 10 points in the radial direction. Since we were interested only into axial profiles, this was considered sufficient for our purposes. Notice that now there will be an additional error due to the dimensional split in the implicit methods. The left boundary condition and initial state considered a gas at a pressure of 4.205 atm and 1000°K. However, the gas composition was arbitrarily set to non equilibrium values by increasing the amount of dissociation: this had the effect of stiffening the chemistry in the subsonic region of the nozzle. The calculations were always started impulsively, and run at CFL< 1 (explicit) until the shock exits the nozzle, before the implicit models were tried. We used this case to evaluate the effect of sub-iterations and sub-coupling in the chemistry.

Figure 5 shows the comparison of residual history for the 4 implicit methods used, i.e. FC/Block, EC/Block, EC/Scalar and EC/N_s-Split, and without any sub-iterations or sub-coupling. The residual of the subsonic zone (solid line) and supersonic zone (dotted line) have been shown separately. A first break point in the curves shows the end of the explicit pre-calculation, used for elimination of the shock from the nozzle. The implicit scheme is then used, with a constant CFL=1.5, until a time of 5 milliseconds. At that point, the calculation is pursued further for the supersonic region only, the subsonic region remaining frozen. The residual shown is for the total energy, and is averaged over the entire volume of the region considered.

Figure 5-a shows the results for the FC/Block method, Figure 5-b for the EC/Block method. Both show good convergence properties, with a slight improvement for the EC/Block method. The N_s-Split method (Figure 5-c) has even better convergence properties, but the Scalar method (Figure 5-d) shows a non-vanishing residual for the subsonic region. All methods converge rapidly in the supersonic region when computed separately, indicating that most of the problems (if any) are located in the subsonic region.

The solutions obtained at 5 milliseconds are plotted in Figure 6, for the atomic oxygen mole fraction. The solution for the scalar method is slightly in error in the subsonic region, but quickly recovers during the expansion and leads to the correct final value. The N_s-Split method has the opposite behavior, i.e. has an error increasing with the distance along the nozzle: it seems that the species convection suffers from some unphysical diffusion of species, also noticed in the results of the previous section: there is a phase error between each species convection, which is irreversible. By contrast, the Scalar method correctly propagates the species, but does not accurately couple the convection with the momentum and energy equations. This may lead to fluctuations in pressure or temperature, which quickly disappear when the flow becomes near supersonic.

The use of sub-iterations in the chemistry did not change the results for this case. Increasing the stagnation pressure and the stiffness slowly lead to noticeable effects. The most dramatic differences between the cases of sub-iterated and non-iterated chemistry were observed for very stiff systems, at the limit of stability. In order to demonstrate the effect of sub-iterations, or sub-cycling of the chemistry, we consider a high pressure (400 atmospheres) case, with an initial temperature of 6000 ^oK, and a highly non-equilibrium initial composition (non-dissociated air). A constant time step of 5×10^{-8} seconds was assumed. Figure 7 shows the results of the chemistry integration (no fluid dynamics) for both non-iterated and sub-iterated (20 cycles) cases. It is clear that a single step of the chemical integration, with $\Delta t = 5 \times 10^{-8}$ sec, leads to very large changes in species concentrations and temperature. This will significantly affect the remainder of the history of the chemical integration. If the time step is not too large, the correct equilibrium values may be obtained in the final steady state: if the time step is large enough, unphysical values (i.e. negative concentrations) may be obtained during the first step,

and the correct solution cannot be recovered. By using a smaller time step (10^{-8} sec), both methods give essentially the same history, and the same final values, which agree with the values obtained in Figure 7 for the sub-iterated case. It is clear then that in some severe cases, the sub-iteration of the chemistry can yield a higher stability and a higher accuracy: these cases may be found for example in high-pressure shocks, detonations, or strong ionizing shocks, when the grid used is coarse.

The method of sub-coupling was also tested on some other stiff cases. It was found that the stability was slightly reduced when the sub-coupling was incorporated. When the chemistry is sub-iterated and sub-coupled, the convection of species during the sub-step δt is estimated and included in the variation. While this process accounts for the effect of the convection on the chemistry, it fails to account for the reverse process, and it fails to account for the influence of other convective terms, specifically the pressure waves. The coupling of the chemistry is not 'in phase' with all the convective equations. In subsonic regions and behind shock waves, the pressure waves are a dominant process, and a significant error is made. We therefore recommend that no sub-coupling (SIC) be used if the chemistry is sub-iterated.

V: Two-Dimensional Shock Layer

The final test will be done for a 2-dimensional, axi-symmetric flow around a blunt body. This is a typical flow configuration of interest. The flow is modeled with a 144×80 grid, the free stream Mach number is $M_\infty = 25$, the free stream temperature and pressure are $T_\infty = 241.75$°K and $P_\infty = 1.65\ 10^{-4}$ atm; the free stream is air, modeled using 11 species $N, O, N_2, O_2, NO, N^+, O^+, N_2^+, O_2^+, NO^+, e^-$ and a 15 reaction set from Dunn & Kang [5]. The blunt body shape is taken from the Apollo spacecraft.

The calculations were proceeded with the FC/Block method and the OS/Scalar method. Since the chemical changes were quite important in the shock layer, our restriction in time step due to the temperature changes (relative change < 5%, see section III) prevented us to compute the flow implicitely. Any attempt to increase the time step, and therefore to allow a larger change in temperature due to chemical effects led very quickly to flow instabilities. The comparison presented below is therefore between a FC/Block implicit method run at small time steps, and an Operator-Split method where the fluid dynamics are computed explicitely. The pressure behind the shock is close to 0.5 atmospheres, with a temperature between 8,000 and 12,000 °K, and the chemistry is rather stiff, especially due to the reactions involving electrons. Figure 8 shows the comparison between the two methods along the stagnation line, and the agreement is very satisfactory.

There is a lack of resolution of the shock front, and we proceeded to improve the results by adapting the grid in the neighborhood of the shock. Several adaptions were performed, first on the temperature gradients, then on the chemical gradients (N_2). After each adaption, the flow was computed further until convergence. The adaption procedure used the SAGE code [6] developed at Ames, and affected grid points in a direction normal to the blunt surface only. Figure 9 shows the comparison between the original, non-adapted solution and the results from the final adaption. Since the results from the FC/Block and OS/Scalar methods were found to be agreement, and since the latter method is considerably more efficient, only the OS/Scalar method was used for the adapted cases. We see in Figure 9 that the peak temperature has changed significantly (15 %), and so has the shock location. Although the flow variables relax to the same values in the midst of the shock layer, the unresolved relaxation zone may still affect some important engineering variables, such as the radiative heating at the wall. The radiative emission power behind the shock will depend strongly on the temperature and species densities, both varying rapidly in that region, and being very sensitive to the grid resolution. Therefore, a radiation code was used to compute the intensity along the line-of-sight in the stagnation region, and the heat flux at the wall: this computation was performed after the flow steady state was obtained, i.e. the flow and radiation were not coupled. After each adaption, the change in radiative heat flux was computed and compared: the results are shown in Table 2, for both the optically thin case and the optically thick case. In the former case, the relative changes are quite large, and the values converge slowly. In the thick case, the absorption by the core of the shock layer tends to damp the perturbations: for that case, we see that the heat flux converges more rapidly towards a final value. Since the relative change is small (-1.8%) after the 3^{rd} adaption, we considered that the resolution was now sufficient. The comparison in radiative spectrum at the wall between the unadapted and final solution is shown in Figure 10. Most of the changes occur in the UV region.

It is important to remark that the computed radiation did not include the continuous spectrum, and therefore the variations in radiative heating at the wall may be under-estimated. Additionally, the density is sufficiently large in this example that equilibrium radiation can be assumed: this considerably reduces the uncertainty in the computation of the radiative flux. For lower density and higher velocity cases, one must include thermal non-equilibrium effects. The relaxation zone becomes then even more important to resolve accurately.

It appears from this example that in practice it will be very difficult to compute a flow using an implicit method with a large CFL number, and that hydrodynamics-chemistry coupling effects will sometimes limit the time step to CFL values below 1. Additionally, we may be required in practice to transform the grid, according to the solution obtained, in order to reach the desired accuracy: these adaptions need to be performed several times. It would seem therefore that a more efficient approach would combine the flow computation with the grid refinement. Indeed, there is a technique that can potentially lead to more efficient computations: using unstructured grids, the computational cells can be subdivided at will to give better accuracy in the regions that need it. Similarly, the subdivided cells can be regrouped in regions of low gradients, in order to keep the total number of cells within reasonable limits. Such a technique would use a small number of cells to start with, and progressively refine them: most of the transients would then be computed using a small number of cells, leading to a more efficient procedure.

VI: Conclusions and Recommendations

We have not used here all the possible variations on the implicit schemes, neither have we exhausted the methods of coupling the chemistry and the fluid dynamics. We have however used techniques which are commonly used, and, we hope, demonstrated the trends for practical problems. We can draw several conclusions from this study:

1. It is clear that on many problems of interest, the calculations cannot proceed with very large CFL numbers during the approach to steady state. Inevitably, for large numbers of species, the Block Tridiagonal methods cease to be efficient in that regime. Only Scalar Tridiagonal methods, or even explicit methods remain efficient.

2. It is clear that the Operator-Splitting approach, including the Explicit-Coupling between chemistry and hydrodynamics, is at least as accurate as the Fully Coupled, and apparently more stable for very stiff problems. Sub-iterations of the chemistry can further improve the accuracy and stability in the most severe cases of stiffness.

3. The N_s-Split method, at least in its present formulation, is too inaccurate for large time steps or strong concentration gradients. This disapointing result is not completely understood at the moment. It does not affect our conclusions, since the method is less performant than the Scalar method. This results should however be investigated further, since it may have implications on other systems, such as a two- or three-fluid plasma, where the implicit treatment of the electron component gas dynamics is mandatory.

4. Calculations of shock layers on fixed grids may not be sufficiently accurate if radiative phenomena or thermal non-equilibrium effects must be considered. In the example shown, several iterations at grid adaption were necessary. Other calculations on similar problems were also performed, that supported this conclusion. It appears then that dynamical grid adapting should be performed during the course of the calculation, for higher efficiency.

Dynamic grid refinement could lead to even higher efficiencies if both the distribution and the overall number of grid points are allowed to vary. This can be done on structured as well as unstructured grids. The construction of implicit schemes on unstructured grids would be quite complex. However, we have concluded that this may not be a restriction for many cases. An explicit algorithm will therefore be sufficient, and the technique is reduced to a sophisticated book-keeping problem. In addition, the use of explicit, Operator-Split techniques allows us to take advantage of massively parallel (or mixed) computer architectures. This method will be investigated in the future.

We have not mentioned another technique applicable for Operator-Split methods, when the chemistry is very stiff. The chemistry (or other internal process) can be rescaled, or 'slowed-down' artificially: this may have the effect of increasing the relaxation distances. However, we have made preliminary calculations that seem to indicate that in the very severe cases of stiffness, the changes are not perceptible. In addition, this procedure can be used

during the elimination of the transients, then the rescaling is progressively eliminated until a steady state with the proper time scale is obtained. If the rescaling is not eliminated, a false steady solution is obtained. The influence of the numerical procedure on the steady solution is also a serious question, discussed recently by Lafon & Yee [7]. They show that for flows coupled with non-linear source terms, the steady state reached may depend on the path used to reach it. It is clear therefore that the errors induced by the numerical procedures can never be under-estimated, and that all users of CFD should proceed with extreme caution.

VII. References

[1] A. Harten, *J. Comp. Phys.*, vol 49 (1983), pp. 357-393.

[2] G. Sod, *Numerical Methods in Fluid Dynamics*, Cambridge University Press, 1985.

[3] E. Oran & J. Boris, *Numerical SImulation of Reactive Flow*, page 130, Elsevier Publ., 1987.

[4] N. Yanenko, *The Method of Fractional Steps*, Springer-Verlag, 1971.

[5] M. Dunn & S-W. Kang, 'Theoretical and Experimental Studies of Reentry Plasmas', NASA-CR-2232.

[6] C. Davies & E. Venkatapathy, 'Application of a Solution Adaptive Grid Scheme, SAGE, to Complex Three-Dimensional Flows', AIAA 10^{th} CFD Conference, Honolulu, Hawaii 1991. AIAA paper 91-1594.

[7] A. Lafon & H.C. Yee, 'On the Numerical Treatment of Nonlinear Source Terms in Reaction-Convection Equations', AIAA paper 92-0419.

designation	Treatment of hydrodynamics	Chemistry/Convection coupling method
FC/Block	$N \times N$ Block Tridiagonal (section II-A)	Implicit (or Fully-) coupled
EC/Block	$N \times N$ Block Tridiagonal (section II-A)	Explicit (or Loosely-) coupled
OS/Block	$N \times N$ Block Tridiagonal (section II-A)	Operator-Split (or Fractional Step)
EC/Scalar	Scalar Tridiagonal (section II-B)	Explicit coupling
EC/N_s-Split	N_s-split method (section II-C)	Explicit coupling
EC-SI/Block	$N \times N$ Block Tridiagonal	Explicit with Sub-Iterations (or Sub-Cycling)
EC-SIC/Block	$N \times N$ Block Tridiagonal	Explicit, Sub-Iterations *and* Sub-Coupling

Table 1: Designation of numerical methods and coupling methods used in this study.

Grid Cycle	Relative Change in Surface Flux Optically Thin Gas [2000-8000 Å]	Relative Change in Surface Flux Optically Thick Gas [1740-1750 Å]
Non-adapted Grid - Adaption 1	-25.1 %	-11.0 %
Adaption 1 - Adaption 2	+27.1 %	+5.2 %
Adaption 2 - Adaption 3	-3.5 %	-1.8 %

Table 2: Axisymmetric blunt body calculations - results of grid adaption study.

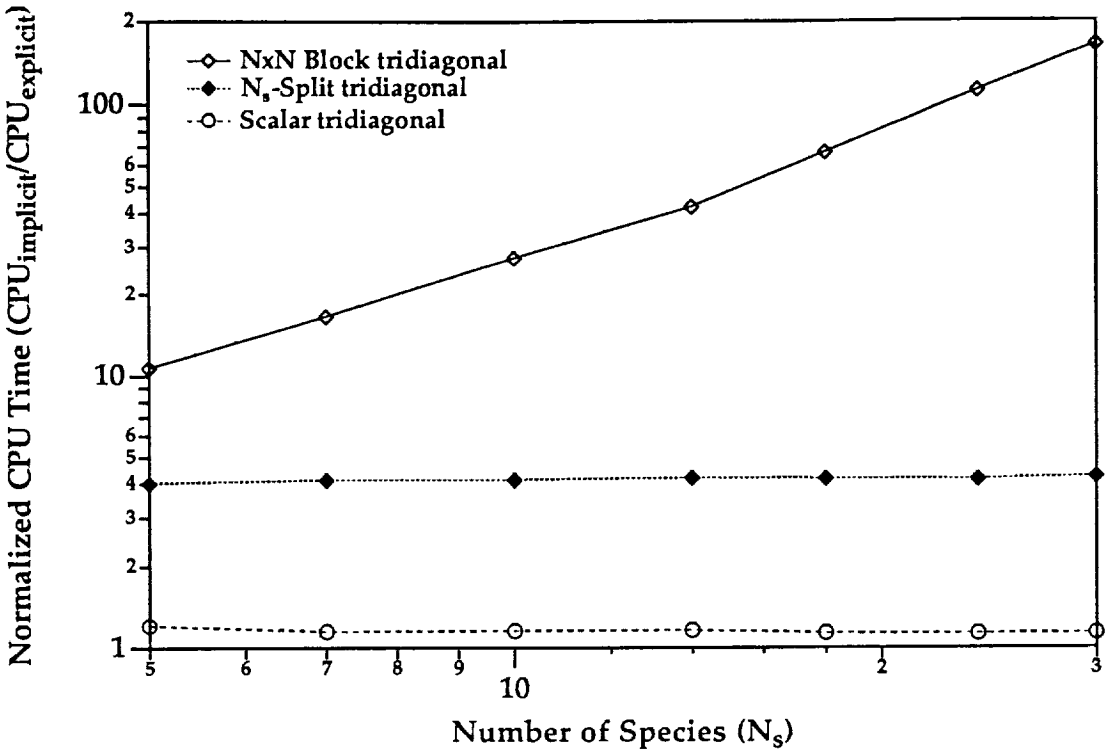

Figure 1-a. Normalized CPU requirement for Block, Scalar and N_s-Split methods (nonreacting). CPU is obtained as time per iteration per grid point, and normalized to CPU requirement for explicit method.

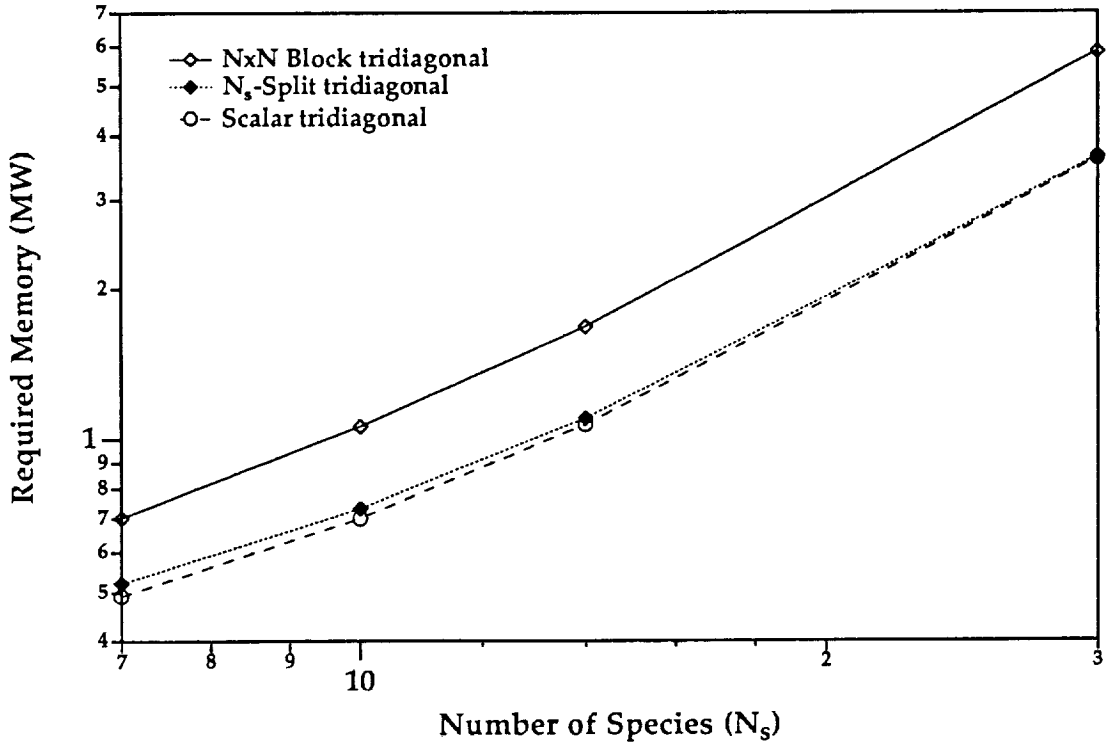

Figure 1-b. Memory requirement versus number of species for same methods

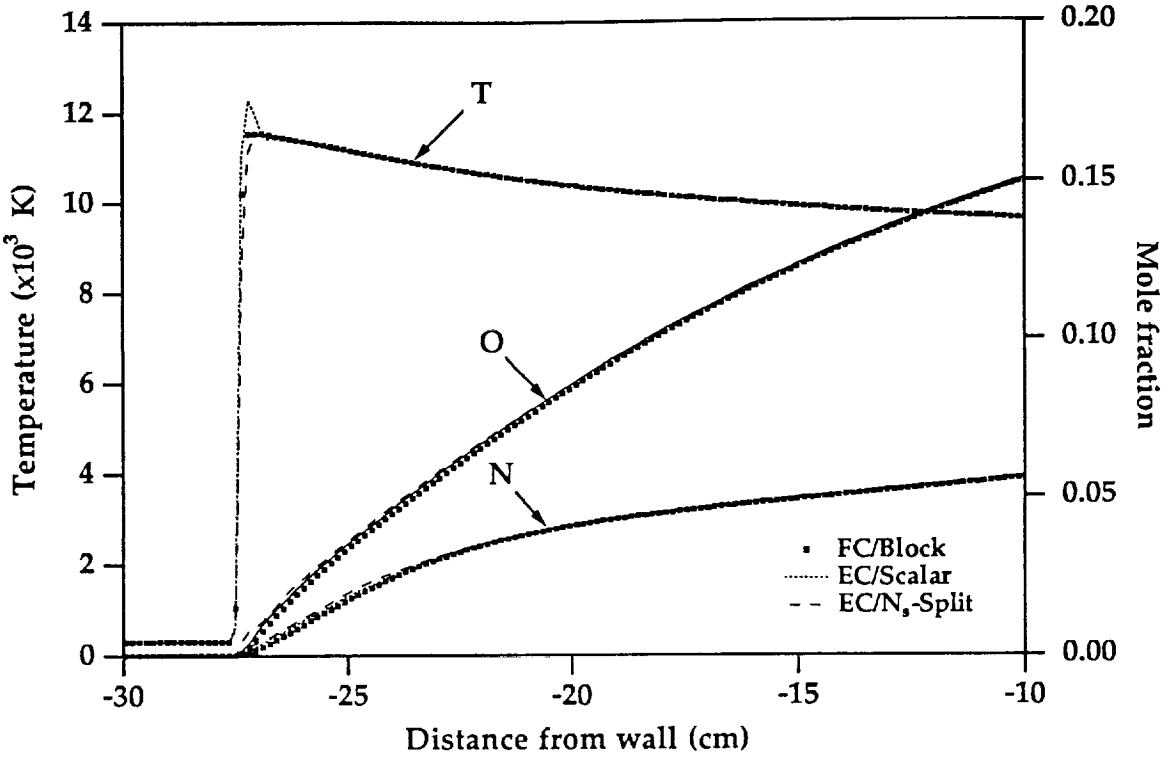

Figure 2-a. 1-D Shock (Case 1, $P_\infty=10^{-5}$ atm). Results for CFL=2. Results for EC/Block and OS/Block methods were indistinguishable from FC/Block method and hence, are not shown.

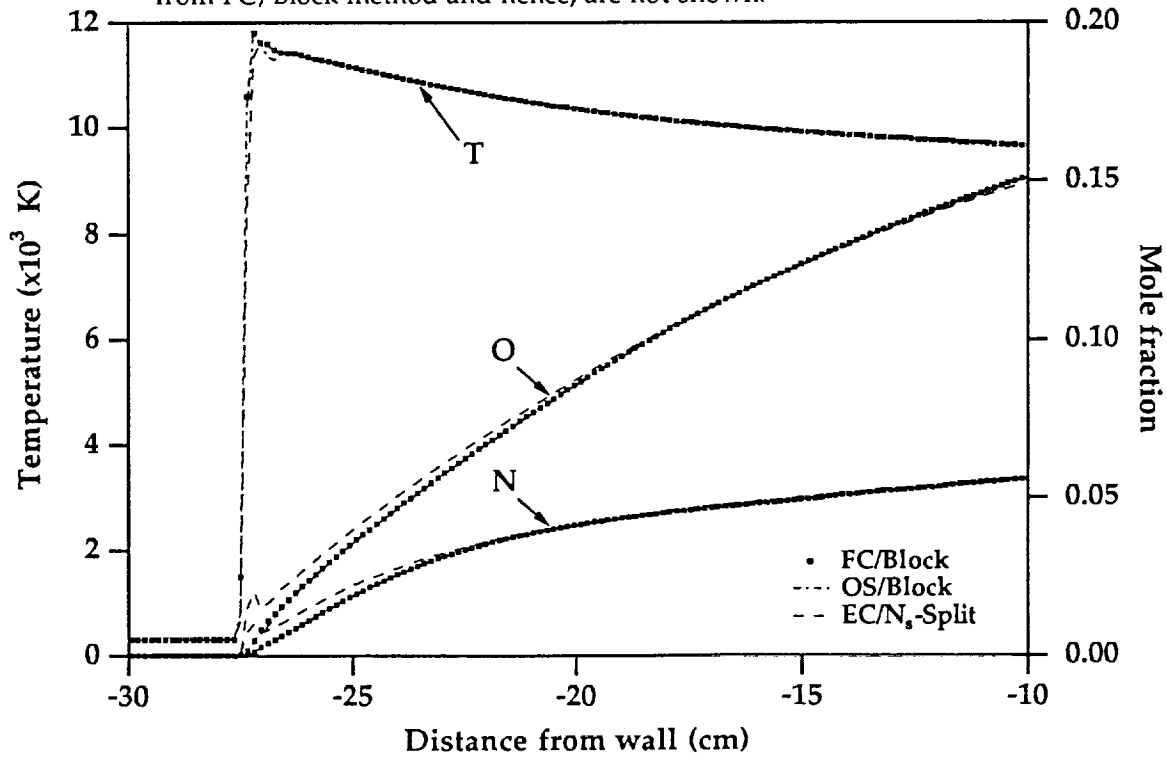

Figure 2-b. 1-D Shock (Case 1, $P_\infty=10^{-5}$ atm.). Results for CFL=4. The EC/Scalar method failed for this CFL number.

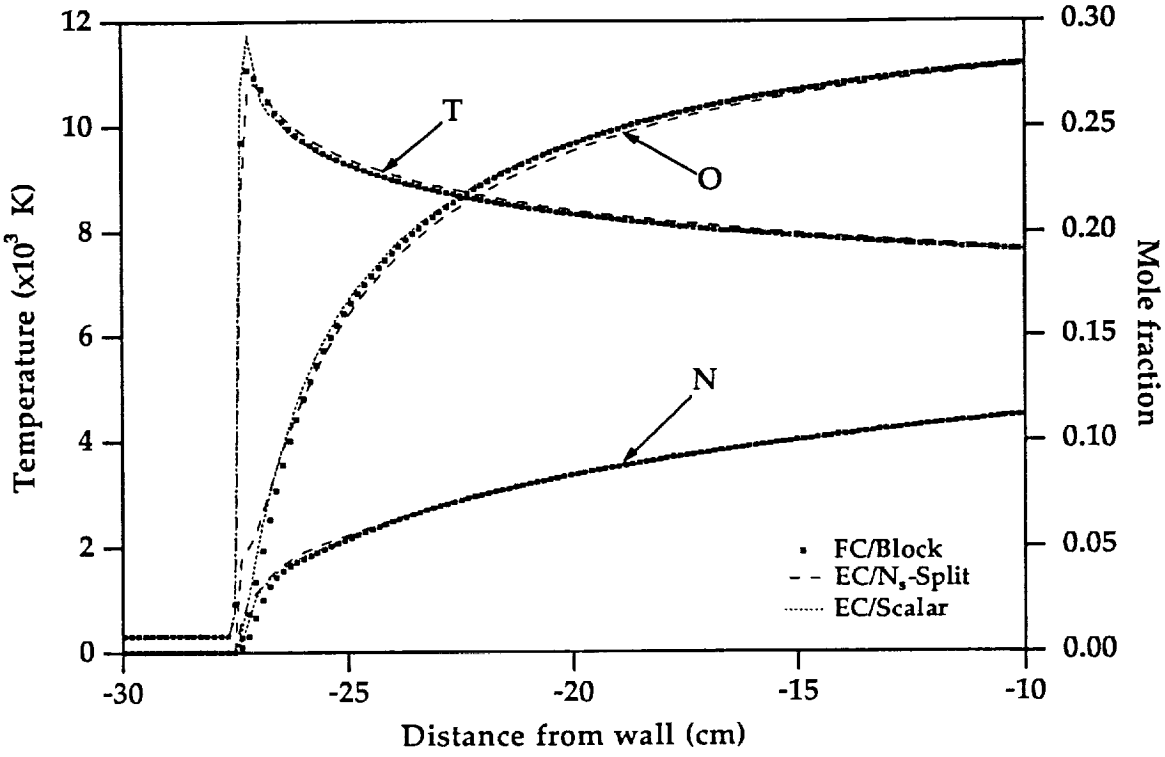

Figure 3-a. 1-D Shock (Case 2, $P_\infty=10^{-4}$ atm.). Results for CFL=2. Results of EC/Block and OS/Block methods are indistinguishable from FC/Block results and hence, are not shown.

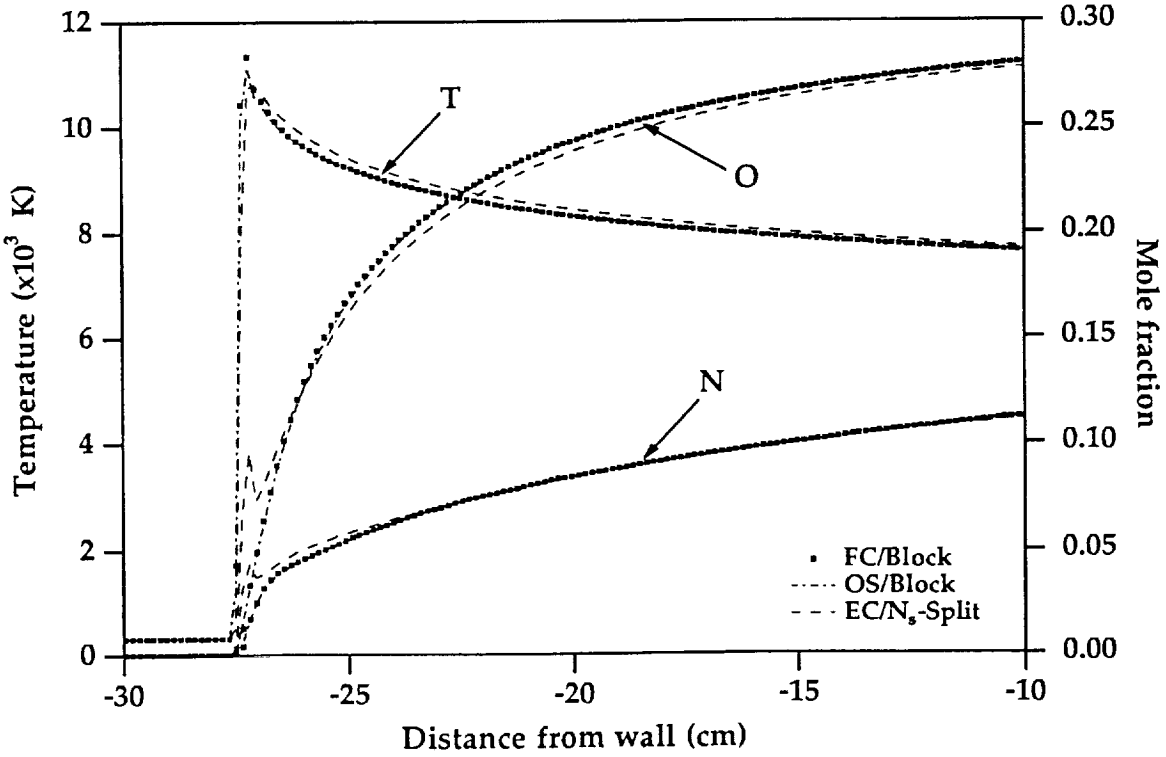

Figure 3-b. 1-D Shock (Case 2, $P_\infty=10^{-4}$ atm.). Results for CFL=4. The EC/Scalar method failed for this case.

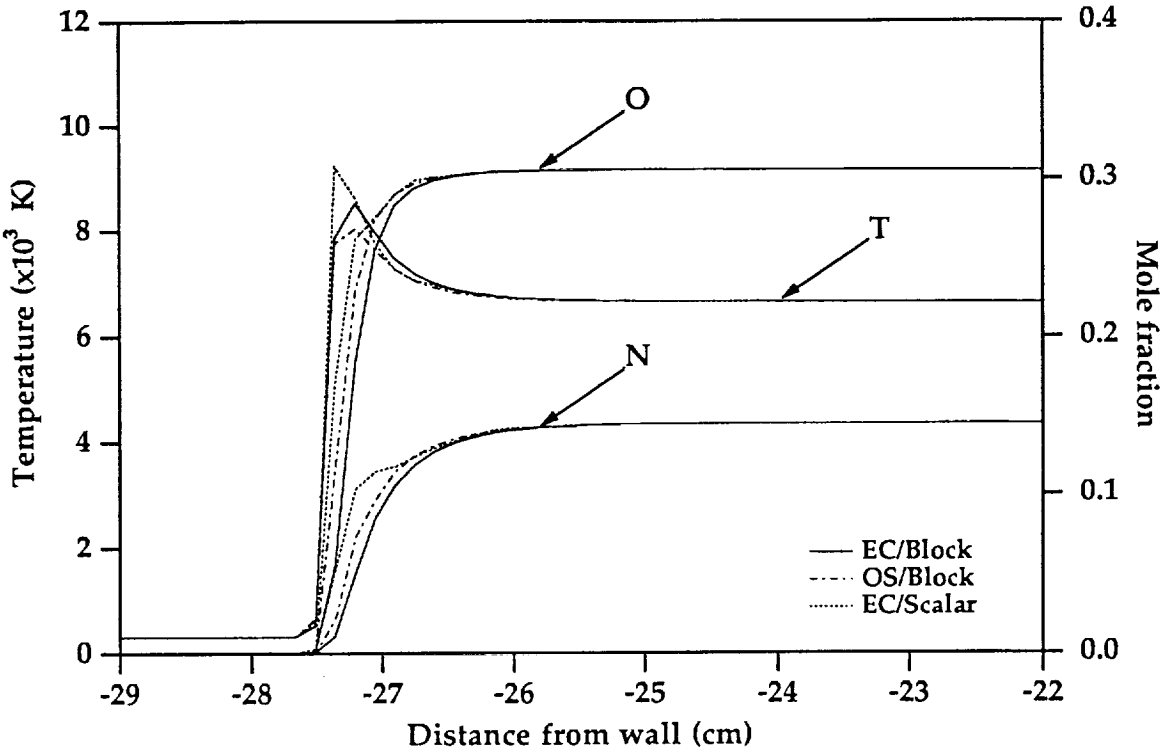

Figure 4-a. 1-D Shock (Case 3, $P_\infty=10^{-2}$ atm.). Results for CFL=2. The FC/Block method failed and the EC/N_s-Split method gave nonphysical, oscillatory solution.

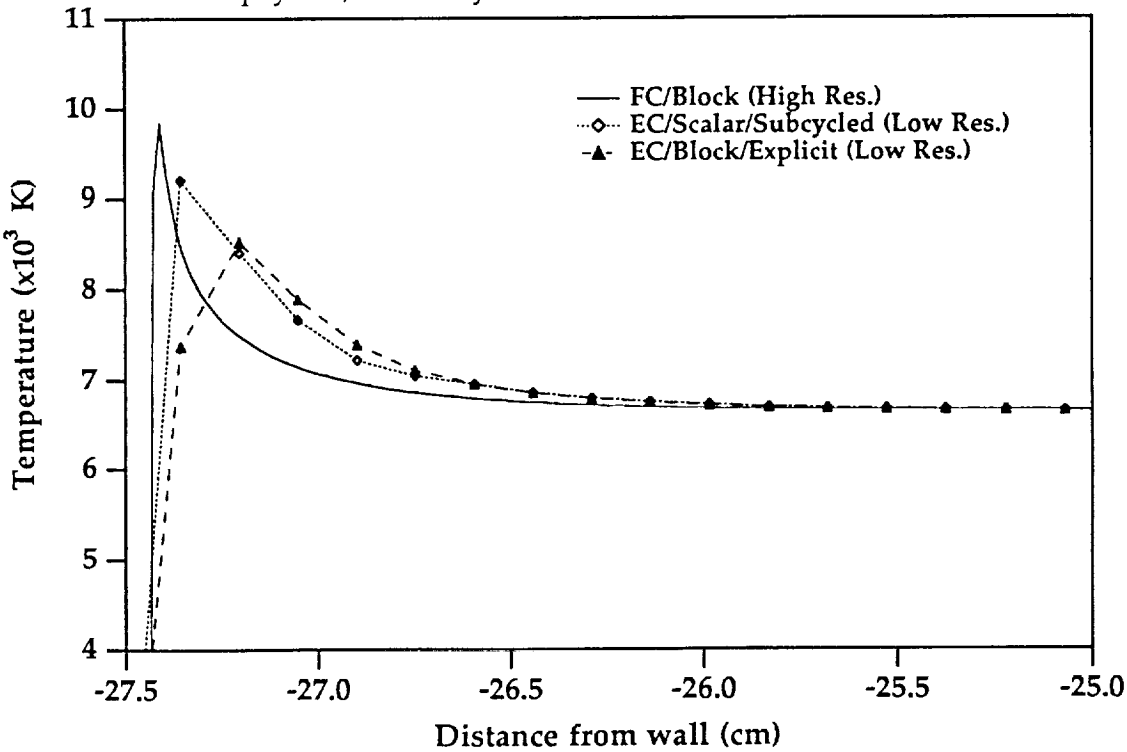

Figure 4-b. Details of Case 3. FC/Block solution is obtained for a higher density (x 10) grid. Other solutions shown are for the standard grid but with subcycled chemistry or smaller time steps (CFL=0.2)

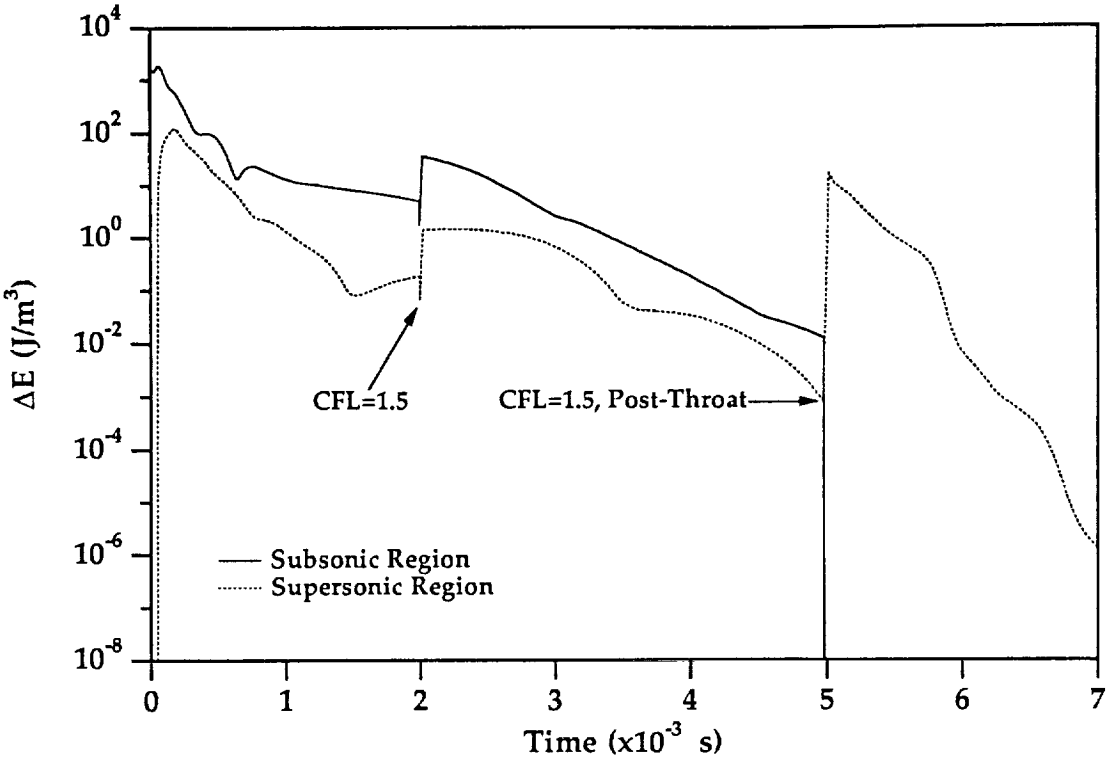

Figure 5-a. Quasi-1D Nozzle - energy residual history for the FC/Block method.

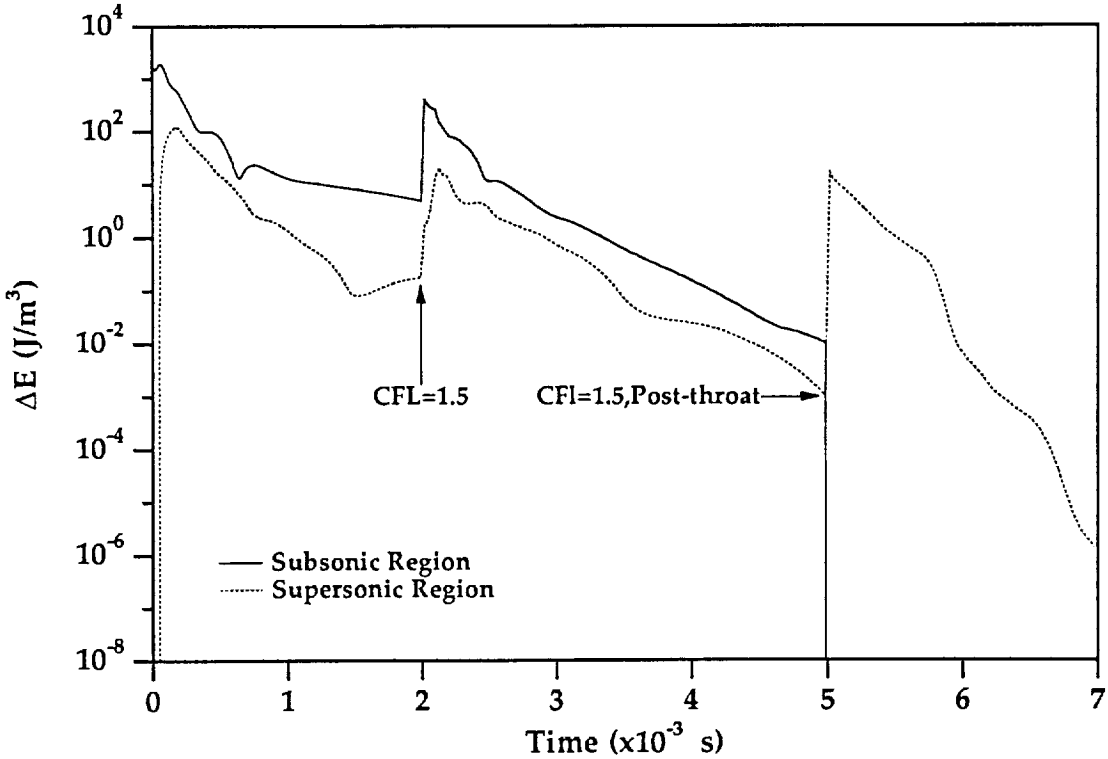

Figure 5-b. Quasi-1D Nozzle - energy residual history for the EC/Block method.

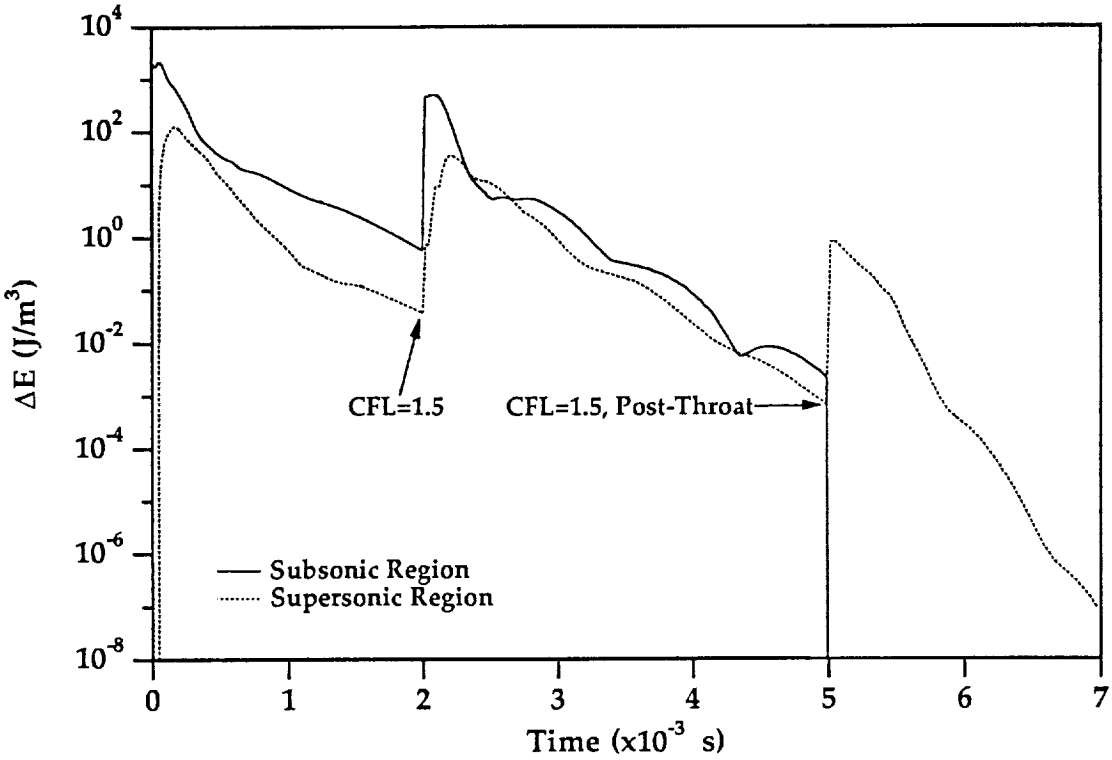

Figure 5-c. Quasi-1D Nozzle - energy residual history for EC/N_s-Split method.

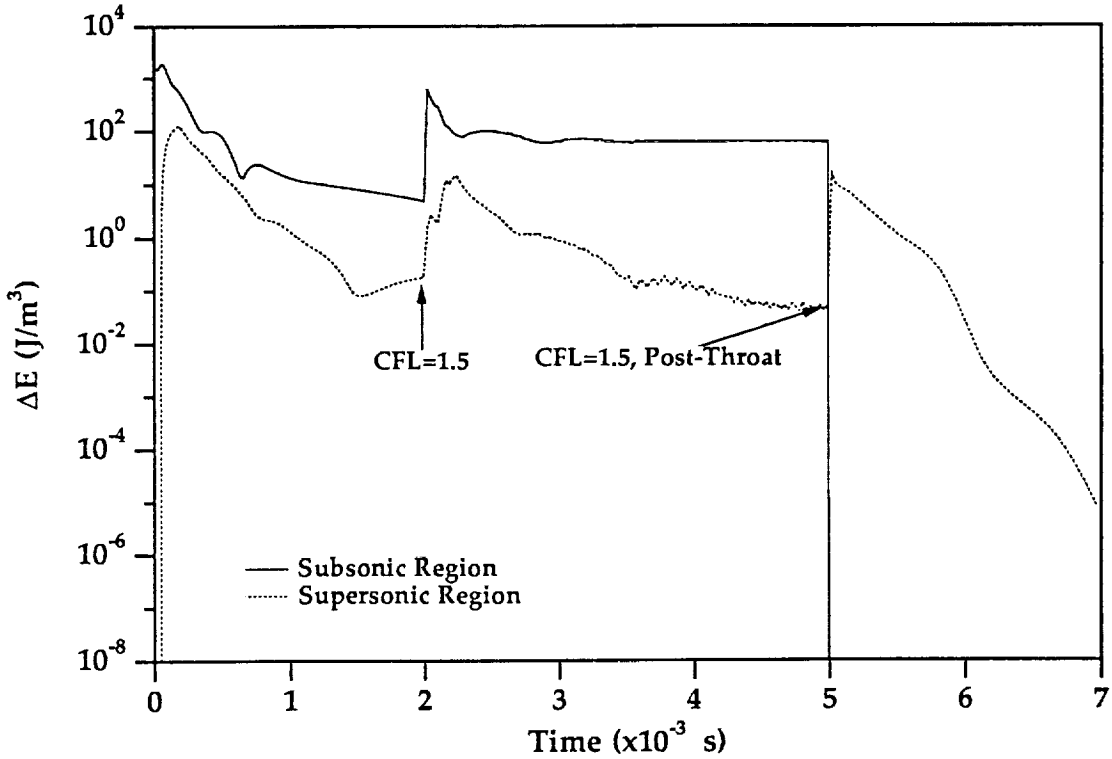

Figure 5-d. Quasi-1D Nozzle - energy residual history for EC/Scalar method.

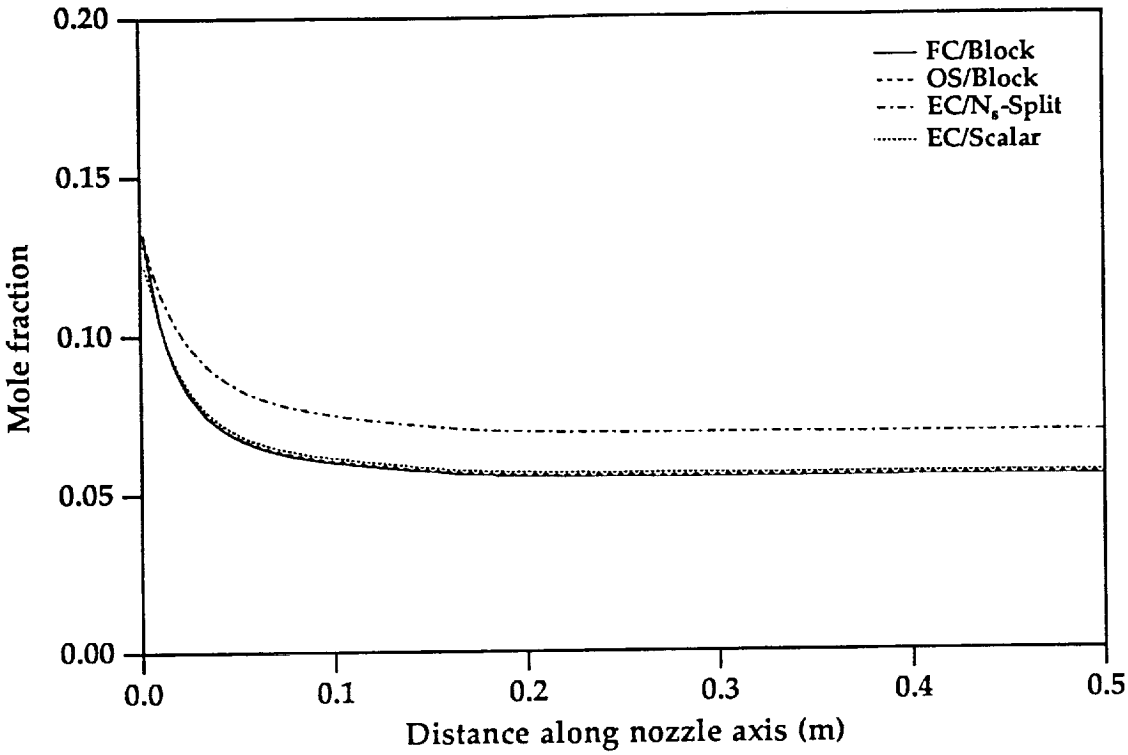

Figure 6. Quasi-1D Nozzle - steady state axial distribution of atomic oxygen.

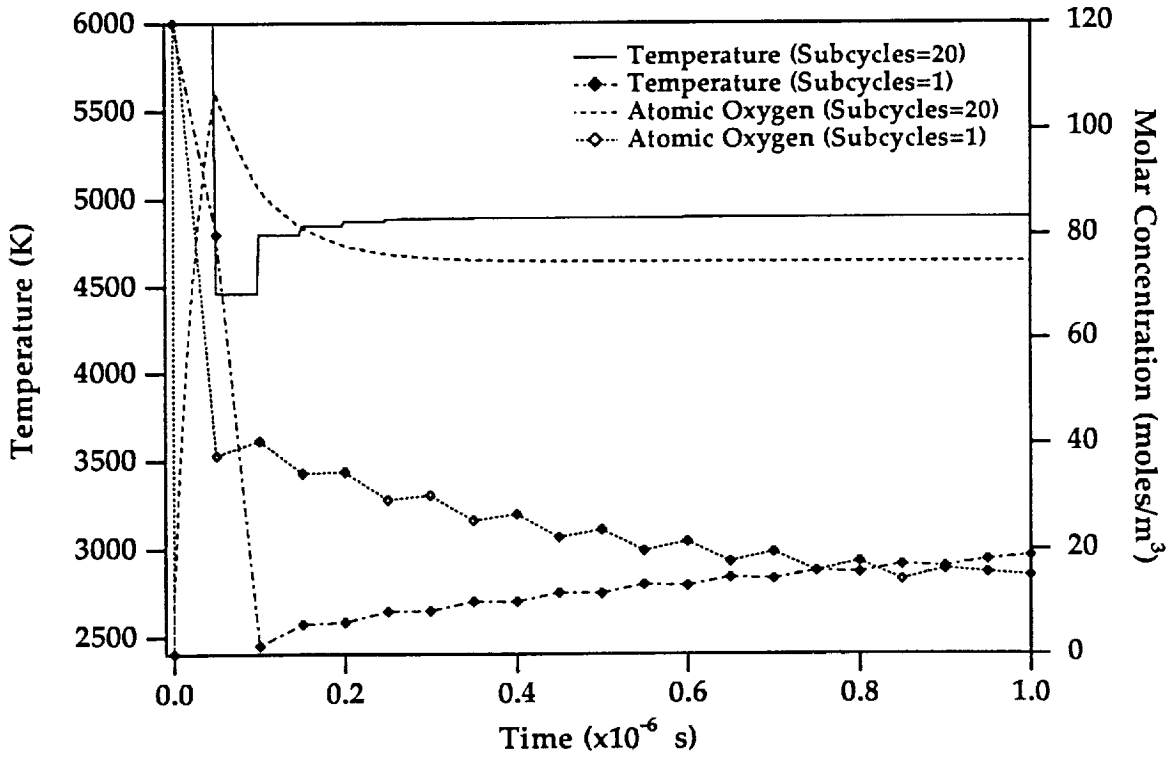

Figure 7. Quasi-1D Nozzle - Test of subiterated chemistry (EC/Block method). Initial state far from equilibrium and global time step (Δt) is 50 ns. Subcycled case (20 cycles) has an effective time step (δt) of 2.5 ns. The temperature is recomputed only at the end of the integration over the global time step 50 ns.

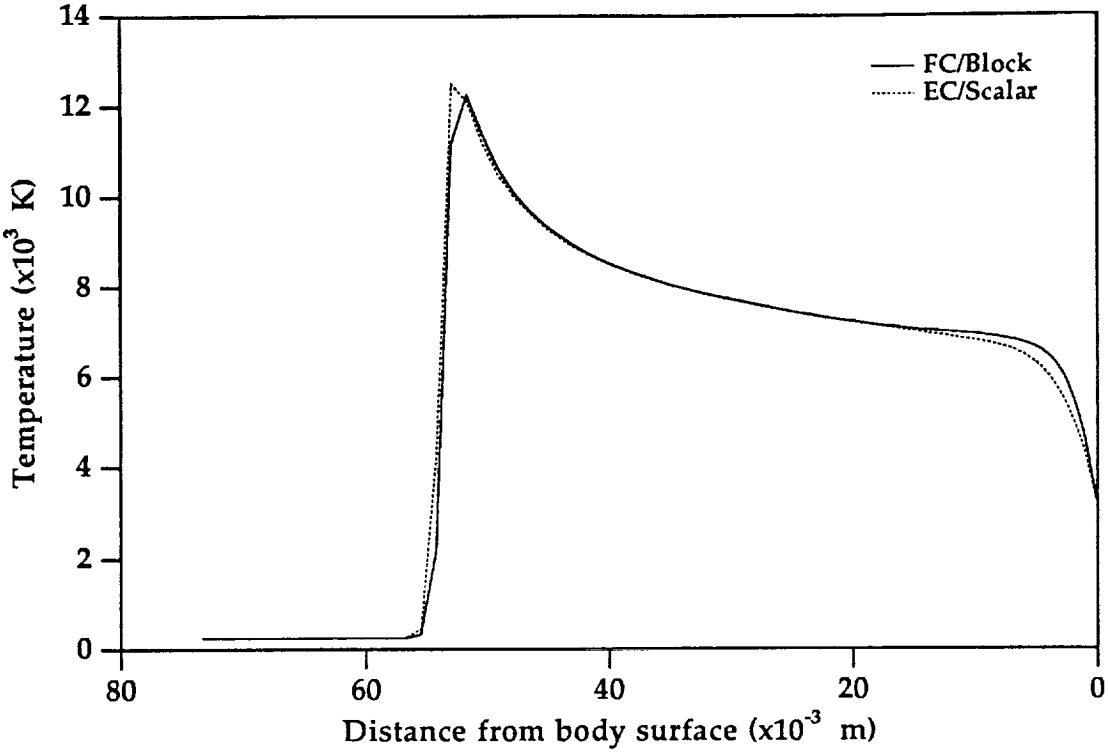

Figure 8-a. Axisymmetric Blunt Body - Temperature profile along the stagnation line (non-adapted grid).

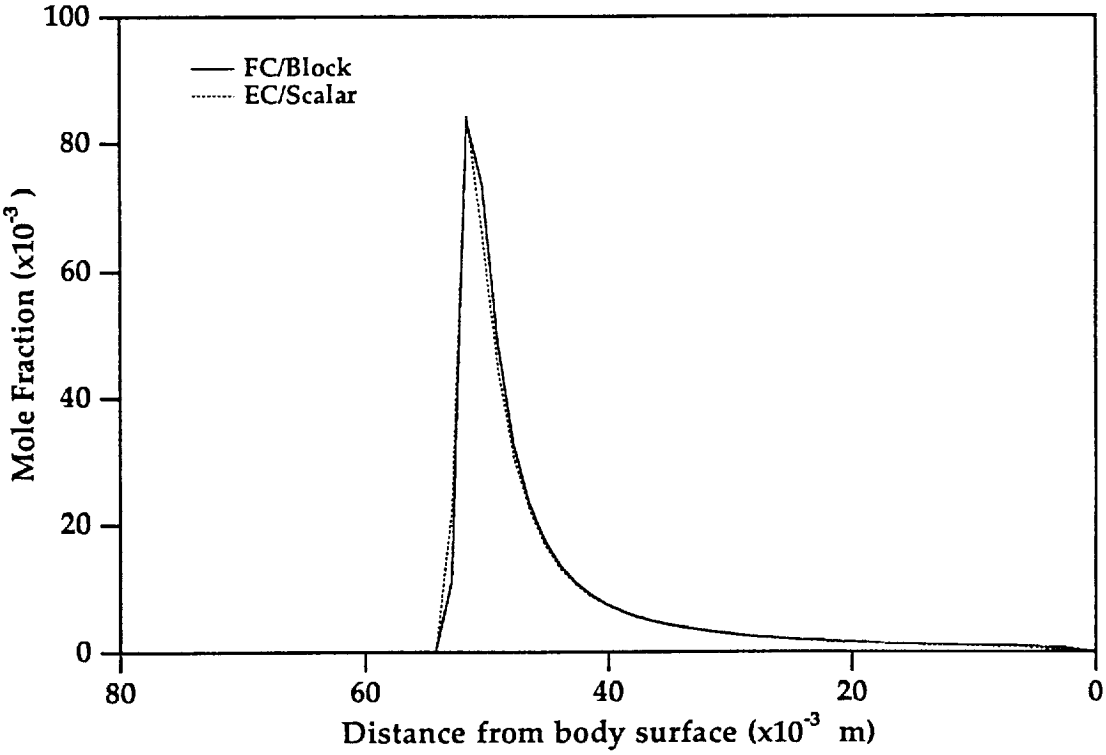

Figure 8-b. Axisymmetric Blunt Body - Electron mole fraction profile along the stagnation line (non-adapted grid).

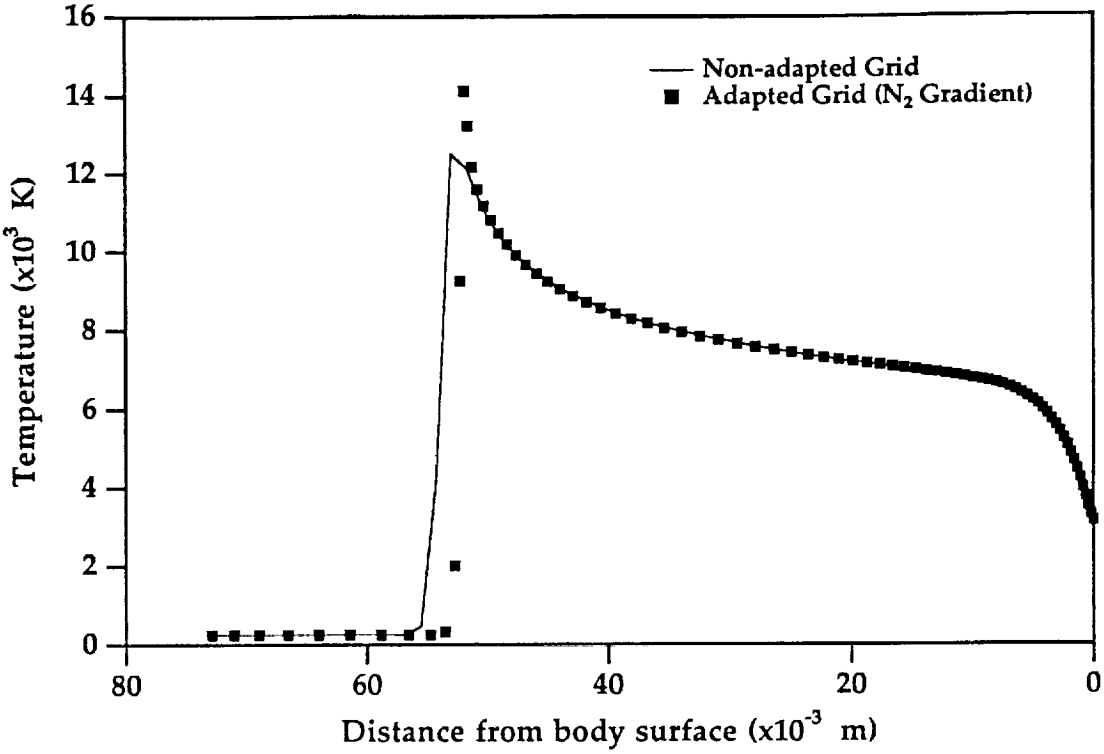

Figure 9-a. Axisymmetric Blunt Body - Temperature profile along the stagnation line for non-adapted and adapted (final pass) grid. Note the significant change in shock location and peak temperature.

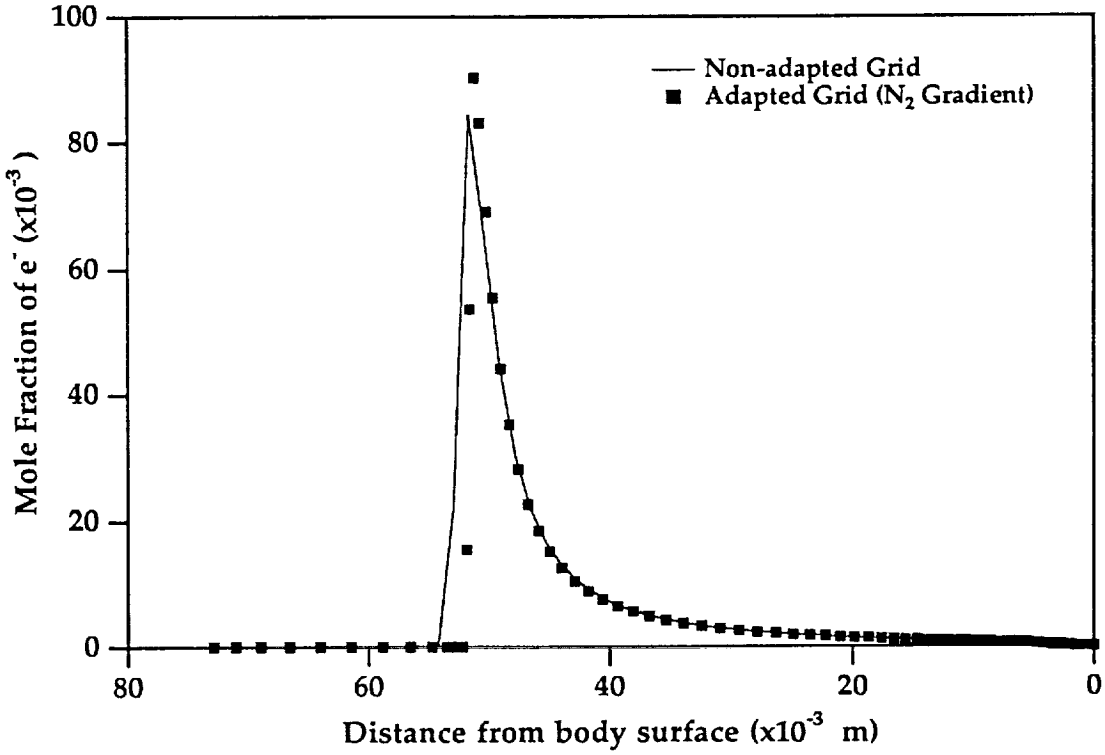

Figure 9-b. Axisymmetric Blunt Body - Electron mole fraction profile along stagnation line for non-adapted and adapted (final pass) grids.

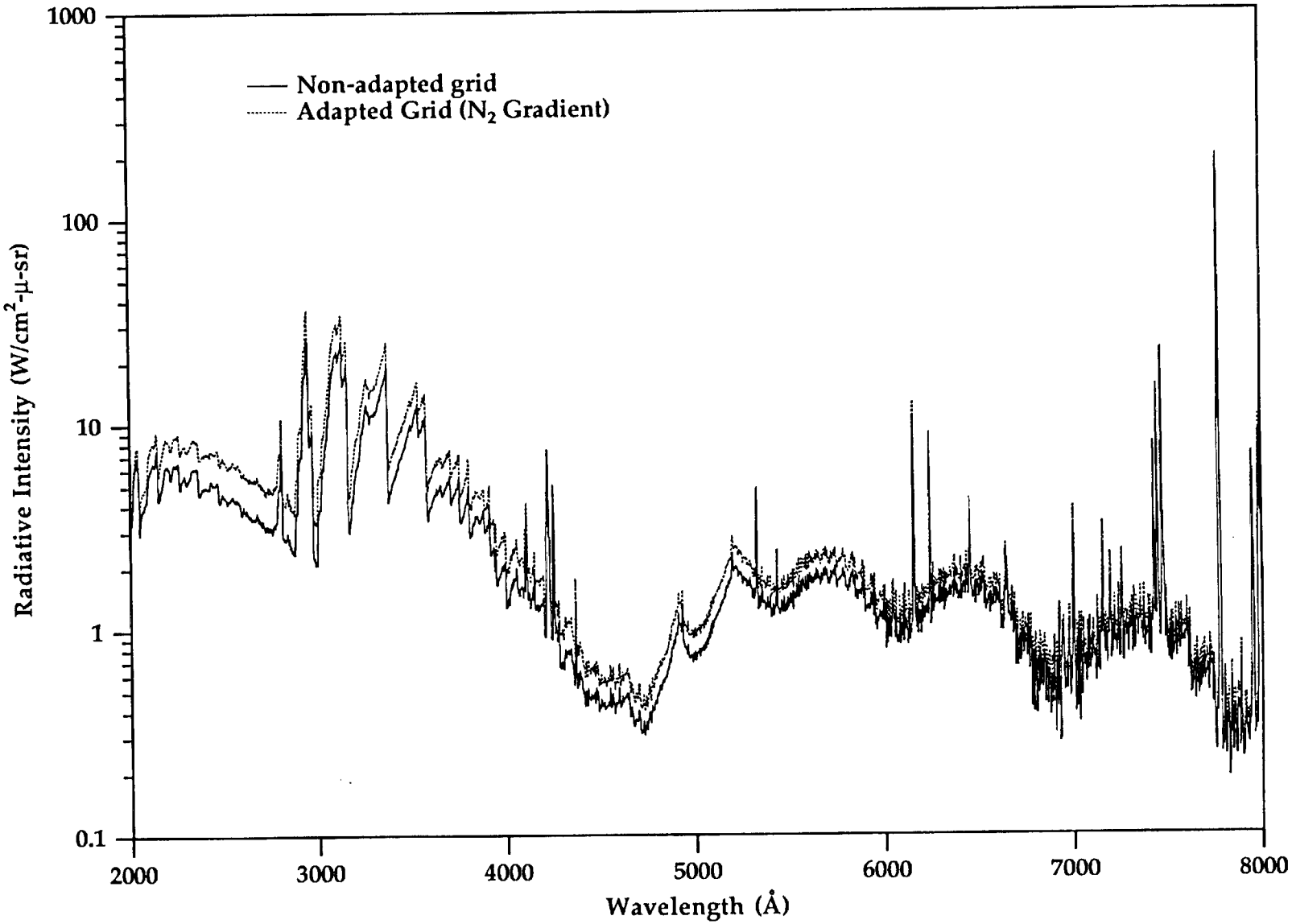

Figure 10. Axisymmetric Blunt Body - Comparison of radiation spectra incident on the wall (stagnation line of sight). The change is ≈ 35% in the UV(2500 Å) region.

AIAA-92-4029

NUMERICAL SIMULATIONS OF UNSTEADY FLOW IN A HYPERSONIC SHOCK TUNNEL FACILITY

Jean-Luc Cambier, Susan Tokarcik
and Dinesh K. Prabhu
Eloret Institute
Palo Alto, CA

AIAA 17th
Aerospace
Ground Testing Conference
July 6-8, 1992 / Nashville, TN

NUMERICAL SIMULATION OF UNSTEADY FLOW IN A HYPERSONIC SHOCK TUNNEL FACILITY.

Jean-Luc Cambier *, Susan Tokarcik †, Dinesh K. Prabhu ‡
Eloret Institute, 3788 Fabian Way, Palo Alto, California 94303

Abstract:

This paper describes the computational work being performed at Ames on the simulation of the 16" Shock Tunnel facility. The paper describes the approach used and shows some preliminary results for various flow transients. In particular, we describe the numerical problems encountered during the computation of these flows, and the methods used to resolve them. We also discuss the validity of some approximations used, notably concerning the reduction of the problem into problems of smaller dimensionality, or smaller size. We show how quasi-1D simulations can be used to help design experiments, or to better understanding the characteristics of the facility. An application to the design of a non-intrusive diagnostic is shown. The multi-dimensional flow transients computed include the shock reflection at the end of the driven tube, the shock propagation down the nozzle, and the breaking of the main diaphragm. The interaction between separate flow events will also be discussed.

I. Introduction

The Ames 16" facility, shown schematically in Figure 1, can be considered as a typical example of a shock-tunnel for hypersonic flows. The shock tunnel is about 70 meters long, composed of a driver section (17" diameter) filled with a light combustible mixture, and a long driven tube (filled with the test gas at low pressure). At the end of the tunnel is a supersonic nozzle 6 meters long (1 m diameter at the exit plane) and finally a test section. The complete operation of the facility typically results in test times of the order of 5 to 20 milliseconds: the time for the main shock to propagate from the main diaphragm to the end of the driven tube is of the order of 7 msec. After partial reflection at the end of the driven tube, the shock interacts with the incoming contact discontinuity (CD) which separates the test gas from the driver gas. For 'tailored' conditions, there is no wave reflected back from this interaction, and the flow between the CD and the nozzle is uniform and steady. More detailed descriptions of a shock tunnel operation can be found for example in ref. [1]. The test time is measured from the time the flow conditions in the stagnation region become steady, until the CD reaches the end of the driven tube, and the nozzle flow becomes contaminated with the driver gas. A flow 'quality' will be represented by the steadiness of the stagnated flow, the low level of contamination of the test gas by driver gas or impurities, as well as the peak conditions (pressure, enthalpy) attainable by the facility.

Numerical simulations are required to better understand the test flow conditions (temperature, mass fraction profiles, time dependence, etc..) and supplement the experimental knowledge: they are used also to improve the design of the experiments or to improve the tunnel operation characteristics. In order to satisfy these objectives, several aspects of the tunnel operation need to be simulated. Modeling the entire facility from the driver to the test section requires us to grid a physical length of about 50 meters; yet, important flow features such as shock and contact discontinuities (CD) should be resolved with good accuracy, i.e. a few mm in the axial direction. The spatial stiffness is then of the order of 10^4; this is a conservative estimate, since the boundary layers also need to be resolved in some cases, requiring grid spacing as low as tens of micrometers in the radial direction. The modeling of the shock-tunnel facility falls into the general category of *multiple scale* problems, and calls for appropriate special numerical methods which we will hint at in this paper.

The complete operation of the hypersonic facility also involves a large number of different physical processes at work, some of which are not well understood or are very difficult to compute. The combustion process in the driver gas requires a good description

*Senior Research Scientist, member AIAA. Mailing address: NASA Ames Research Center, MS 230-2, Moffett Field, California 94035.
†Research Scientist, member AIAA.
‡Research Scientist, member AIAA.

of the energy deposition and flame propagation; the main diaphragm rupture would require us to understand the material deformation up to the plasticity limit. The penetration of the jet of driver gas into the driven tube is a problem of 3D, turbulent, multiscale mixing. The temperatures are sufficiently high that some wall ablation takes place and contaminates the flow. Finally, radiative effects may need to be considered, and low density, thermal nonequilibrium gas models may be required in the nozzle expansion. A multiplicity of CFD tools must therefore be made available to study the effects of each of these phenomena.

The problem is compounded by the lack of crucial experimental data: such phenomena such as diaphragm rupture are difficult to observe, and only rough estimates of the process time and energy scales can be made available and approximately correlated with the experimental data. Ablation of the tunnel material is also a very complex physical process, which may depend on the microstructure of the material itself.

Solving this problem will require us to develop and test appropriate numerical techniques, decompose and reduce the problem accordingly, and develop and test various physical models. Simplification of the problem can be accomplished first by 'dimensional reduction', i.e. solving the problem in in a reduced number of dimensions. Quasi-1D simulations have low computational time and memory requirements, and therefore can be used for a large number of computations, such as those required for design and sensitivity studies. It will be important to verify the accuracy of these simulations, and to estimate the quality of information which can be obtained from them.

In a typical cartesian tradition, decomposition of the problem into several independent sections is usually attempted. This we regard as 'causality reduction'. This approach requires several approximations and simplifications, and its validity needs to be more clearly justified. For example, the time evolution of the flow in the test section clearly requires us to accurately compute the unsteady flow in the stagnation region, including gas/wall interactions, shock/boundary layer interactions. The shock/CD interaction is also very important, and this requires us to know very well the shape of the CD. Going back further, the shape of the CD will be influenced by the earlier process of flow establishment from the main diaphragm rupture and thereon. But the details of the diaphragm rupture will depend on the pressure rise in the driver gas, and this requires us to model first the turbulent flame propagation in the driver tube. The logical sequence of events, i.e. from driver tube combustion to flow expansion into the test chamber, is unfortunately the most difficult to compute, since it requires us to be able to model the most complex phenomena at first. Therefore we have to sacrifice some degree of detail in order to obtain practical answers in reasonable time. By causally reducing the problem, we loose accuracy but gain in efficiency: the method can still be used to examine the important physical effects (i.e. sensitivity studies) in an efficient way.

In this paper, we will discuss these methods and the preliminary results. The following questions must be addressed:

- what improvements in numerical techniques are required.
- how accurate are the results from reduced (1D) models.
- how significant are the causal influences of various sections of the tunnel.
- what physical phenomena are important and how to model them.

The last item on our list will not be discussed here. In this paper, we will concern ourselves primarily with the numerical techniques, and the evaluation of the approximations commonly made in shock-tunnel simulation. The obvious intent of the development of this numerical capability is to provide an array of numerical tools for better understanding of the facility operation, and the design of new test conditions and diagnostic procedures. The combined focus of both experimental and numerical tools leads to superior measurement capability, and is an approach practiced at NASA-Ames [2].

II. Numerical Techniques

We have already mentioned that the spatial and time stiffness can be quite large; fortunately the CFD community has developed an arsenal of techniques which can potentially be used to reduce the severity of the problem. First, we observe that the flow discontinuities are few and generally well localized: it is therefore unnecessary to simultaneously carry the same resolution requirements in all regions of the facility. We can rely on several techniques of dynamical

grid refinement to carry this task. Second, the problem can be approximately separated in three parts. The combustion process in the driver gas proceeds independently of the driven tube, and can be computed separately if necessary (throughout this paper, it will be simply modeled). Since the flow is mostly supersonic in the nozzle, there is no backward influence of the flow from the nozzle to the tubes. It is therefore adequate to compute at first the unsteady flow in the driver and driven sections, including the nozzle and up to the throat; the flow solution at the exit plane can be stored according to the required spatial and time accuracy, and used as unsteady inflow condition for the remainder of the facility, i.e. nozzle and test section. This allows us also to switch between different physical models (e.g. nonequilibrium thermodynamics) and different dimensionalities (3D versus 2D axi-symmetric or 2D versus 1D).

Another important question concerns the choice of numerical method: although we are interested in the unsteady flow motion, the flow time scales that need to be resolved may be large compared to the time scale from the stability limit of an explicit scheme. This is true especially for a clustered viscous grid. An implicit method, if time-accurate, can potentially be used for this problem as well. However, there is a huge cost associated with the inversion of the block-tridiagonal matrices from the LHS of the system of equations, especially when multiple species are present. Our experience showed that even when only two species are considered (driver gas/driven gas), the implicit method needs to be executed at a CFL number ≥ 5 for better performance than the explicit method. Due to the severe nature of the problem (pressure ratio, shock speed), this CFL value is generally too large for these transient flows. However, the viscous terms alone can be treated implicitely, and show greater stability than the convective terms: our method therefore performs an Operator Splitting between convection, viscous dissipation and chemistry. The viscous terms are treated implicitely, and the inversion of the 3×3 (in 2D) block tridiagonal matrices is sufficiently fast to be justified. The chemistry is also treated point-implicitely, and the algorithm is also very fast. When the chemistry is extremely stiff however, linearization errors will reduce the stability of the point-implicit algorithm. For example, let us consider air (79% N_2, 21% O_2) suddenly raised to 100 atm and 6000 °K: at constant volume, the system reaches equilibrium within a fraction of a microsecond. Attempting to solve implicitely the chemistry in one iteration and with a time step larger than $\simeq 2\ 10^{-8}$ sec would lead to very unstable and unphysical solutions. The initial evolution from the highly nonequilibrium state needs to be time-resolved more accurately: our algorithm subiterates (more precisely, 'sub-cycles') the chemistry, i.e. integrates over a given time interval Δt with variable steps δt. The sub-step is initially estimated from the rate of change of the species, then is stretched in a fixed proportion for the subsequent sub-iterations: $\delta t^{n+1} = (1 + a)\delta t^n$, with $a \geq 0$. Each sub-iteration is solved point-implicitely. The change in temperature is also estimated at each sub-iteration from the change in chemical energy. Figure 2 shows a sample computation ($a = 0.5$) for this highly nonequilibrium case. The 'exact' time evolution is also shown. The integration intervals are $\Delta t = 5\ 10^{-7}$ seconds. One can see that the variable step solution is off in the equilibrium region until the end of the first integration interval, at which time the thermodynamic state of the gas is re-analyzed and a more accurate calculation of the temperature is performed. The sub-iterated solution then quickly matches the exact solution.

To maintain good accuracy, the relative changes in temperature estimated during the chemistry should be limited. A chemical time scale is therefore defined as the time during which the chemical reactions induce a relative change in temperature of $\simeq 5\%$[†] . The effect of chemistry on the flow dynamics occurs principally through the temperature change, and this time step limit provides us with a criterion for accurate coupling of the chemistry and flow dynamics. If there is no monitoring of the chemical time scale and no enforcement of this time step limit, an instability generally develops rapidly, especially in cases of stiff chemistry; this instability can occur for both a fully-coupled approach or the Operator-Splitting approach. The case of very stiff chemistry would seem therefore to be very inefficient: this corresponds basically to a very poor resolution of the chemical relaxation distance, such as the one behind the primary shock. However, it is possible to somewhat rescale the chemical time scale without changing the solution too much. Let us suppose that we want to resolve the flow dynamics on the order of a convective time-scale Δt_{conv}, but the chemistry is so stiff that accuracy and stability considerations restrict us to (for example) a global time scale $\simeq 0.01 \Delta t_{conv}$. We can artificially rescale the chemistry by 10, and the stability limits lead us

[†]This number may be varied, according to the desired accuracy and/or the stability. It is our experience that in most cases, the maximum relative change allowed should be less than 10%.

to a time scale $0.1\Delta t_{conv}$, which we can better afford. This rescaling can be done locally, depending on the stiffness ratio: this will affect slightly the solution, for example by over-estimating the chemical relaxation length behind a shock, but the difference may be practically insignificant for very stiff cases. The technique is easily implemented by restricting the integration interval (it becomes $5\ 10^{-8}$ sec in our example): the insert in Figure 1 shows the results of this rescaling approach. We see that the original transients are still reproduced, and the solution still converge to the exact solution. This sub-iterated algorithm, with or without the rescaling option, is used in all our calculations.

The spatial stiffness can be solved by various techniques of dynamic grid adaption. In the driver tube, strong gradients and discontinuities exist only during the combustion process. After rupture of the main diaphragm, only weak gradients subside, and this section of the facility does not require high resolution. The spatial accuracy is required for the propagating shock and CD, down the driven tube. One possible technique is to dynamically compress and stretch the grid points to accumulate them in the required regions. This technique can work well in one dimension and is easy to implement: care must be taken however to prevent sudden jumps in spacings, or accuracy will be lost. The technique may become more problematic in two or more dimensions, as some flow features (including the CD) may have more complex shapes: the grid can become distorted, and can affect the solution. Another technique, pioneered by a group at Livermore [3], consists of adding smaller scale grids in regions of interest. These grids can be exact sub-scale replicas of some regions of the coarse, background grid: the flow variables can be transferred between grids in an exactly conservative way. This way, the grids are never distorted and their motion can be computed very quickly, with minimal overhead. An example is shown in Figure 3: the propagation of the primary shock and CD down the driven tube is computed in a one-dimensional model. A first calculation used a constant spacing grid, with about 1000 points for the whole tunnel. A second calculation used a background grid for the whole tunnel with 250 points, and a high resolution grid super-imposed on it: the latter moves along with the shock, with a sliding motion. The sub-scaled grid had a size of 800 grid points, and the scale ratio between the two grids was 20 to 1. Flow values within the background cells are computed by volume averaging of the sub-scaled cells present, if any. While both calculations used approximately the same number of points, it is clear that the second method has a much higher local resolution, and the sharpness of the CD is dramatically improved.

Another method, which we will be testing in the future, uses non conservation of the number of grid points. Unstructured grids can be manipulated to accumulate points in the regions of interest, either by grid displacement or by dynamic subdivision.

The singular axis was found to be another recurrent problem during the computation of flow transients: the simulation of the shock reflection at the end of the driven tube, for example, initially showed a strong conical shock structure near the axis with the apex of the cone leading the overall structure (see Figure 4). This peculiar formation can also be seen for example in the results of P. Jacobs [4]. This structure is possible only if a very intense and high velocity jet of gas is produced and maintained on the axis: this is a highly singular and unphysical behaviour. Close examination of the numerical results indeed showed an excessively large axial velocity component in a single cell close to the axis. Because this high velocity jet was present in one cell only, and did not show signs of diffusion, we were convinced that it is the result of a numerical error. A similar phenomenon can be observed also in the propagation of the main shock down the nozzle [5], and can be seen at the axis or in some cases near the walls. This phenomenon was observed only for axi-symmetric flows, and when a second-order accurate scheme (with minimal dispersion) was used. It was finally related to the aspect ratio of the grid cells: indeed, the problem disappeared when the aspect ratio of the grid cells was adjusted to lower the radial gradients. If the spacing is such that $\Delta x << \Delta r$, the flow features are smooth and accurate. If $\Delta x \geq \Delta r$ an instability *may* develop in some regions of the flow. We assume the problem comes from the axi-symmetric pressure correction term, which *is not* part of the monotonic (TVD) fluxes and acts as a non-conservative momentum source term. This pressure correction term is a result of the formulation of the Euler equations for an axi-symmetric problem, and can be easily visualized with the following finite-volume description. Let us consider a cell in a cylindrical geometry, described schematically in Figure 5. As one approaches the axis, the ratio of cell side surface to cell volume behaves as $1/\Delta x$ for the axial direction, while it is exactly 0 for the radial direction. There is a contribution to the radial momentum density from the pressure on the sides of the cells in the azimuthal direction. This contribution is proportional to $1/\Delta r$. It is

clear that when the cells are clustered near the axis, the contribution from the non-conservative momentum source term may become dominant, and therefore there is no guarantee that a non-oscillatory solution can still be obtained. The problem usually disappears when the grid is relatively coarse in the radial direction, near the axis, in which case the source term ceases to be the dominant contribution. This observation also applies to other cases, such as the computation of shock layers on blunt axi-symmetric bodies. In most unsteady cases or for steady flows, the radial gradients will be weak near the axis. One particular exception would be the propagation of a shock ring towards the axis: this is such the case in the reflection of the primary shock in the tunnel, from the upper section of the end wall. Figure 6 shows a time sequence for the same case as Figure 4, but for a grid coarsened near the axis: we see that the instability is effectively removed. A similar improvement can be obtained by reducing the spatial order of accuracy in that region.

The general effect of the grid structure or aspect ratio on the flow solution should never be underestimated, especially in the severe cases we are concerned with. Although we may see unstructured grids as a potentially useful tool for the flows of interest here, their effect on the flow solution will have to be carefully evaluated.

The flow expansion in the supersonic nozzle is one of the easier tasks to perform: the transient flow simulation is required to examine the steady flow establishment time in the test section, and to verify that the flow does not choke during that time. This is particularly relevant for large objects or for massive gas (fuel) injection. Since the nozzle is evacuated to very low pressure before the rupture of the secondary diaphragm, the flow propagating down the nozzle is preceded by a high velocity jet. The mean free path in that region can be quite large ($\simeq$ 3 mm for P = 100 milliTorr), and strictly speaking the Navier-Stokes equations cease to be valid in this low-density region prior to the shock. By attempting nevertheless to solve the flow dynamics with the Navier-Stokes equations, we are experiencing strong viscous effects which operate on a very short ($\simeq$ 10 pico-second) time scale. Although the viscous fluxes are computed implicitely, it is necessary for stability reasons to artificially reduce the strength of these viscous effects in that region. This is easily accomplished by using a numerical switch that effectively and smoothly removes the gradients on a scale smaller or comparable to the mean-free path during the calculation of the viscous fluxes. This switch will effectively reduce the spreading of the shock into the low density gas. The shock thickness will therefore be underestimated. The cutoff length scale can be adjusted arbitrarily: in Figure 7 we show the effect of the cutoff choice (0.1 versus 10 mean free paths) on the solution, for two cases of nozzle pressures. The change is dramatic for the first case (100 μTorr) and unnoticeable for the second (100 milliTorr). Nevertheless, for the latter case, which is also the case we will be using throughout the remainder, the viscous time scale is reduced by a factor of 5 by choosing the higher (10 m.f.p.) cutoff value.

Using all the modified techniques now at our disposition, we are able to sucessfully compute the transient flows in the nozzle and driven tunnel at the rupture of the secondary diaphragm (see Figure 6). Different grids were used for the driven tube and nozzle regions, and no subscaled grids were used for this particular case: both regions were coupled at each iteration. The results of the computation for the nozzle flow (Figure 8) are in good qualitative agreement with an experimental schlieren of a similar problem shown in Figure 9, taken from ref. [6]. Both show the curved leading shock, and a complex structure behind it, dominated by a Mach disk, itself supported by oblique shocks emanating from the nozzle walls. Although the initial conditions for these two flows are very different, the similarity between the two structures lead us to conclude that they are examples of a general pattern. Details of the conditions (pressures, geometry, etc..) may change the relative strength and position of the shocks, without modifying the overall configuration. A snaphost taken at later times would show that near the exit plane of the nozzle, the primary shock straightens out and becomes normal. If one was to perform an unsteady computation in the test chamber assuming a normal shock at the inflow, the calculation would be in error by leaving out the complex shock structure which propagates immediately behind the leading shock. This is shown for example in Figure 10, where a cone has been used as testing body.

III. Dimensional Reduction

When test times are large compared to the transients, it seems appropriate to compute the nozzle flow for the steady state, without having to perform the calculation time-accurately for tens of milliseconds. This allows us to use many numerical techniques to make this computation more efficient. We have done several such computations, solving for the

full Navier-Stokes equations, but for limited regions at a time. The computation proceeds on a subset of the whole nozzle grid, until convergence is obtained. The subset then moves further down the nozzle; the procedure is similar to the displacement of a 'window' along the flow direction. This procedure is half-way between a global calculation and the PNS method; although less efficient than the PNS method, it is more flexible and allows us to correctly treat embedded recirculation zones or other unexpected subsonic regions which may occur. It was observed that the convergence rate and the computation time are dominated by the chemistry in the boundary layer, and the downstream propagation of chemical changes in the low velocity sublayer. Although the calculation does not display severe instabilities such as may be the case for the transient flows, it is still desirable to coarsen the grid in the radial direction near the axis, to avoid spurious fluctuations in pressure.

The steady nozzle flow computations are usually done to obtain estimates of the flow conditions at the exit plane, in particular temperature, Mach number, pressure and species concentrations. Since it is generally assumed that the flow is nearly uniform at the exit plane, it seems that simple one-dimensional computations should be adequate. We have performed such computations using a quasi-1D version of our code, and compared the results. The effect of the boundary layer is expected to be the major contribution to any potential disagreements between the quasi-1D solution and the 2D axi-symmetric solution. This effect is taken into account by effectively modifying the nozzle profile and its area. By considering the inviscid core only, the quasi-1D method can approximately take into account the constricting effect of the boundary layer by assuming a new nozzle shape for which the effective radius is a constant fraction of the real nozzle radius. The dependence of some flow quantities on the effective nozzle area is shown in Figure 11. It is clearly apparent that the static pressure has the highest sensitivity to the effective nozzle area, and therefore to the boundary layer thickness. Temperature and species concentrations are less sensitive to the area variation, and additional uncertainties about the chemical rates or contaminants are likely to cloud the issues: the static pressure is therefore an important variable to measure at the nozzle exit. The comparison with the 2D axi-symmetric results is shown in Figure 12, where again the sensitivity of the static pressure is clearly demonstrated. The best agreement is obtained for an effective nozzle radius of 87% the real radius (i.e. a boundary layer thickness approximately 13% the nozzle radius). Notice also that the static pressure is the only variable that still displays significant radial fluctuations within the inviscid core, at the exit plane. A multi-point measurement of this variable is therefore doubly informative, as far as code validation is concerned. In Figure 13 we show the radial profile of Temperature and NO concentration at station code-named N3 (2.37 meters downstream of the throat) and the exit plane. All the species profiles are relatively unchanged between N3 and the nozzle exit, except atomic nitrogen N, which is present in very small amounts. Owing to the high reactivity of N, this result is not surprising: most of the chemistry is frozen before station N3, and this is especially true of NO. The temperature variation between N3 and the exit plane is therefore due to hydrodynamical effects only.

NO is a relatively important specie to measure (it effectively ties up a significant amount of oxygen and has a noticeable effect on ignition delays), and it can be done easily with a laser absorption method. A computational study of this diagnostic technique can also be done to help design the experiment. The computed high resolution spectrum of the $NO(\gamma)$ band system is shown in Figure 14, with and without the boundary layer. The intensity at peak absorption of the $(0,0)$ band changes by a factor of $\simeq 3$ when the boundary layer is removed. A precise measurement of the core flow must avoid the uncertainty caused by the boundary layer: this can be simply done by providing an optical wave guide that protects the beam from the boundary layer. Although this protrusion is likely to disrupt the flow, the effect may be small enough or irrelevant at the exit plane. We can now look at the effect of core flow variation by comparing the intensity for the 2D solution (without BL) and a quasi-1D solution. The result is plotted in Figure 15-a as the ratio of intensities between the two cases. Surprisingly, the error is less than 10% for the most sensitive lines. At the exit plane (Figure 15-b), the results are even better, with deviations less than 2%! This seems to indicate that this measurement can yield useful information on the core flow, without having to worry too much about details of the radial fluctuations within the inviscid core.

IV: Causality Reduction

In the previous section we have seen that dimensional reduction of the problem can still yield some useful results, and quasi-1D calculations can help design and understand the facility operation and exper-

imental diagnostic techniques. Some flow features are lost in this reduction process, for example the shock structure that propagates down the nozzle. If one were to compute the transient flow inside the test section, one would require a prior computation of the transient nozzle flow. This is an example of causal interaction between two different regions of the facility. The computation of the transient nozzle flow can be done by assuming constant stagnation conditions, or starting from a uniform shock impingement on the end wall of the driven tube. For later times, the propagation of the reflected shock in the driven tube must be followed accurately: this entails the interaction of the shock with the bounday layer and with the contact discontinuity. If this numerical simulation is done with sufficient detail, we can gather information on the effect of boundary layer and CD shape on pressure wave generation and flow contamination. The shape of the contact discontinuity may however depend on its early history, i.e. on the main diaphragm rupture itself. This is another example of causal interaction, which forces to model the diaphragm rupture and subsequent evolution, in order to at least estimate the effect on CD shape. This is another difficult problem which will require a lot of effort: the calculation done so far is only a first attempt at solving the problem, which helped us identify the areas where further improvement is necessary.

Although the opening and petaling of the steel diaphragm is a fundamentally 3-dimensional process, it is not required at this stage to include this complication. The problem is therefore reduced to a 2D axi-symmetric problem, and the diaphragm opening is reduced to a case of time varying boundary condition. The driver and driven tubes are gridded as two separate regions: between them, the boundary condition is set as a reflecting wall for some of the grid cells, and a patching condition for the grid cells within the opening. The distribution of patched/reflecting boundary points changes with time; in this first attempt, the grids are assumed fixed in time, i.e. the opening proceeds in steps, one grid point after another. If the grid had sufficent resolution in the radial direction, this would be a good approximation to a continuous process. Some effects are ignored in this approximation. First, the physical boundary (steel) between the two regions is changing in time, due to the distortion of the diaphragm (the petaling); its dynamics should be modeled as well, and this will require a major effort in the future. We also assumed that the diaphragm is initially vertical, while in reality it is to some extent assuming a hemispherical shape, due to the pressure rise in the driver tube. Since we are only interested at this point in testing the numerical capabilities, this is not a concern.

In Figure 16 we show the temperature contours of the flow transient, taken at three different times after the start of the opening of the main diaphragm. At 30 μseconds, the primary shock is just past the contracting section of the driven tube, immediately followed by the contact discontinuity and a hot layer of driver gas. The opening at that time is still small (about $1/6^{th}$ of the driven tube diameter). Notice that between the hot, sheared gas layer and the opening is a weak shock (blue contours in the figure) is emanating from the diaphragm opening. This is the result of the step in diaphragm opening: as one more cell of the driver section is put in contact with the driven tube, the sudden change in local boundary condition creates this weak shock. This purely numerical effect was difficult to estimate *a priori*, and is an interesting observation in itself: it forces us to reconsider the technique for future computations, in order to have a smoother, continuous opening. At a later time (54 μseconds), the primary shock has travelled further down the driven tube and significantly straightened. Oblique shocks reflected from the walls of the constricting section interact near the axis to form a strong mach disk. The shear layer has attached itself to the walls, and the driver gas behind the primary shock has developed a concave shape near the axis. At 70 μseconds, the primary shock is completely planar, the mach disk has shrunk, and a very complex flow structure follows the primary shock and CD. Since the stepwise diaphragm opening has produced spurious shocks, it is difficult to identify the real physical effects. Presumably, this structure is actually simpler (at least in this 2D approximation). We can safely assume that a few main conclusions can be drawn from this preliminary result:

- the primary shock becomes planar very rapidly ($\simeq 60\mu$seconds).
- a complex and unsteady flow structure, dominated by a mach disk, is formed behind the CD
- the CD itself develops a complex shape.

The last item can be more clearly demonstrated in Figure 17, which shows the CD and the main shock, for the same time sequence. It is clear from Figure 17-c that the CD is definitely non-planar; indeed, it is likely that from that moment on, the CD evolution will be dominated by Rayleigh-Taylor instabilities,

and will not recover an ideal, planar shape.

The remainder of the simulation, i.e. the full propagation of this structure down the whole length of the driven tube, would take a considerable amount of CPU, and has not yet been attempted. Future work will focus again on the diaphragm opening and on a numerical technique that more accurately describe it. It is important also to point out that this calculation is difficult for an additional reason: as the diaphragm opens, there is a strong jet of gas that flows through a small opening in a ideally reflecting surface. This jet has a tendency to entrain some flow around the opening, producing an artificial 'cavitation' near the surface. The same numerical phenomenon can be also observed occasionally near the base wall of a wedge in a hypersonic flow, for example. This numerical instability can be removed by enhancing the numerical diffusion in that region. This was done so in our case. This will also affect the diffusion of the driver gas into the driven tube, and therefore the extent of mixing and shape of the contact discontinuity. This transient flow must therefore be recomputed with special care.

Another example of causality relation concerns the influence of the combustion process in the driver and the flow in the driven tube. Pressure fluctuations are experimentally observed in the driver tube, which seems to indicate that the combustion is not a uniform process, and that some pressure waves are bouncing back and forth in the driver tube. These waves can travel down the driven tube after opening, and influence the pressure field in the stagnation region. This effect is demonstrated in Figure 18, where the pressure histories at two locations are compared with the computations: Figure 18-a shows the pressure history a few centimeters upstream of the main diaphragm, in the driver tube. Figure 18-b shows similar profiles near the end wall of the driven tube. Pressure fluctuations with a *sine* shape have been superimposed in the driver tube at the moment of diaphragm rupture; the amplitude of this fluctuation was chosen to match the experimental observation in the driver tube. These quasi-1D computations show a very good agreement with the experimental traces when the fluctuations (of the right phase) are superimposed. The agreement is notably much better than without these fluctuations (Figure 18-b). It is clear that the combustion process in the driver tube has a strong influence on the flow conditions in the stagnation region, and should also be modeled and better understood. These calculations were performed by G. Wilson at NASA-Ames, using a quasi-1D code: additional details on the modeling will be presented in the future [7].

These results are another example of the usefulness of dimensional reduction: it also shows that with some clever modeling, one can causally reduce the problem and retain an accurate description of the system. This should also help in understanding the conditions for better reproduction of test runs, and for more uniform flow conditions. This is another difficult task, which involves the modeling of energy deposition, initiation of deflagration and flame propagation. An effort in that direction is planned.

V: Conclusions and Future Plans

From these preliminary results, we can draw the following conclusions:

- The flow conditions are very severe and put enormous strain on the accuracy and stability of the current numerical techniques. Further research into the improvement of the numerical techniques is desirable.
- The validation of the CFD capabilities will require some difficult measurements, including high resolution video recording of the transient processes, such as secondary and main diaphragm rupture.
- The numerical modeling of the facility, even with simplistic assumptions (quasi-1D), can greatly benefit the design of experiments, diagnostic procedures, new test conditions, and understanding of the tunnel performance.
- The computation of separate regions of the facility treated as independent is an approximation at best. The influence of remote and past events on the overall flow structures is not negligible, and must be estimated. The separation of the facility flow into separate regions can be used for the estimation of various physical phenomena.

The most immediate challenge still concerns the opening of the main diaphragm. The preliminary results shown here suffer from an inadequate treatment of the unsteady boundary condition, and must be recomputed more accurately. Other challenges that await us concern the importance of various physical effects, such as shock-BL interactions at the end of the driven tube, and wall chemistry and ablation and resulting flow contamination. These three topics will be addressed in the future.

VI. References

[1] A. G. Gaydon & I.R. Hurle, "The Shock-Tube in High-Temperature Chemcal Physics", Reinhold Publ., 1963.

[2] J. Cavolowsky *et al*, 'Flow Characterization in the NASA Ames 16-inch Shock Tunnel', 28^{th} Joint Propulsion Conference, Nashville, TN 1992. AIAA paper 92-3810.

[3] J. Bell et al., 'Adaptive Mesh Refinement on Moving Quadrilateral Grids', AIAA 9^{th} Computational Fluid Dynamics Conference, Buffalo, N.Y. 1989. AIAA paper 89-1979.

[4] P.A. Jacobs, "Simulation of Transient Flow in A Shock Tunnel and a High Mach Number Nozzle", 4^{th} Int. Symp. Comp. Fluid Dynamics, Davis, September 1991.

[5] M. Lewis, U. Maryland, private communication.

[6] M. Van Dyke, "An Album of Fluid Motion", p.171, Parabolic Press, 1982.

[7] G. Wilson, 'Time-Dependent Quasi-1D Simulations of High Enthalpy Pulse Facilities", to be presented at the AIAA 4^{th} Int. Aerospace Planes Conference, Orlando, Dec. 1992.

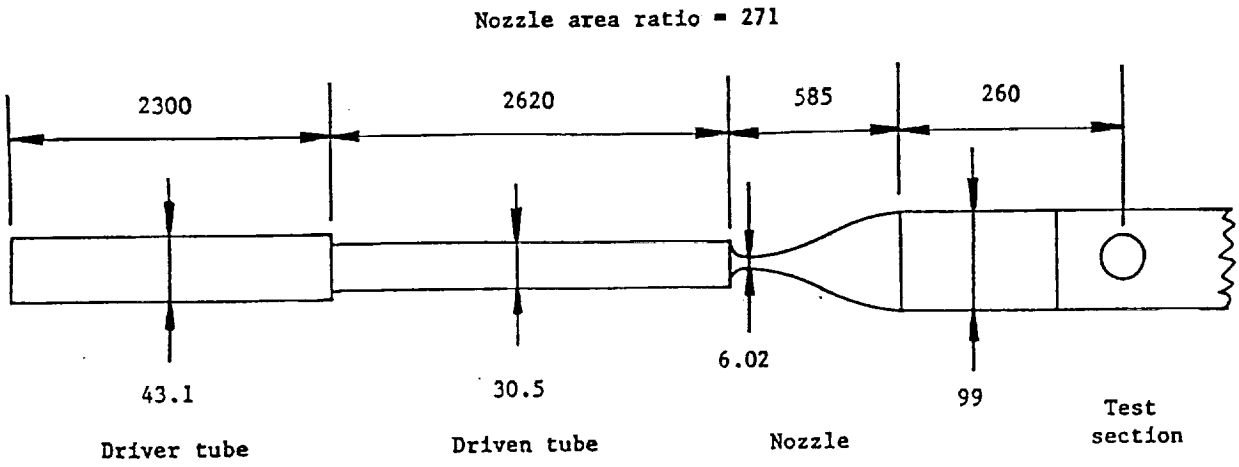

Figure 1: Schematic (not to scale) of Ames 16" Shock Tunnel facility. All dimensions are in cm.

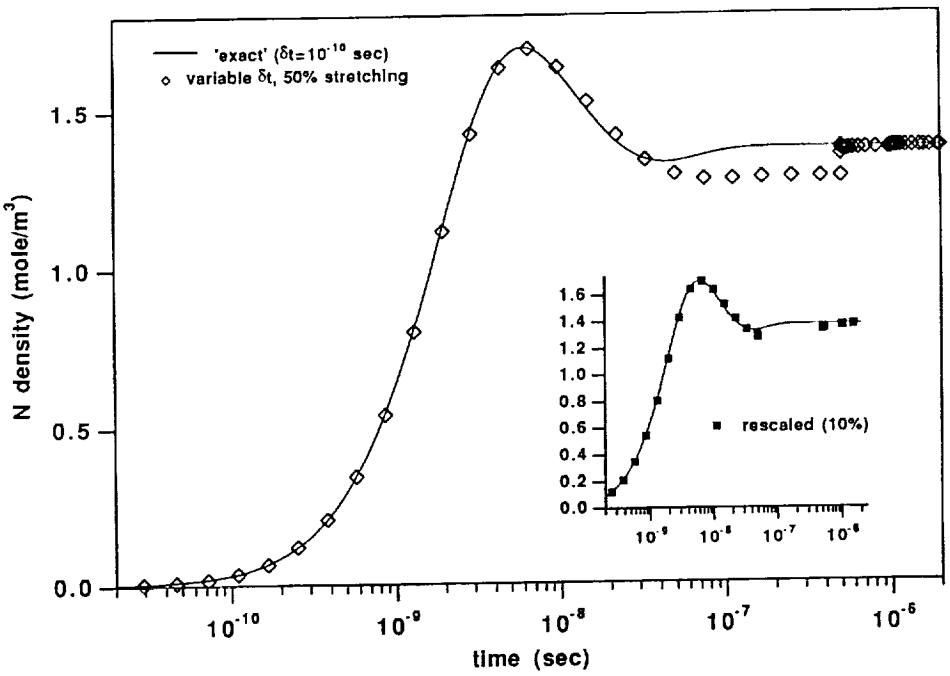

Figure 2: Computation of stiff chemistry. The open symbols are obtained when the implicit chemistry solver is sub-iterated with an increasingly large sub-step. The temperature change is also estimated at each sub-step. The integration proceeds until $\Delta t = 5\ 10^{-7}$ seconds, which is an assumed global time step. Deviations from the 'exact' solution at times greater than 10^{-7} seconds are due to an error in the estimate of temperature. As the first integration is terminated, a more accurate estimate of the temperature (including variations of the specific heat) is made, and the solution quickly converges to the correct one. The insert shows the effect of rescaling of the chemical time scale: here the integration proceeds only to 10% of the global time step. The integration during the second global step also quickly converges to the exact solution.

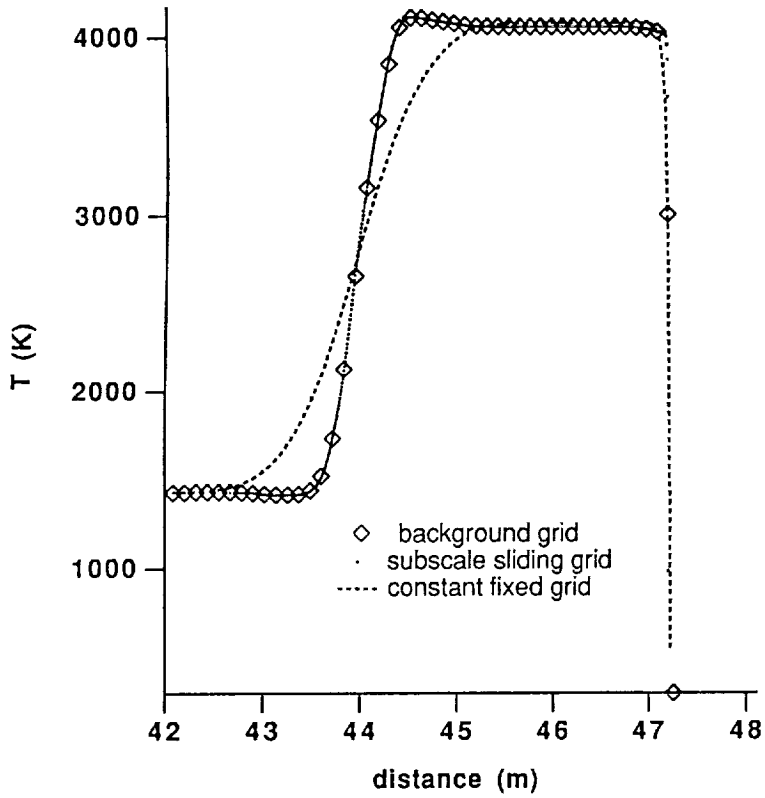

Figure 3: Grid subscaling performance. A constant fixed grid (1000 points) is compared with the results from a high density grid (800 points) moving along with the shock. This final profile, at the end of teh driven tube, shows the increase in resolution of the contact discontinuity. The high density ('subscaled') grid is a subset of the 'background' grid (250 points), and moves by steps equivalent to one cell spacing of the background grid. The transfer of information between the two grids proceeds by volume averaging, and is fully conservative.

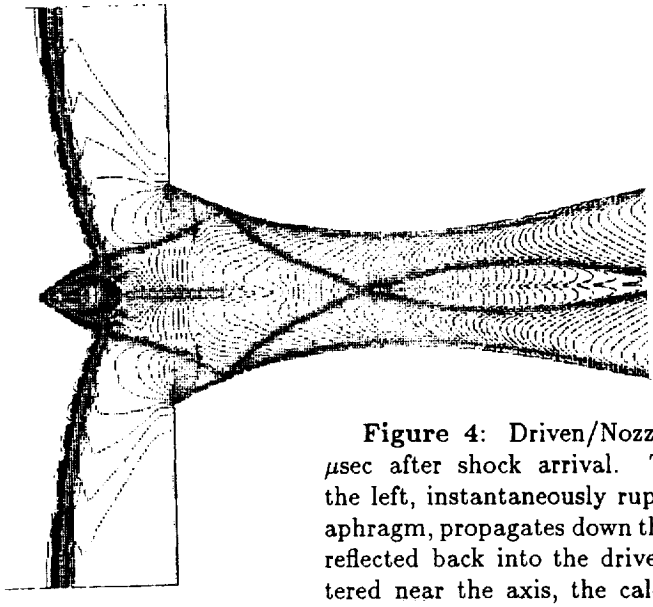

Figure 4: Driven/Nozzle flow transient at 80 μsec after shock arrival. The shock comes from the left, instantaneously ruptures the secondary diaphragm, propagates down the nozzle and is partially reflected back into the driven tube. Cells are clustered near the axis, the calculation id for inviscid, non-reacting flow, spatially 2^{nd}-order. The conical structure is believed to be an artifact from the numerical method.

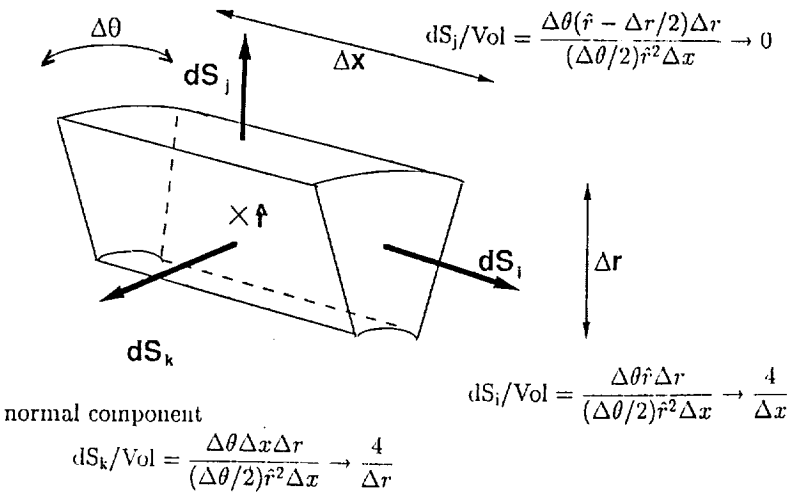

$$dS_j/\mathrm{Vol} = \frac{\Delta\theta(\hat{r} - \Delta r/2)\Delta r}{(\Delta\theta/2)\hat{r}^2\Delta x} \to 0$$

$$dS_i/\mathrm{Vol} = \frac{\Delta\theta\hat{r}\Delta r}{(\Delta\theta/2)\hat{r}^2\Delta x} \to \frac{4}{\Delta x}$$

$$dS_k/\mathrm{Vol} = \frac{\Delta\theta\Delta x\Delta r}{(\Delta\theta/2)\hat{r}^2\Delta x} \to \frac{4}{\Delta r}$$

Figure 5: Schematic of finite-volume computational cell in cylindrical geometry. Surface to volume ratios are independent of the wedge angle. The momentum source term in the axi-symmetric formulation of the Euler equations is proportional to dS_k, and behaves as $1/\Delta r$ near the axis.

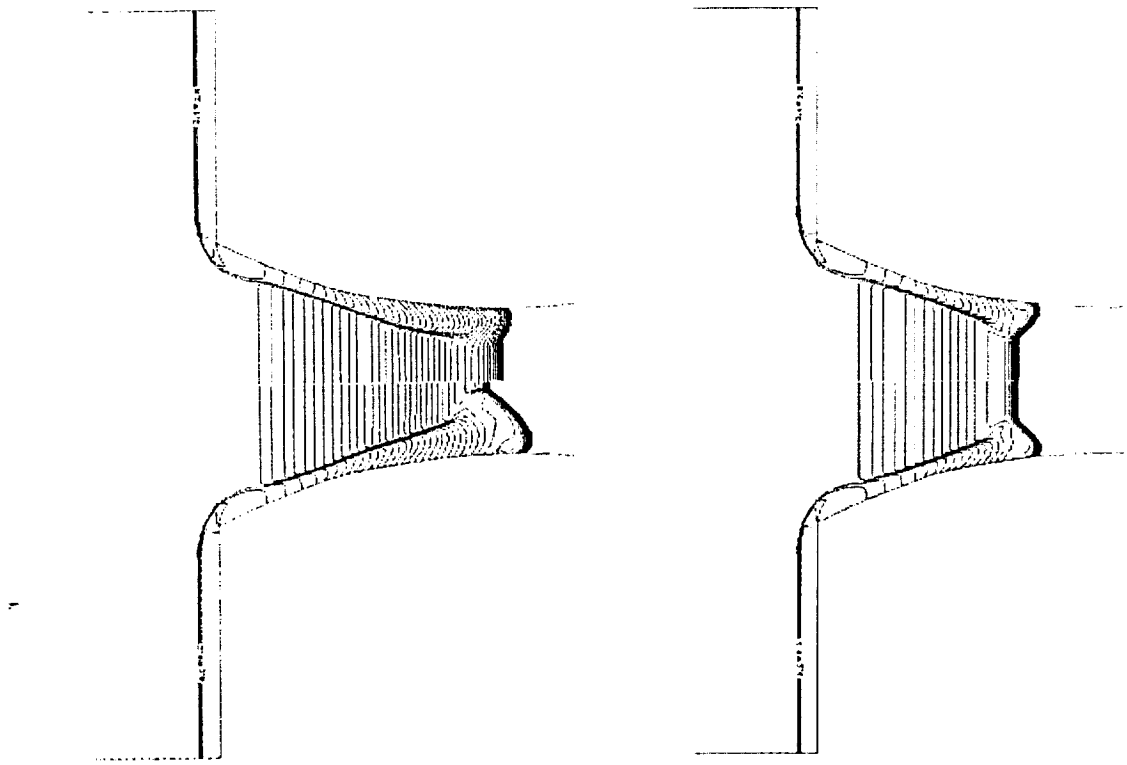

Figure 7: Effect of viscosity for low nozzle pressures. The top section shows the results for a cutoff of gradients at a scale comparable to 0.1 mfp. The bottom section uses a cutoff at 10 mfp. The case on the left is for a nozzle pressure of 100 μTorr, the case on the right is for 100 milliTorr (the experimental condition for the 16" shock tunnel). The cutoff allows greater stability and greater time steps in computing implicitely the viscous terms. The contours shown on the right hand side show that for our case of interest, the results are insensitive to the choice of cutoff.

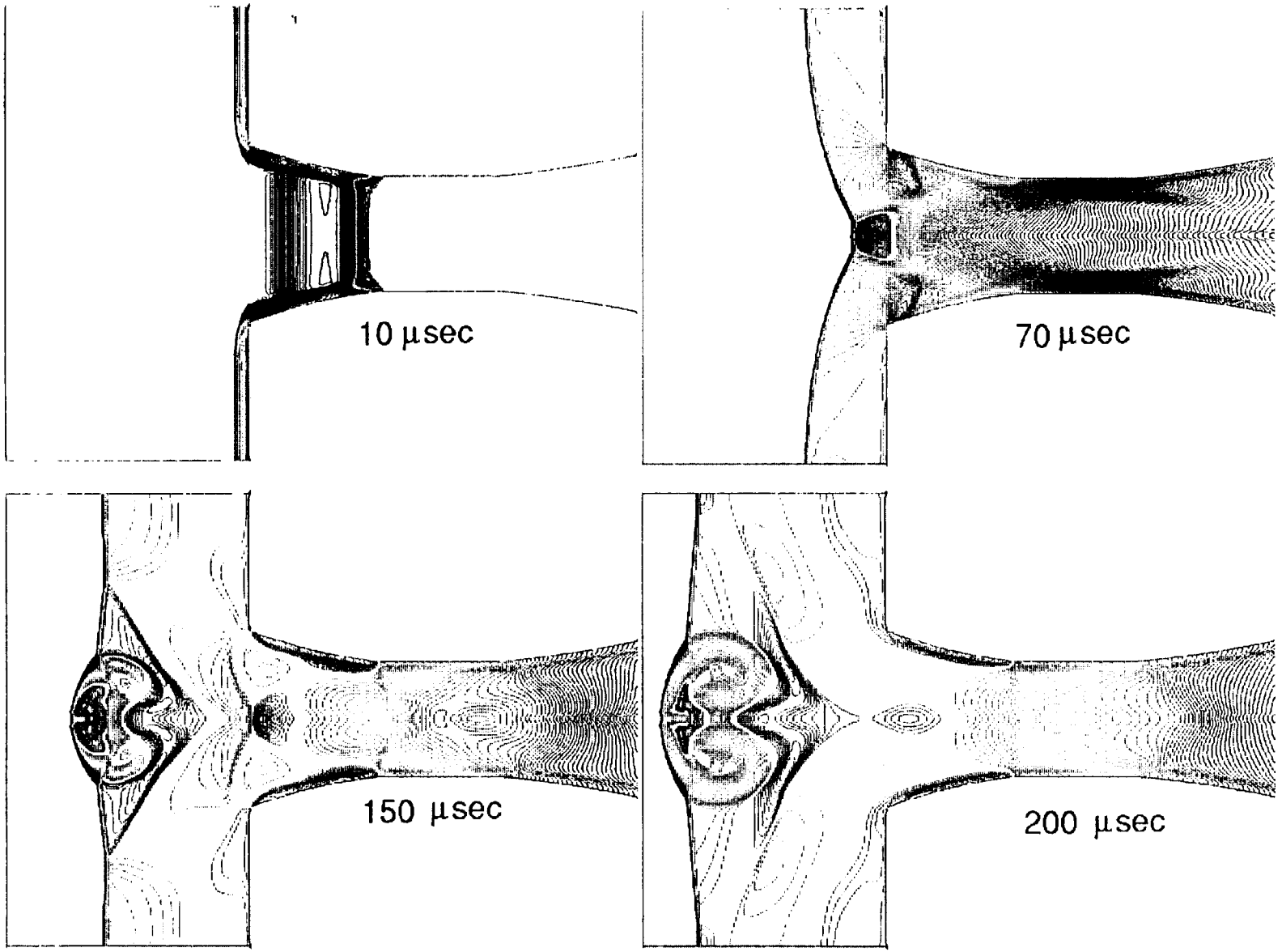

Figure 6: Driven/Nozzle flow transient. This computation is obtained after coarsening the grid in the radial direction near the axis. The shock convergence on the axis (70 μsec) now leads to a stable shock structure ('bubble') near the axis. The formation of an intense vortex is evident for 200 μsec. Plots at later times would show that the reflected shock becomes essentially planar at $\simeq 500\mu$sec, while the vortex structure persists.

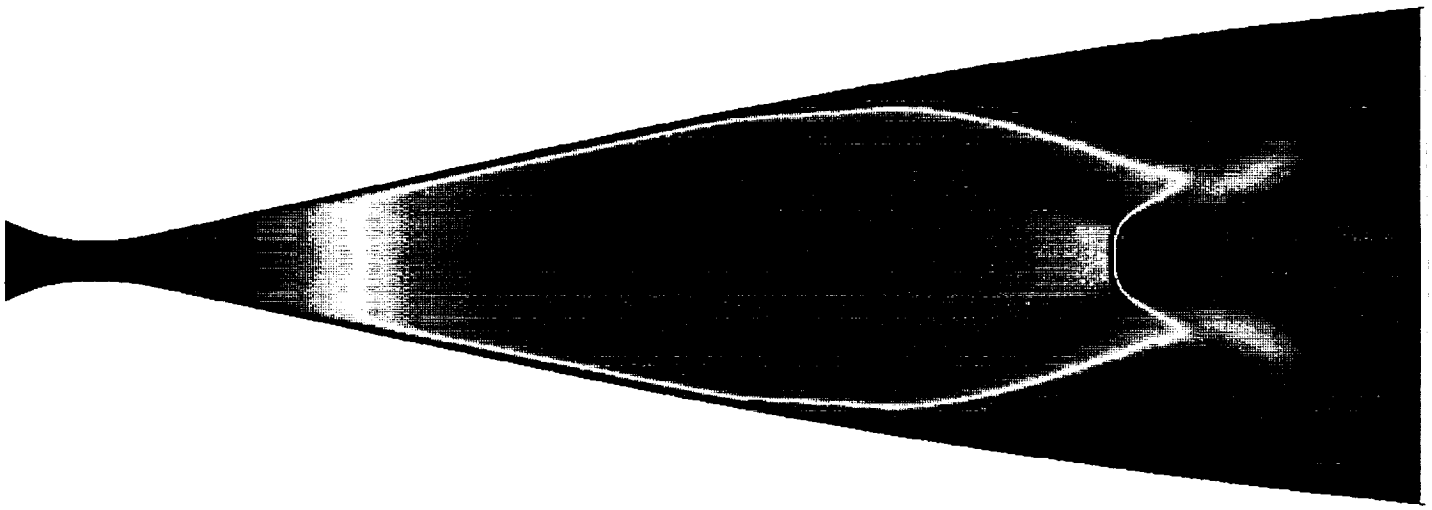

Figure 8: Nozzle flow transient (Mach contours). The curved primary shock can be identified on the right. Weak oblique shocks are emanating from the walls and converge to form a strong (upstream facing) mach disk on the axis, and reflect back. Strongly sheared flow is visible between the primary shock and the first oblique shocks. A contact discontinuity behind the primary shock has been numerically diffused beyond idenitification. A small vertical break in contours is due to an interpolation error by the graphics, between two different grids.

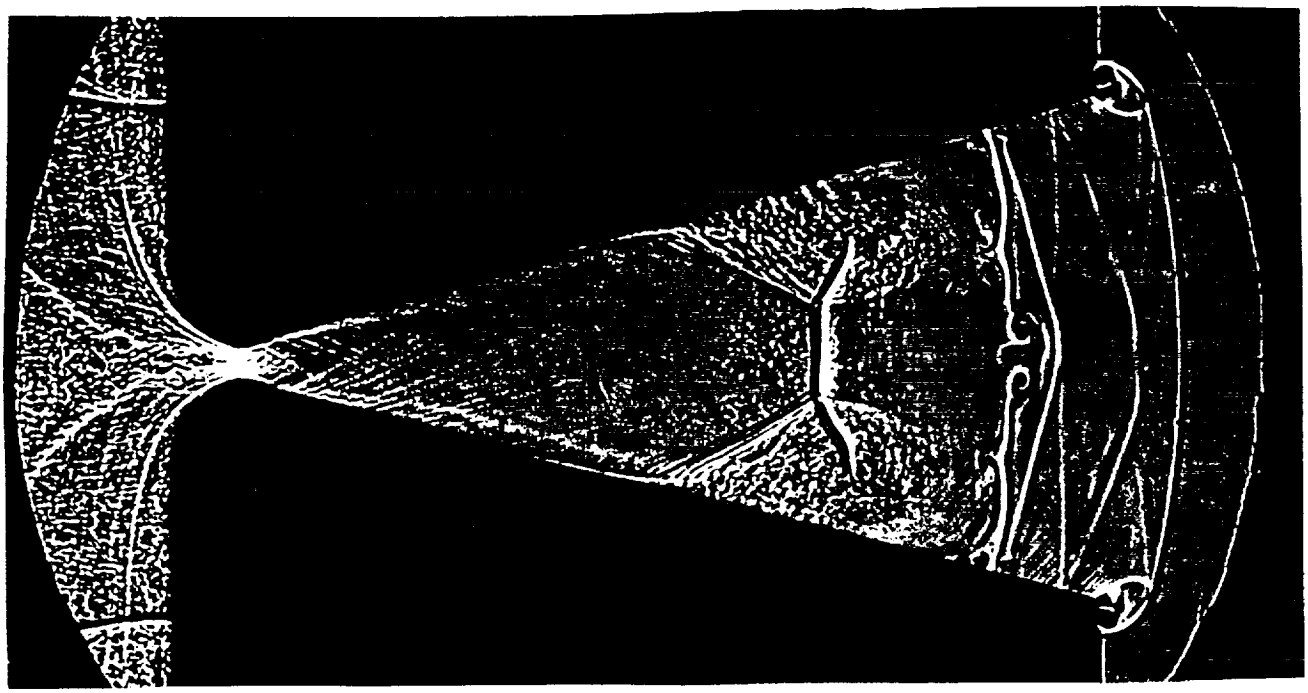

Figure 9:Experimental shadowgraph, taken from [6]. The upstream facing shock and the attached oblique shocks are clearly defined in this picture. Contact discontinuities are also very clear, and show strong vortices. All features of Figure 8 are contained in this picture.

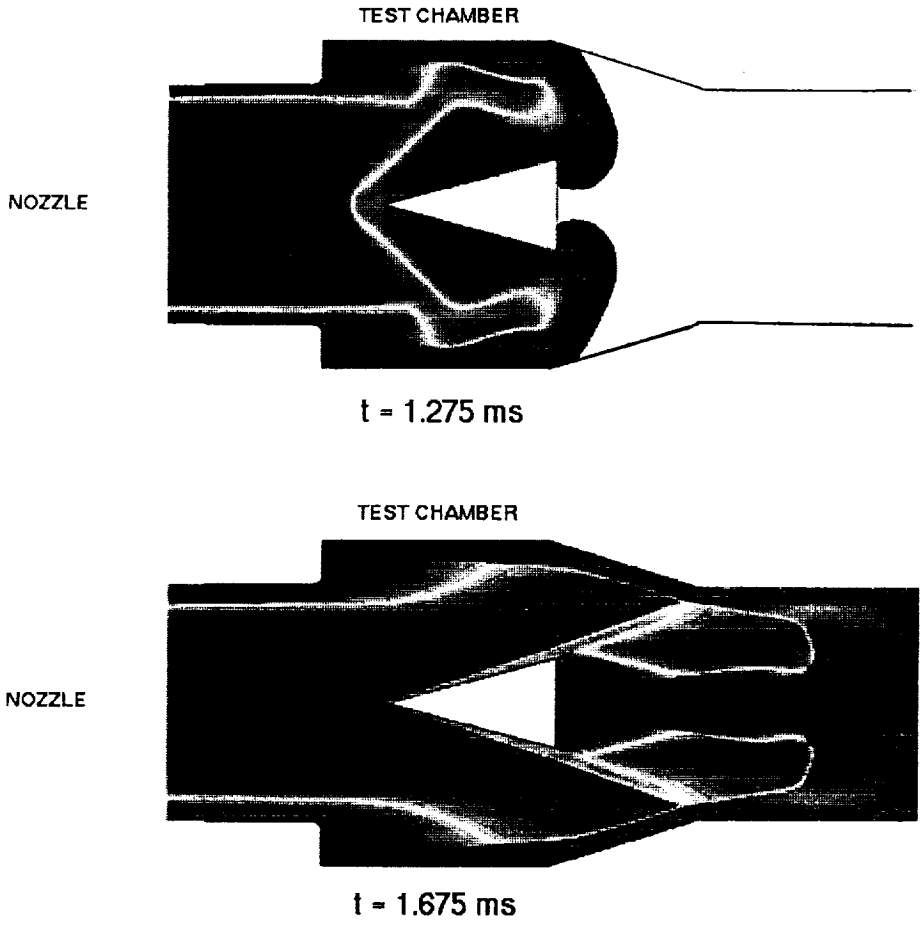

Figure 10: Interaction in test chamber (Mach contours). In this example, as the primary shock diffracts at the end of the cone, the remainder of the shock structure has just reached the apex of the cone. For this case, steady flow over the testing body is achieved within 400 μseconds.

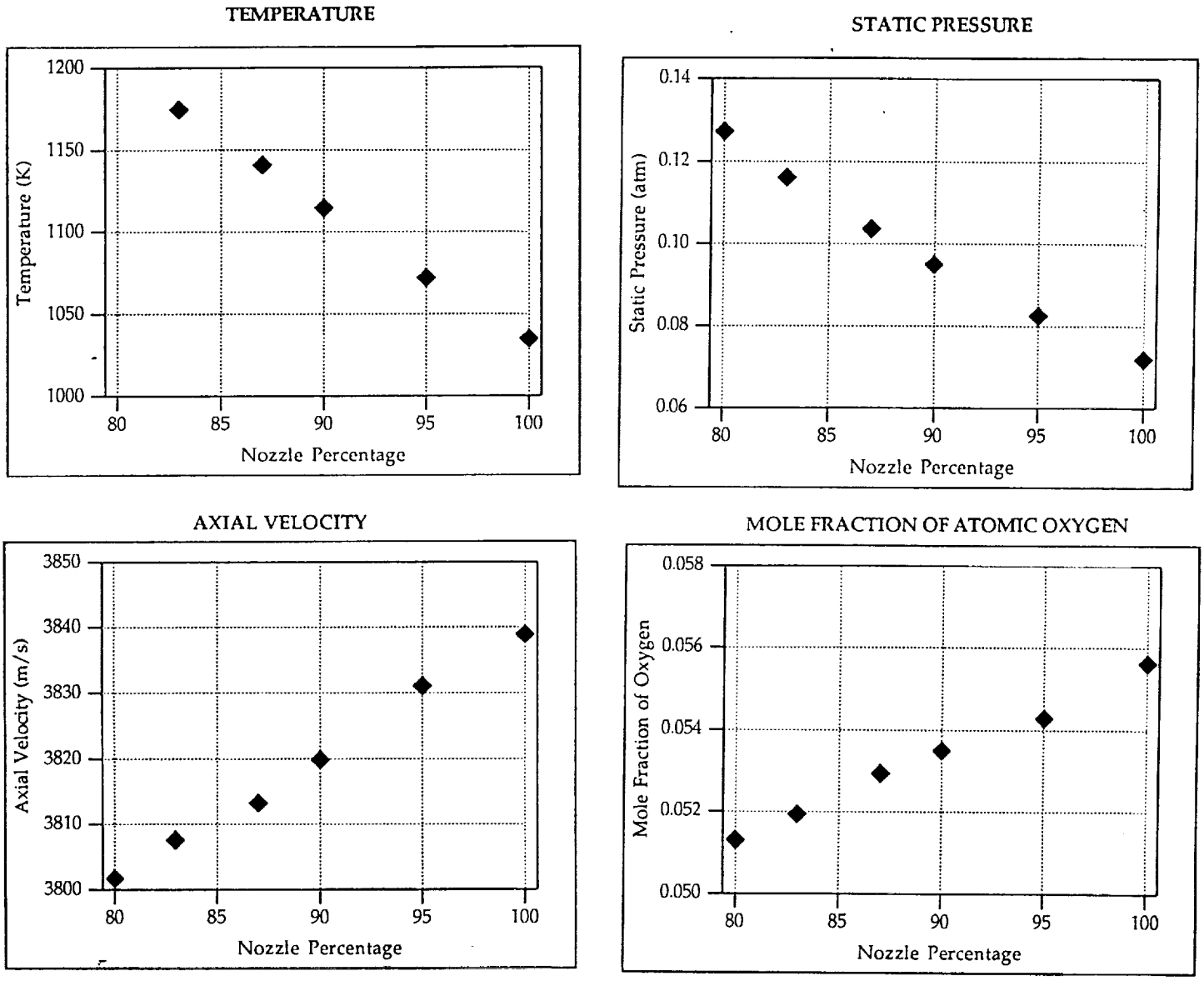

Figure 11: Sensitivity of various flow quantities to effective nozzle area. The nozzle shape is replaced by a modified nozzle contour from the throat on, by removing a fixed fraction of the radius (i.e. the 87% nozzle removes 13% of the radius), to account for the boundary layer. Examination of the plots shows that the static pressure is the most sensitive variable, and therefore the most useful variable to determine experimentally.

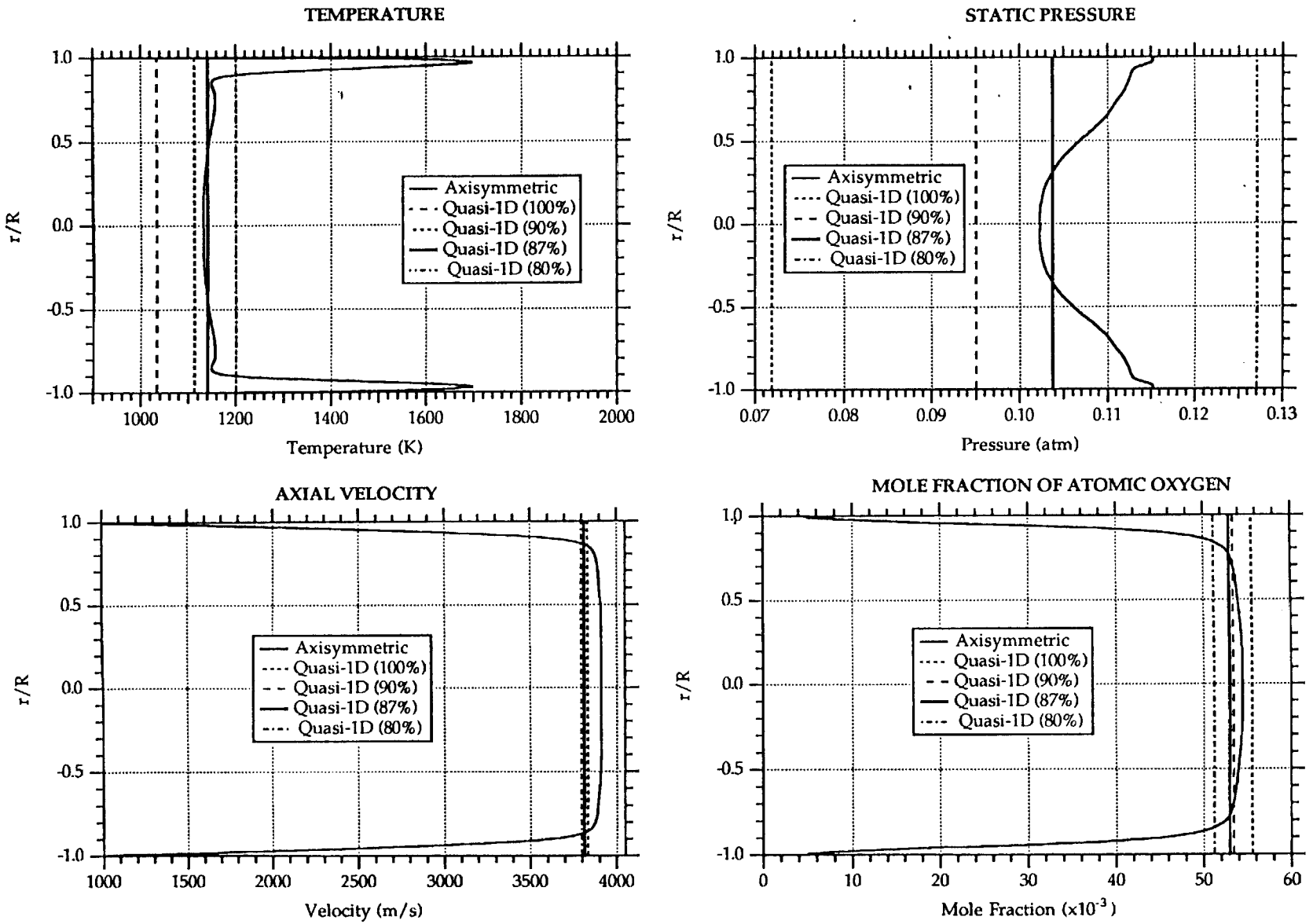

Figure 12:Comparison of quasi-1D solutions with 2D axi-symmetric solution. Except for the flow within the boundary layer, the agreement is very good for the 87% case. Most variables have a flat profile in the core region, except the static pressure. Again, measurement of the static pressure should yield some valuable information on the nozzle flow, and for code validation.

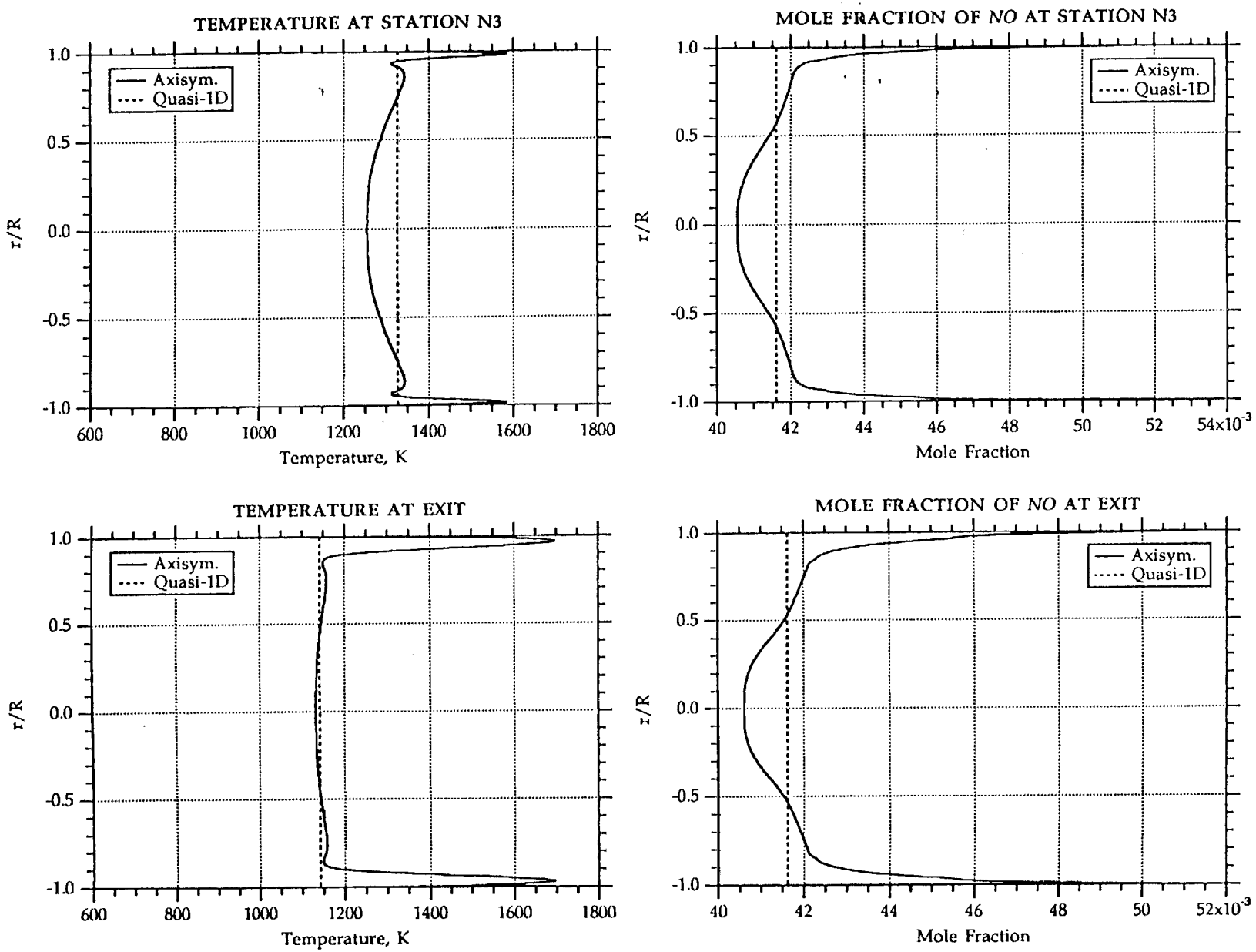

Figure 13: Temperature and *NO* mole fraction at two stations. There is still some significant core variation of the temperature at N3. The *NO* concentration profile remains essentially frozen, with most of the gradients in the boundary layer, as expected.

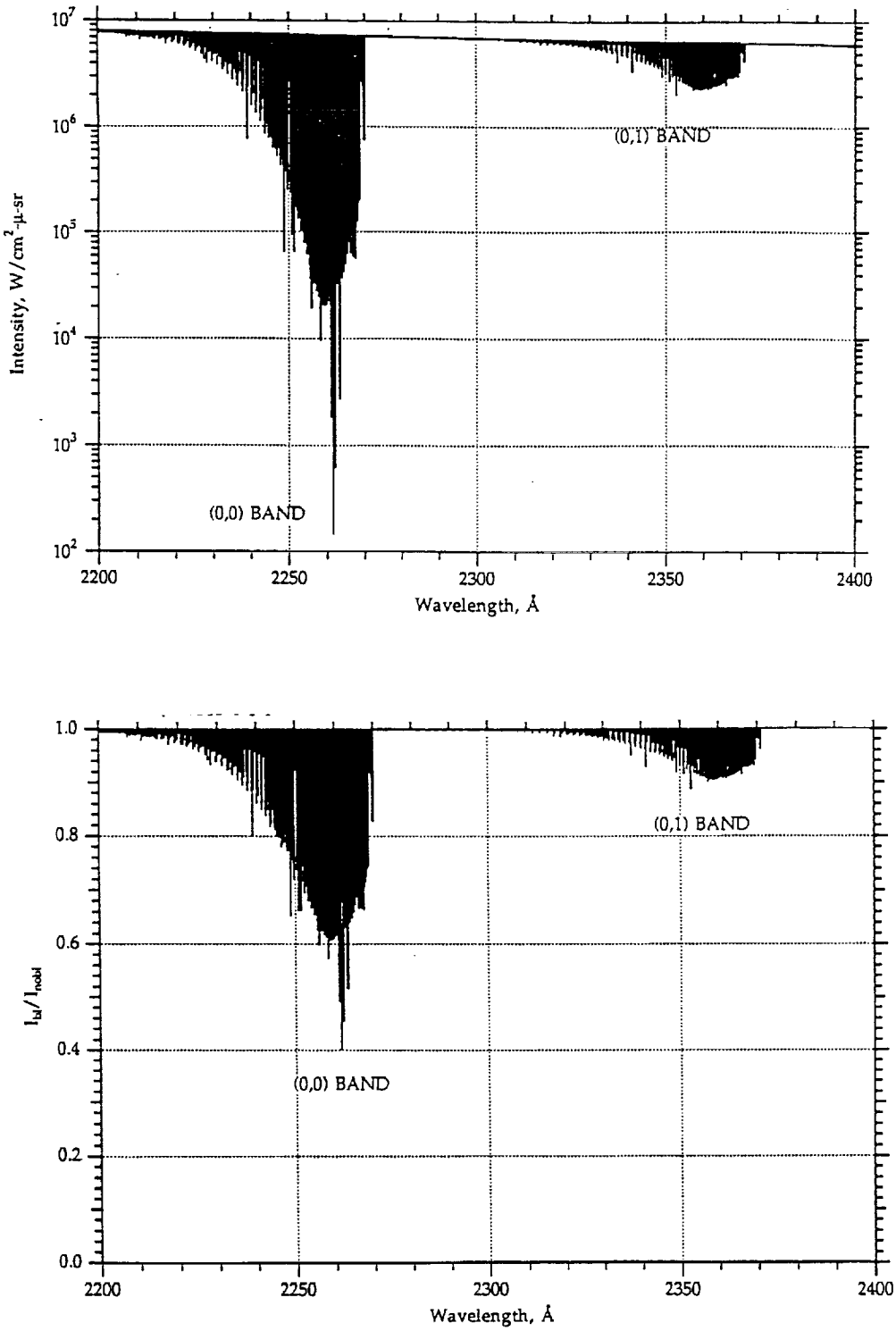

Figure 14: Computed Intensity at station N3, with and without the boundary layer. Figure 14-a (top), shows the intensity in absolute value, with the boundary layer included. Figure 14-b (bottom), shows the ratio of computed intensity *with* the boundary layer, versus the computed intensity *without* boundary layer. A similar plot for the exit plane would show a ratio at peak absorption of 0.2.

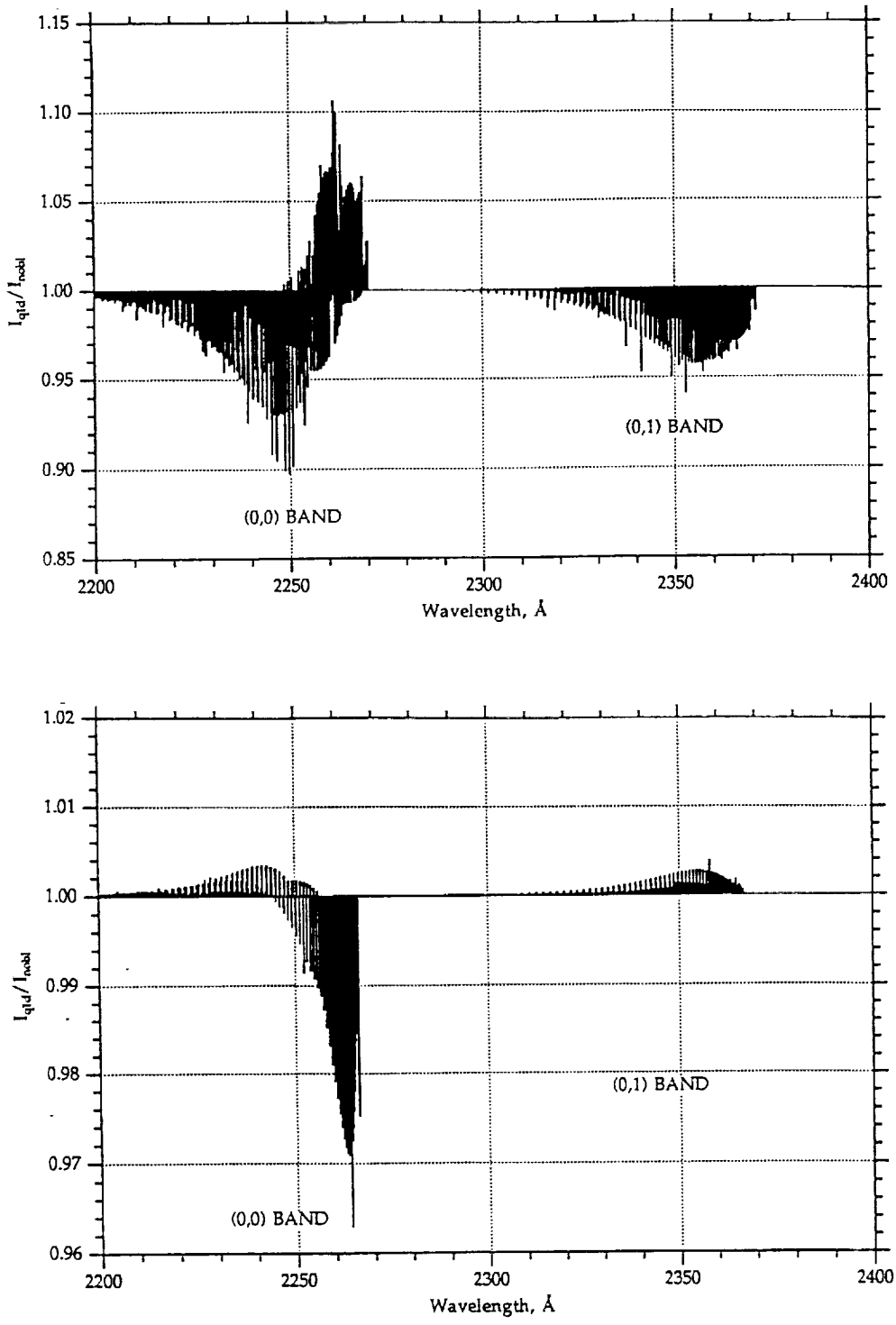

Figure 15: Comparison of quasi-1D and axi-symmetric cases (without BL). Figure 15-a (top) shows the ratio of the computed intensity for the quasi-1D solution (87%) versus the computed intensity for the 2D solution at station N3. Figure 15-b (bottom) shows a similar quantity for the exit plane.

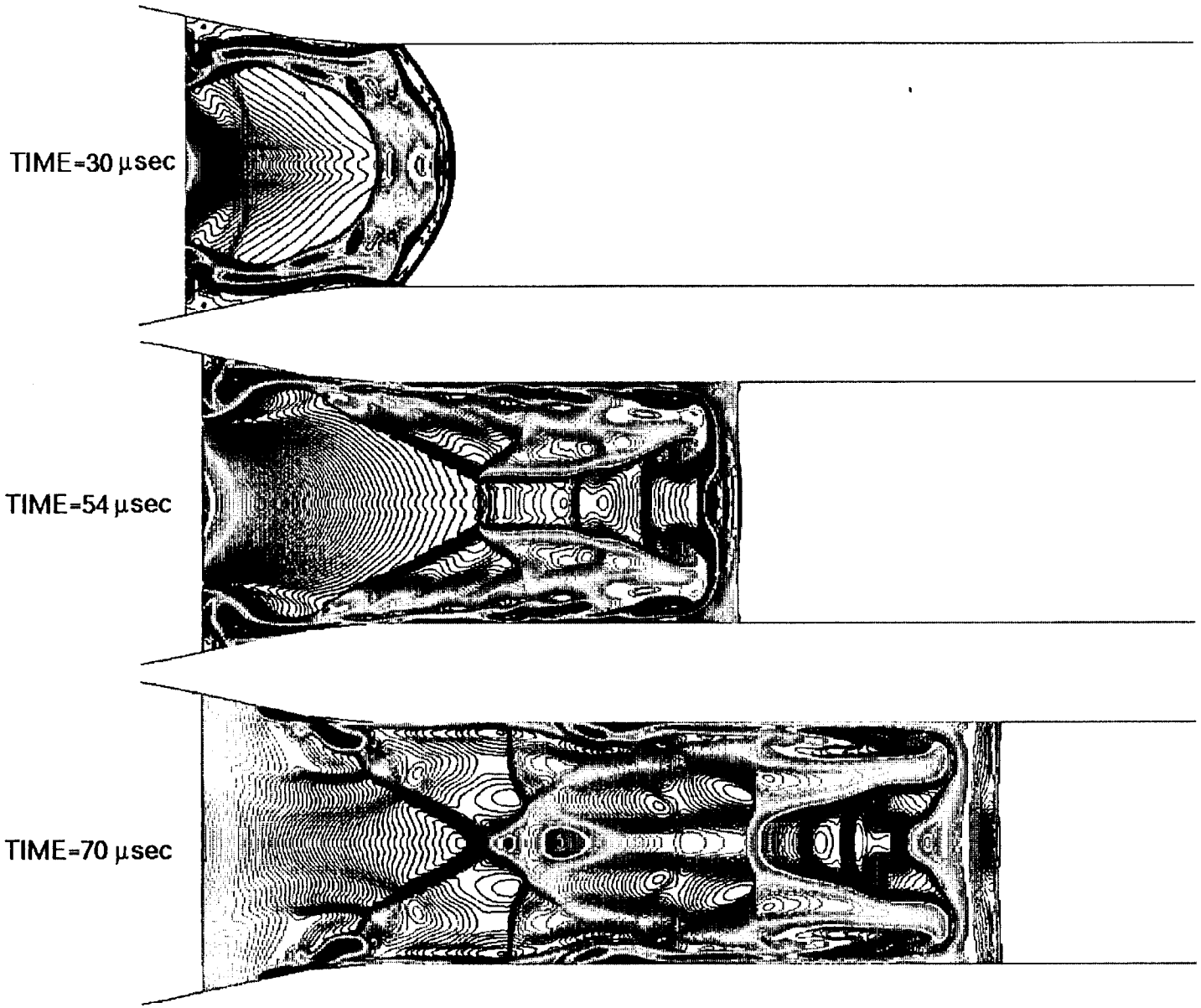

Figure 16: Flow transient at main diaphragm. Figure 16-a (top) taken at 30 μsec, Figure 16-b (middle) at 54 μsec, Figure 16-c (bottom) at 70 μ sec after start of diaphragm opening. The opening sequence has been set arbitrarily.

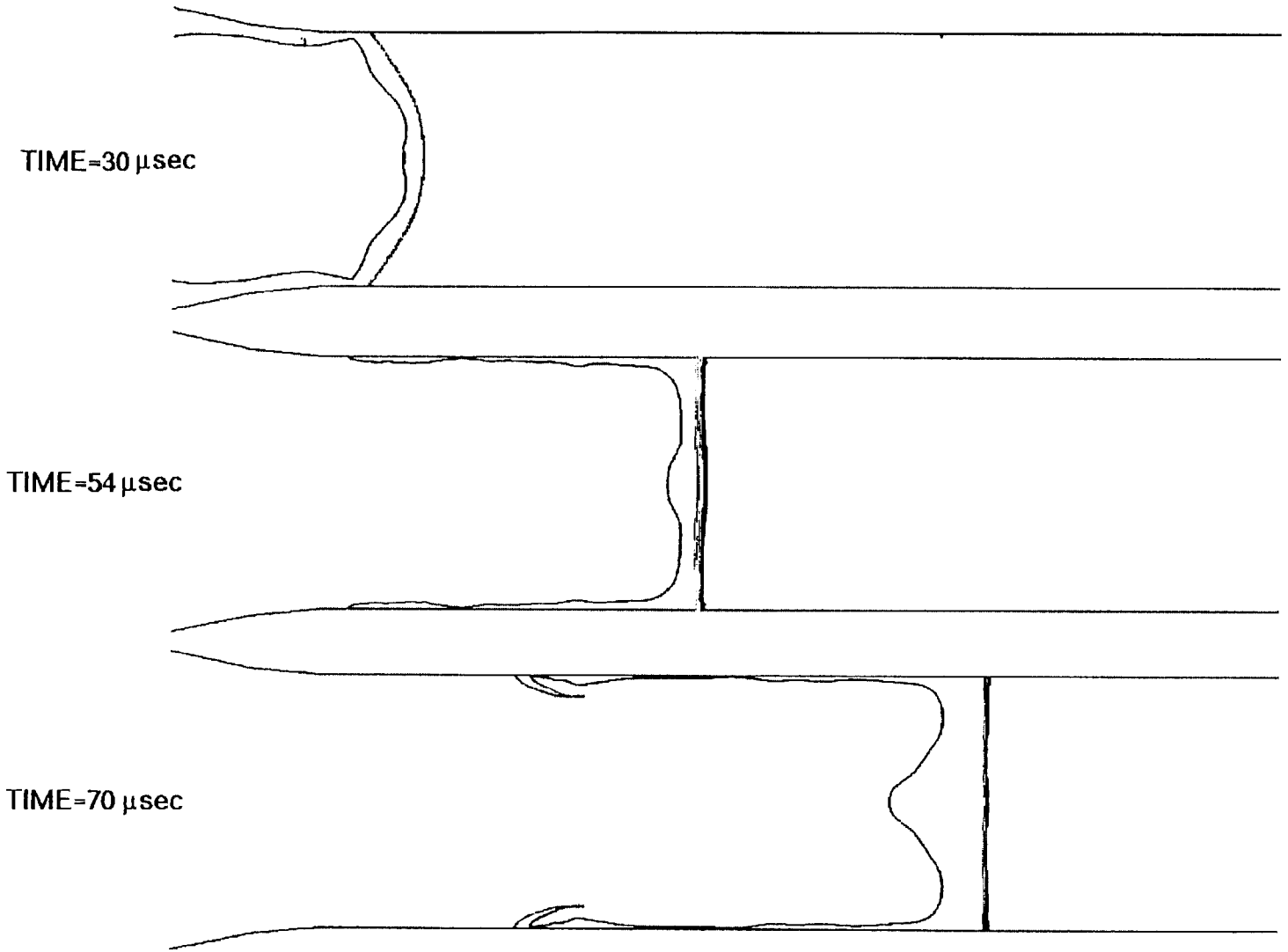

Figure 17: Shock and Contact Discontinuity for same time sequence as Figure 16.

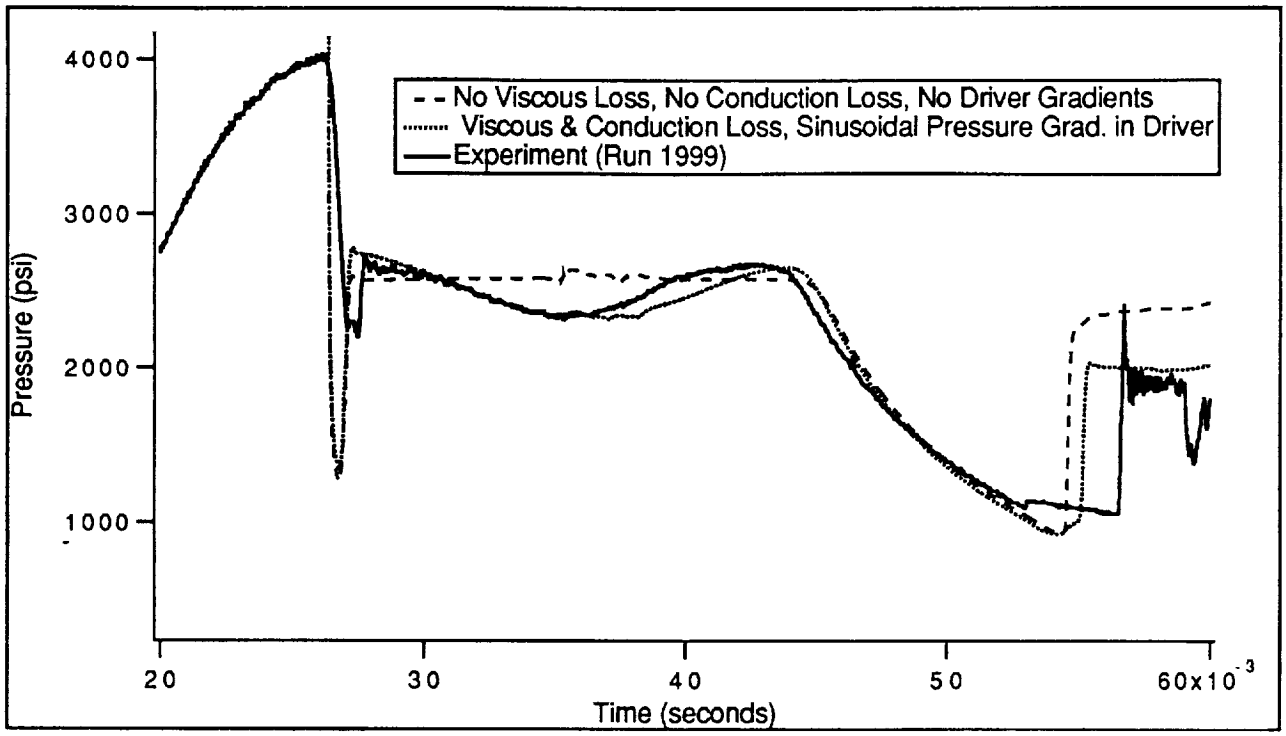

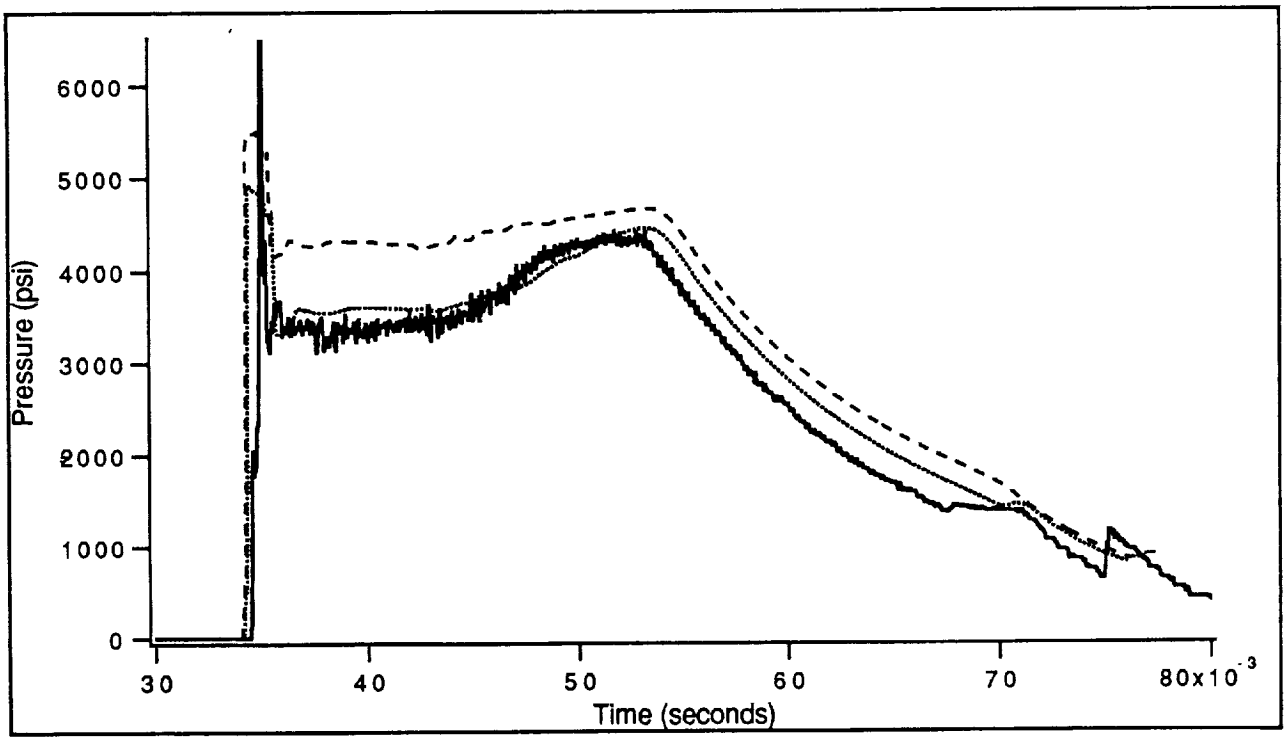

Figure 18: Comparison between experimental and computed pressure traces at two locations. Figure 18-a (top) shows the comparison at a few cm upstream of the main diaphragm in the driver tube. Figure 18-b (bottom) shows the traces for a point near the end of the driven tube. Significantly better agreement is obtained after assuming an *ad-hoc* pressure gradient within the driver tube, at the end of combustion.